DISS. ETH NO. 22365

Interplay of Diffusivity and Reactivity in Organic Aerosol Aging

A thesis submitted to attain the degree of
DOCTOR OF SCIENCES of ETH ZURICH
(Dr. sc. ETH Zurich)

presented by
SARAH S. STEIMER
M.Sc., Uppsala Universitet

born on 14.09.1983
citizen of Germany

accepted on the recommendation of
Prof. Dr. Thomas Peter, examiner
Prof. Dr. Markus Ammann, co-examiner
Prof. Dr. Daniel Knopf, co-examiner
Dr. Ulrich Krieger, co-examiner

2014

Contents

ABSTRACT

Atmospheric aerosol particles influence climate, affect human health, and transport condensed materials over long distances. During their lifetime in the atmosphere, those particles undergo transformation through chemical reactions. This aging process in turn affects their properties, such as hygroscopicity and absorptivity. It has been shown that particles which contain organic matter can adopt an amorphous solid state in the atmosphere. This will slow down the mass transport within the condensed phase, which could decrease reactivity by limiting reactant supply. This thesis deals with the question of how exactly changes in physical state and thereby diffusivity influence chemical reactions in atmospheric particles.

To investigate the influence of physical state on reactivity of organic matter in particles, we studied the kinetics of the shikimic acid ozonolysis in depth, using three different experimental techniques: electrodynamic balance (EDB) measurements, scanning transmission X-ray microscopy (STXM) combined with near-edge X-ray absorption fine structure (NEXAFS) spectroscopy, and measurements with a coated wall flow tube operated under atmospheric pressure. EDB measurements of single, levitated shikimic acid particles were used to investigate the physical state of shikimic acid and obtain parametrizations for density, concentration and water diffusion coefficients as a function of relative humidity. We found that shikimic acid particles do not crystallize at low humidity, but become amorphous solids instead and that water diffusivity decreases from 1.9×10^{-9} $m^2 s^{-1}$ in the dilute aqueous solution to about 1×10^{-16} $m^2 s^{-1}$ in a dry shikimic acid particle.

With this knowledge, we then investigated the influence of physical state on the shikimic acid ozonolysis.

We used STXM-NEXAFS to follow the shikimic acid degradation. This was the first time that these techniques were successfully applied to measure the reaction of an atmospherically relevant material in situ. Decreasing humidity clearly correlated with decreasing reactivity. We saw a dependence of the reaction rate on particle size at low humidity, but did not observe a gradient in shikimic acid within the particle at any measured humidity. From this we concluded that the system can best be described by the analytical expression for reacto-diffusion limited uptake at all humidities below the highest humidity considered (83 %). The second order rate constant of the ozonolysis was determined for the first time; its value is $(3 \pm 1.8) \times 10^3\ \mathrm{L\,mol^{-1}\,s^{-1}}$.
To extend the range of accessible kinetic regimes, we also studied the same reaction by monitoring the ozone consumption in a flow tube under varying environmental conditions. Both the general trend in correlation of humidity and reactivity, and the obtained second order rate constant of $(1.5 \pm {}^{1.5}_{0.5}) \times 10^3\ \mathrm{L\,mol^{-1}\,s^{-1}}$ are in good agreement with the results from the X-ray microscopy experiments. Using the resistor model, we found that like in the microspectroscopy study, the uptake at all humidities apart from the highest (here 92 %) is best described as reacto-diffusion limited. However, the resistor model approach showed clear deficiencies in describing the uptake on long timescales and at low humidities. Fitting the experimental data with a kinetic flux model indicated that limitation in mass transport of shikimic acid might be responsible for some of these discrepancies. While the general trend of reactivity with relative humidity was captured well, none of the fits managed to correctly reproduce all features of the measured uptake. Further improvements of the implementation of processes in the model and of the fitting procedure itself are clearly needed.

With this work, we showed that a multi-technique approach is a clear benefit when dealing with complicated questions such as the dependence of reactivity on diffusivity in the condensed phase. In particular sophisticated models, such as the kinetic flux model we used to evaluate the flow tube data, benefit from the different constraints provided by the different experiments to reduce arbitrariness of the results.

ZUSAMMENFASSUNG

Atmosphärische Aerosole spielen eine wichtige Rolle für das Klima und unsere Gesundheit und sind daher ein aktuelles Forschungsgebiet. Auf Grund ihrer langen Lebensdauer in der Atmosphäre können sie über große Distanzen transportiert werden und damit außerdem auch zur Verbreitung von biologischen Stoffen wie z.B. Sporen und Pollen beitragen. Während der Lebenszeit eines Aerosols in der Atmosphäre können sich seine chemischen Bestandteile in Folge von Reaktionen ändern. Dieser Alterungsprozess kann dann auch die Eigenschaften der einzelnen Aerosolpartikel, wie zum Beispiel Hygroskopizität und Absoptivität, verändern. Für Aerosolteilchen, die viele organische Verbindungen enthalten, wurde meist die Annahme gemacht, dass sie flüssig sind. Es hat sich jedoch gezeigt, dass sie unter entsprechenden Umweltbedingungen auch einen festen, amorphen Zustand annehmen können. In diesem Fall ist die Diffusion im Inneren des Teilchens verlangsamt, wodurch es prinzipiell zu Konzentrationsgradienten kommen kann. Dies wiederum führt zu einer Reduktion der Reaktionsrate. Diese Arbeit beschäftigt sich nun mit der Frage, wie genau der Aggregatzustand von Aerosolteilchen die Reaktionskinetik der darin enthaltenen Verbindungen beeinflusst.

Um den Einfluss des Aggregatzustands auf die Reaktionskinetik von Teilchen mit organischen Bestandteilen zu verstehen, untersuchten wir ein Modellsystem mittels drei verschiedener experimenteller Methoden. Als Modellsystem wählten wir hierbei die Ozonolyse von Shikimisäure bei unterschiedlichen Feuchten. Um die Mikrophysik der Shikimisäure-Wasser Teilchen zu verstehen, nutzten wir eine

elektrodynamische Falle. Diese misst die Änderung der Partikelgröße und -masse durch Wasseraufnahme und -abgabe bei variierender Feuchte. So erhielten wir Informationen über den Einfluss der Feuchte auf den Aggregatzustand, die Konzentration, die Dichte der Lösung und die Diffusion von Wasser. Es zeigte sich, dass Shikimisäureteilchen nach Trocknung aus der Lösung einen amorphen, festen Zustand annehmen. Die Diffusionskonstante sinkt dabei von 1.9×10^{-9} $\mathrm{m^2\,s^{-1}}$ in der verdünnten wässrigen Lösung auf etwa 1×10^{-16} $\mathrm{m^2\,s^{-1}}$. Mit diesem Wissen konnten wir dann den Einfluss der verlangsamten Diffusion auf die Reaktionskinetik der Ozonolyse von Shikimisäure untersuchen.

Durch eine Kombination aus Röntgenmikroskopie und -spektroskopie waren wir desweiteren in der Lage, den Abbau der Shikimisäure in einzelnen Teilchen direkt mitzuverfolgen. Dies war das erste Mal, dass diese Technik erfolgreich zur Untersuchung einer laufenden Reaktion unter umweltrelevanten Bedingungen eingesetzt wurde. Wir beobachteten dabei, dass die Abbaurate bei niedriger Feuchte klar abnahm. Zusätzlich ergab sich eine Abhängigkeit der Reaktionsrate von der Größe des Teilchens. Ein Gradient in der Shikimisäurekonzentration wurde jedoch nicht beobachtet. Dies führte uns zu der Schlussfolgerung, dass sich der Abbau bei den meisten Feuchten am besten durch den analytischen Ausdruck für klassische reakto-diffusive Limitierung beschreiben lässt. Die in diesem Experiment zum ersten Mal bestimmte Ratenkonstante zweiter Ordnung ist $(3 \pm 1.8) \times 10^3$ $\mathrm{L\,mol^{-1}\,s^{-1}}$. Sie wurde bei der höchsten gemessenen Feuchte, 83 %, bestimmt, wo von reaktionslimitierter Aufnahme ausgegangen wird.
Um Zugang zu Bereichen zu erlangen, in welchen andere Prozesse limitierend für die Reaktionsrate sind, maßen wir zusätzlich auch die Ozonaufnahme in einem mit Shikimisäure beschichteten Durchflussreaktor. Sowohl der generelle Trend in der Abhängigkeit der Ozonaufnahme von der Feuchte, als auch die gemessene Reaktionsrate zweiter Ordnung ($(1.5 \pm \frac{1.5}{0.5}) \times 10^3$ $\mathrm{L\,mol^{-1}\,s^{-1}}$) stimmen gut mit den Ergebnissen aus der Röntgenmikroskopie überein. Unter Verwendung des Widerstandsmodells ist auch hier der analytische Ausdruck für reakto-diffusive Limitierung der Ozonaufnahme am besten zur Beschreibung der Ergebnisse geeignet. Bei längeren Reaktionszeiten sowie tiefen Feuchten erweist sich diese Methode der Auswertung jedoch als ungenügend. Daher verwendeten wir zusätzlich ein kinetisches Flussmodell um unsere Daten zu fitten, da dieses im Gegensatz zum Widerstandsmodell nicht auf der Annahme eines quasi-stationären Zustands beruht. Die Ergebnisse der Modellierung zeigen, dass einige der Eigenschaften der Ozonaufnahme, welche mit dem Widerstandsmodell nicht wiedergegeben werden

konnten, auf langsamer Diffusion von Shikimisäure beruhen könnten. Allerdings konnten auch mithilfe des komplexen Flussmodells nicht alle Details des Verlaufs der Ozonaufnahme korrekt wiedergegeben werden. Hier zeigt sich deutlich, dass die Implementierung der verschiedenen Prozesse im Flussmodell sowie die Methode der Fitoptimierung noch weiter verbessert werden müssen.

Im Rahmen dieser Arbeit konnten wir zeigen, dass komplizierte Fragestellungen wie der Zusammenhang von Aggregatzustand und Reaktivität von Aerosolteilchen am besten mit verschiedenen Methoden untersucht werden, um so möglichst viele unterschiedliche Informationen über das untersuchte System zu erhalten. Dies gilt im Besonderen bei der Verwendung komplexer Modelle zur Interpretation, da diese ohne experimentelle Einschränkungen zu stark unterbestimmt sind, um brauchbare Ergebnisse zu liefern.

CHAPTER 1

Introduction

1.1 What are aerosols and why do we care?

What are aerosols? An aerosol is an ensemble of solid and/or liquid particles suspended in a gas. Atmospheric aerosols can be either of natural origin or anthropogenic. Both of these can be further classified as either directly emitted (primary) or formed via gas-particle conversion processes in the atmosphere (secondary). As an aerosol undergoes various transformations during its lifetime in the atmosphere (e.g secondary material condensing on a primary particle), these distinctions become less and less meaningful when applied to the whole aerosol. It is therefore often more useful to apply the distinction by origin for individual aerosol components instead of the whole aerosol. Whether these components are particles or compounds depends on whether the aerosol is externally mixed, i.e. an ensemble of different but homogeneous particles in the gas phase, or internally mixed, in which case each particle consists of several compounds. Atmospheric particles range in size from a couple of nanometers up to tens or hundreds of micrometers. They can be separated into three modes: nuclei mode (< 0.1 µm), accumulation mode (0.1 to about 2.5 µm) and coarse mode (> 2.5 µm). The first two are also often grouped

into a single fine mode. While cloud droplets theoretically fall within the definition of aerosol particles, they are usually treated as a separate phenomenon in atmospheric science. Due to the higher settling velocity of larger particles, only particles with sizes in the fine mode range have the atmospheric lifetime to be transported globally (days up to weeks) (Seinfeld and Pandis, 1998). Aerosols contain both organic and inorganic compounds, the exact nature of which is greatly dependent on time and location. Figure 1.1 shows the large variation in non-refractory nitrate, sulfate, ammonium, chloride and organic content of particulate matter < 1 µm (PM_1) measured with an aerosol mass spectrometer (AMS) at various different locations (Zhang et al., 2007). Organic compounds make up between 18 and 70 % of measured particle mass in said study, while the fraction can rise as high as 90 % in tropical forested areas (Kanakidou et al., 2005). This organic fraction does not consist of only a few specific molecules, or even narrow classes of compounds, but comprises a large variety of different compounds. Current estimates put the amount of measured organic compounds in the atmosphere (including both gas and particle phase) in the range of 10000-100000, with an additional unknown

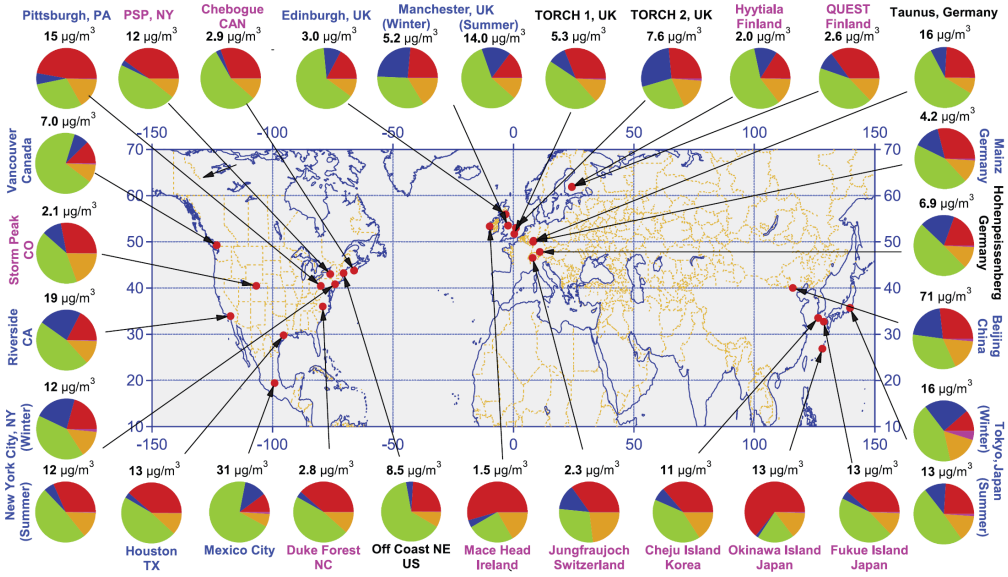

Figure 1.1: Overview of AMS datasets indicating the composition of non-refractory PM_1 with the following color-code: organics (green), sulfate (red), nitrate (blue), ammonium (orange), and chloride (purple). Font color of the location label indicates the type of sampling location: urban area (blue), < 100 miles downwind of major cities (black), and rural/remote area > 100 miles downwind (pink). Reproduced from Zhang et al. (2007).

number of unidentified compounds (Goldstein and Galbally, 2007). It is therefore common to use bulk properties to classify the organic fraction, such as volatility, oxygen to carbon (O:C) ratio, or solubility in water. The water soluble fraction comprises between 20 and 70 % of organic particulate matter (OPM) by mass and consists of carboxylic acids, polyols, polyphenols, sugars and other highly functionalized compounds (Rogge et al., 1993; Saxena and Hildemann, 1996; Decesari et al., 2000).

Why do we care? Aerosols affect us in two major ways: They take part in a variety of processes that influence our environment, and they may have a negative effect on human health. Among the prominent environmental processes is the influence of aerosols on the Earth's climate, which can be either direct, semi-direct or indirect. The direct effect describes the immediate interaction of atmospheric particles with radiation via scattering (cooling) and absorption (heating). There are two indirect effects. The presence of an increased number of atmospheric particles as cloud condensation nuclei may lead to a higher number density of cloud particles. This increases the albedo as the particle surface to volume ratio in the cloud increases (cloud albedo effect). Smaller cloud particles also decrease cloud precipitation efficiency, which leads to longer lifetimes (cloud lifetime effect). In the semi-direct aerosol effect, the absorption of solar radiation by aerosols heats the troposphere, which reduces relative humidity and can lead to the evaporation of clouds (Lohmann and Feichter, 2005). This classification was slightly changed in the last report by the Intergovernmental Panel on Climate Change (IPCC) (Boucher et al., 2013), where the effects are now separated into irradiance changes from aerosol-radiation interactions (ari) and irradiance changes from aerosol-cloud interactions (aci). Both of these are then further split into radiative forcing and adjustments. The ari radiative forcing corresponds to the direct aerosol effect, the ari adjustment to the semi-direct aerosol effect. The aci encompasses both the cloud albedo effect (radiative forcing) and the cloud lifetime effect (adjustments). According to Boucher et al. (2013), the current best estimate for the total effective radiative forcing by aerosols is $-0.9\ \mathrm{W\,m^{-2}}$.

Additionally, aerosols affect the trace gas composition of the atmosphere via chemical and physical multiphase processes. A major example for this is the heterogeneous hydrolysis of N_2O_5, which yields HNO_3 and is a net sink for reactive oxides of nitrogen ($NO_x \equiv NO + NO_2$). As NO_x react catalytically under consumption of volatile organic carbon to produce O_3 and thereby also OH, their

removal reduces the oxidative capacity of the atmosphere (Dentener et al., 1996; Thornton et al., 2003; Karagulian et al., 2006).

Due to their atmospheric lifetime of up to several weeks, aerosols can also transport condensed material over long distances. Such long-range transports are relevant in the biogeochemical cycle of e.g. iron, where dust is a major source of iron in the ocean (Duce and Tindale, 1991; Boyd and Ellwood, 2010). Aerosols can also transport biological matter such as reproductive materials, organisms, pathogens and their fragments (Griffin et al., 2001; Taylor et al., 2004; Elbert et al., 2007).

There are several ways, apart from distribution of pathogens, in which aerosol particles can affect human health. A good, brief overview of the health effects of particulate matter is given by Nel (2005). Exposure to fine particulate matter is linked to respiratory diseases including allergies (Nel et al., 1998; Samet et al., 2000; Bernstein et al., 2004), cardiovascular diseases (Peters et al., 2001; Pope et al., 2004) and lung cancer (Pope et al., 2002). Generally, particles in fine mode are more relevant for health effects as they can penetrate deeper into the respiratory system. As aerosols have such a wide ranging impact on our lives, it is important to understand their distribution, lifetimes and relevant properties affecting health and environment.

1.2 Aerosol aging – a change in properties?

During its lifetime in the atmosphere, an aerosol can change in chemical composition as well as ratio of material in the gas and condensed phase through various physical and chemical processes. If the change can be related to chemical reactions, the term 'aerosol aging' is often used to describe the transformation process. This encompasses changes caused by condensed phase reactions, reactive uptake, or gas phase reactions followed by gas-to-particle conversion of products (Rudich et al., 2007). Reactions involved in the aging of organic compounds are categorized as either fragmentation, oligomerization or functionalization reactions, depending on whether the carbon number of the product is larger, smaller or the same as for the reactant. (Jimenez et al., 2009).
Aging can change important particle properties, which in turn influence our environment and health. Chemical processing of aerosols can for example lead to 'browning' of the condensed phase material, i.e. an increase in mass absorption

coefficient (MAC) in the visible range. Such an effect has been observed for a variety of atmospherically relevant reactions such as exposure of secondary organic matter (SOM) to ammonia and ammonium salts (Bones et al., 2010; Laskin et al., 2010; Updyke et al., 2012), the acid-catalyzed aldol condensation of aldehydes and ketones (Nozière and Esteve, 2005), and reactive uptake of glyoxal by ammonium sulfate aerosol (Galloway et al., 2009). Due to the increase in MAC, browning influences the direct and semi-direct aerosol effect. Another important property of aerosol particles is hygroscopicity, as it governs the uptake of water and therefore influences their optical properties (direct aerosol effect), their effectiveness as cloud condensation nuclei (indirect aerosol effect) and their respiratory tract deposition. Hygroscopicity can either increase or decrease as compounds get oxidized (Varutbangkul et al., 2006; Vesna et al., 2008) due to the competing effects of fragmentation and functionalization, making the compounds more polar, vs. oligomerization, which leads to less polar compounds.
While particle size is a major factor controlling the influence of ambient aerosols on human health, other properties also play an important role, such as toxicity, allergenicity, mutagenicity and carcinogenicity of the different aerosol compounds. It is clear that aging can change the health effects of aerosols as it alters the chemical composition. This is, however, hard to quantify as usually not all reaction products can be identified and their composition often changes with the reaction conditions. Additionally, even for compounds where the reaction products are comparatively well known, such as the carcinogenic Benzo[a]pyrene, many of the by-products are not well characterized toxicologically (Pöschl, 2002). Two examples for known effects of aging on aerosol properties related to health are the increase in allergenic potential due to protein nitration (Franze et al., 2005) and the formation of toxic compounds from ozonolysis of cypermethrin (Segal-Rosenheimer and Dubowski, 2007).

1.3 Organic matter in aerosols – liquid or solid?

As mentioned in Section 1.1, particles rich in organics consist of a multitude of different compounds. As the melting point of an ideal substance is dependent on its mole fraction in a mixture, mixtures of several compounds can undergo strong melting point depression. Organic-rich particles are therefore preferably in a non-crystalline state (Marcolli et al., 2004), most often assumed to be liq-

uid. While the formation of amorphous solids (glasses) was already mentioned as a possibility (Pankow, 1994; Marcolli et al., 2004), the possible effects of this were traditionally disregarded and the organic-rich aerosol treated as well-mixed. This is particularly the case for SOA with respect to the time scale for its gas-particle equilibration (Pankow, 1994; Odum et al., 1996). However, recent studies have shown that high viscosity liquids and amorphous solids may be relatively common in the atmosphere and their properties significantly different from those of well-mixed liquids. In 2008, Zobrist et al. and Murray showed in laboratory experiments that proxies for organic matter (OM) in the atmosphere can form amorphous glasses under atmospherically relevant conditions, and speculated on possible impacts on water uptake, reactivity, and ice nucleation. In 2010, Virtanen et al. showed first evidence for formation of amorphous, solid, secondary organic aerosol (SOA). The study included both chamber and field measurements of SOA predominantly formed from terpenes in a Boreal forest environment.

What is a glass? The question *What is a glass?* should be easy to answer: a glass is an amorphous solid. Its formation is a kinetic phenomenon. Molecular motion slows down with decreasing temperature. If a liquid is cooled rapidly enough, the molecules rearrange so slowly that they cannot sample enough configurations in the available time to find the thermodynamically most preferable one, which would be crystalline (Debenedetti and Stillinger, 2001). Instead an amorphous solid forms. But when is a material solid? The phase transition from liquid to crystalline solid is a first order phase transition. These transitions show a discontinuity in the first derivative of the free energy with respect to a thermodynamic variable, e.g. in the enthalpy with respect to temperature. The freezing point is therefore well defined. This is different for the glass transition: the enthalpy changes strongly, but continuously as the material vitrifies (Figure 1.2). The point where the liquid and glassy parts of the enthalpy vs. temperature curve would intersect provides one definition for the glass transition temperature T_g. However, as previously described, the glass transition is a kinetic phenomenon and T_g depends on the cooling rate since the liquid has more or less time to sample different states. Another definition of T_g is via viscosity. In this case, a material is solid when its viscosity is $\geq 10^{12}$ Pas, and T_g therefore the temperature at which this viscosity is reached (Angell, 1995; Debenedetti and Stillinger, 2001). This definition is the one more commonly used in atmospheric studies, though all definitions of T_g are arbitrary and there is no international standard (Angell, 1995). According to Zo-

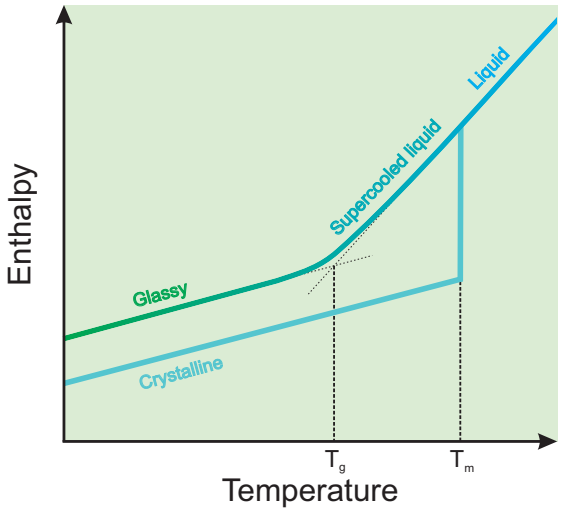

Figure 1.2: Comparison of phase transitions. The change in enthalpy with temperature at a constant pressure is equal to the isobaric heat capacity.

brist et al. (2008), the molecular mass of the investigated organics played a major role in their likelihood to form glasses as larger molecules have a higher glass transition temperature. Their estimated critical mass for a T_g relevant for atmospheric conditions is $\gtrsim 150\ \mathrm{g\,mol^{-1}}$.
However, temperature is not the only important environmental variable influencing glass transition. When mixing two compounds of different T_g, the resulting T_g of the mixture lies between the two initial T_g, which can often be described by the semi-empirical Gordon-Taylor formulation (Gordon and Taylor, 1952). This means that small compounds with low T_g can be mixed with high T_g substances to get mixtures of lower viscosity without changing temperature. Such substances are called plasticizers and are frequently used in the polymer industry. As water has a T_g of 136 K (Kohl et al., 2005), it serves as a plasticizer for water soluble organics. Relative humidity is therefore another factor which influences whether particles in the atmosphere are glassy or not. A good overview of glass formation in the context of atmospheric science is given in a review by Koop et al. (2011).

As described above, glasses have by definition viscosities $\geq 10^{12}$ Pas. This is fifteen orders of magnitude lower than for water at standard conditions (10^{-3} Pas). Koop et al. (2011) classifies materials up to 10^2 Pas as liquid, whereas materials of higher viscosity but below the threshold of $\geq 10^{12}$ Pas are called semi-solid. Over a

wide range, the viscosity is inversely coupled with both translational and rotational diffusion, i.e. the higher the viscosity of a material, the lower the diffusivity of molecules within. This relation is described by the Stokes-Einstein equation:

$$D = \frac{k_B T}{6\pi a \eta}, \tag{1.1}$$

where D is the diffusion coefficient, k_B the Boltzmann constant, a the radius of the diffusing object, and η the dynamic viscosity of the medium. The Stokes-Einstein equation is derived from Brownian motion of spherical particles in a homogeneous, viscous, medium. This means it is a prerequisite that the diffusing object is much larger than the constituents of the medium, which is not true for the diffusion of molecules. Nevertheless, it has been shown empirically that the Stokes-Einstein equation can be used over a large range of viscosities to determine self-diffusion coefficients of molecules in liquids. In this case however, viscosity and translational diffusion decouple at about $1.2T_g$, below which the Stokes-Einstein equation is no longer valid. Additionally, deviations from Eq. 1.1 can occur already much earlier for diffusion of small guest molecules in the matrix. It is therefore important to have independent measurements of diffusion coefficients. Power et al. (2013) convincingly illustrate this using the example of aqueous sucrose; they compare their own, measured viscosity data with data derived from diffusion coefficients via the Stokes-Einstein equation. While self-diffusion in an organic matrix can drop over more than 15 orders of magnitude to less than 10^{-20} $cm^2\,s^{-1}$ from liquid to glassy, the accompanying change in diffusivity of small guest molecules is much smaller. The diffusivity of water in an organic matrix for example decreases from 10^{-5} $cm^2\,s^{-1}$ to 10^{-10}-10^{-12} $cm^2\,s^{-1}$ at room temperature (Koop et al., 2011).

Many of the recently observed changes in aerosol properties and behavior with changing physical state can be related to this change in diffusivity, since they involve mass transfer within the condensed phase. This includes the uptake and release of water (Zobrist et al., 2011; Bones et al., 2012), formation, mixing and evaporation of SOA particles (Vaden et al., 2011; Perraud et al., 2012; Loza et al., 2013) and, more indirectly, reactivity, as will be explained in the following section.

1.4 Diffusivity and reactivity – how do they influence each other?

It is relatively straightforward to see how aging could influence the diffusivity of aerosol particles: reactions change the chemical composition of the aerosol and therefore T_g of the condensed phase. An increase in viscosity could e.g. be due to either formation of polymers with an increased molecular weight, decrease in hygroscopicity which decreases water uptake or volatilization of low molecular weight compounds. One example of a change in viscosity/diffusivity promoted by reaction is the increasing viscosity during ozonolysis of oleic acid (Hosny et al., 2013). But how does diffusivity influence reactivity?

It is well known that the physical state influences the reactive uptake of trace gases from the differences in reactivity between well-mixed liquid and crystalline particles. Both solubility and diffusivity are low in crystalline material. While the diffusion coefficients of water in ice are still relatively large with 2×10^{-11} to 0.22×10^{-11} $\mathrm{cm^2\,s^{-1}}$ between 263 K and 233 K (Bartels-Rausch et al., 2014), respectively, the diffusion coefficient of, e.g., Br in a NaCl crystal is only around 2×10^{-16} $\mathrm{cm^2\,s^{-1}}$, even at 20°C (Hess et al., 2009). Reactions of gas-phase reactants with crystalline particles are therefore generally assumed to be surface reactions without replenishment of the surface, such as uptake of HNO_3 on mineral dust (Vlasenko et al., 2009). There are two mechanisms commonly used to describe surface reaction kinetics: the Eley-Rideal mechanism, where gas phase molecules react directly with molecules at the surface upon collision, and the Langmuir-Hinshelwood mechanism, where the gas phase molecules need to be adsorbed on the surface prior to reaction. The majority of atmospheric surface reactions can be described with the Langmuir-Hinshelwood mechanism, which was first parameterized by Carslaw and Peter (1997) for reactions of $ClONO_2$ or HOCl with HCl on nitric acid trihydrate and sulfuric acid tetrahydrate surfaces. For interactions of gas-phase reactants with a liquid, which is well-mixed with respect to a non-volatile reactant, both surface and condensed phase reactions are possible. Following Ammann et al. (2013), we refer to the condensed phase as particle bulk; the non-volatile reactant is therefore called bulk phase reactant. For the reaction within the particle bulk, two different cases are usually considered. In the first case, the volatile reactant X, which is initially only found in the gas phase, diffuses quickly throughout the condensed phase in comparison to its reactivity with the

bulk phase reactant Y. In this case, the depletion of Y is treated as a regular, homogeneous, second-order reaction, as described by:

$$\frac{\mathrm{d}[\mathrm{Y}]_\mathrm{b}}{\mathrm{d}t} = -k^\mathrm{II}[\mathrm{X}]_\mathrm{b}[\mathrm{Y}]_\mathrm{b} = -k^\mathrm{II}H_\mathrm{X}p_\mathrm{X}[\mathrm{Y}]_\mathrm{b}, \tag{1.2}$$

where $[\mathrm{X}]_\mathrm{b}$ denotes the concentration of X in the particle bulk in $\mathrm{mol\,L^{-1}}$, k^II the second order rate constant in $\mathrm{L\,mol^{-1}\,s^{-1}}$, H_X the Henry constant of X in $\mathrm{mol\,L^{-1}\,atm^{-1}}$ and p_X the absolute pressure of X in the system in atm. In the second case X diffuses slowly in comparison to the reactivity with the bulk phase reactant. In this reacto-diffusion limited case a gradient of the volatile reactant X forms in the condensed phase and the reaction rate depends on the diffusion coefficient of X within the particle bulk. The depletion of Y can then be described by the following equation (Hanson et al., 1994):

$$\frac{\mathrm{d}[\mathrm{Y}]_\mathrm{b}}{\mathrm{d}t} = -H_\mathrm{X}RT\sqrt{D_\mathrm{X}k_\mathrm{b}^\mathrm{II}[\mathrm{Y}]_\mathrm{b}}\left[\coth\left(\frac{r}{l}\right) - \left(\frac{l}{r}\right)\right]\frac{S_\mathrm{p}}{V_\mathrm{p}}[\mathrm{X}]_\mathrm{g}, \tag{1.3}$$

where R is the gas constant in $\mathrm{L\,atm\,K^{-1}\,mol^{-1}}$, D_X the diffusion coefficient of X in the particle bulk in $\mathrm{cm^2\,s^{-1}}$, $[\mathrm{X}]_\mathrm{g}$ the gas phase concentration of X in $\mathrm{mol\,L^{-1}}$, S_p the particle surface in $\mathrm{cm^2}$ and V_p the particle volume in $\mathrm{cm^3}$. One example for a system which can be described by this equation is the reaction of $\mathrm{I^-}$ with $\mathrm{O_3}$ (Rouvière et al., 2010). The reacto-diffusive length l, given by

$$l = \sqrt{\frac{D_\mathrm{X}}{k_\mathrm{b}^\mathrm{II}[\mathrm{Y}]}}, \tag{1.4}$$

describes the characteristic length a molecule of X can diffuse into the particle bulk before it reacts (Hanson et al., 1994). If l is larger than the particle dimension, Eq. 1.3 simplifies to Eq. 1.2 as the reaction is no longer limited by diffusion. An example for this case is the reaction of HOCl and HCl on 60 wt % $\mathrm{H_2SO_4}$ particles of less than 0.12 µm radius at 3.6×10^{-6} atm HCl (Hanson and Lovejoy, 1996). Note that while Eq. 1.3 considers diffusivity as a factor in the reaction, only diffusion of the gas phase reactant X in the condensed phase is taken into account, while Y is considered well-mixed. Liquids can also undergo surface reactions. However, under the assumption that Y stays well-mixed, the surface is constantly and rapidly renewed, so that the whole of the particle bulk is affected. For cases where both surface and bulk reaction are rate determining, this can be taken into account via

resistor model formulations (Ammann et al., 2013).
The uptake coefficient, γ, describes the net probability that a gas phase molecule is taken up after collision with the surface. In the resistor model approach, each process involved in the uptake is represented by a normalized rate or a probability. The inverse uptake coefficient can be expressed by treating the reciprocal rates/probabilities mathematically as electrical resistors with regard to their occurrence (in parallel or serial connection). As a consequence of this, the slower of two subsequent processes is rate limiting, while between two parallel processes, the faster one is rate determining. The resistor model is only valid under steady-state conditions. For an overview of the different uptake processes and their associated resistances see Figure 1.3. While diffusion of the volatile molecule X in the gas phase is explicitly treated as a separate resistor, its condensed phase diffusion is included by selecting an appropriate expression for the particle bulk resistance. Self-diffusion of the non-volatile bulk phase molecule Y is not included at all. One

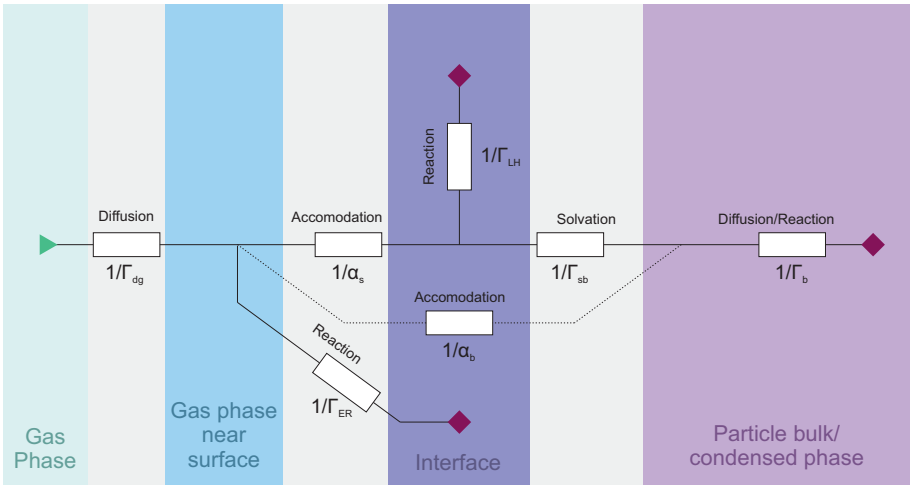

Figure 1.3: Overview of uptake processes in the resistor model. The white boxes represent the resistances associated with the process denoted in the label above.

case of simultaneous reaction on the surface and in the particle bulk is that of $ClONO_2$ and HCl on and in wet sulphuric acid particles (Hanson, 1998). Figure 1.4 illustrates the different reactive uptake processes. An example of reactivity of a crystalline solid vs. that of a liquid can be found in Moise and Rudich (2002), where the uptake of ozone to oleic and linoleic acid was found to decrease by about one order of magnitude when the physical state changed from liquid to crystalline solid.

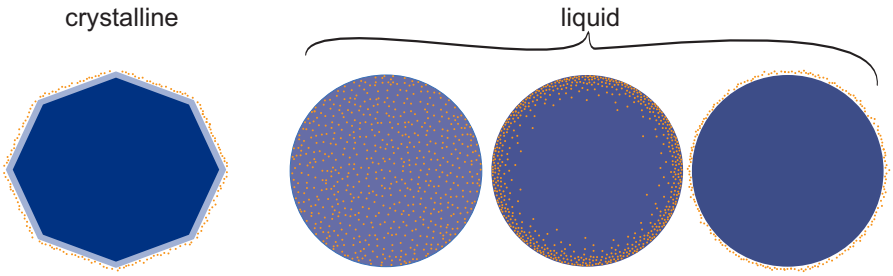

Figure 1.4: Overview of different fundamental reactive processes traditionally considered in heterogeneous atmospheric chemistry: surface reaction for a crystal and different cases of liquid phase reactions: reaction limited bulk reaction, reacto-diffusion limited bulk reaction and surface reaction.

So what about glassy particles? Diffusivity should be decreased compared to a liquid, but solubility is still relatively high. Using the solution of the diffusion equation in one dimension

$$x^2 = 2Dt, \tag{1.5}$$

where x is the mean distance from the starting point travelled by a molecule within the time t, and the diffusion constants given in Section 1.3, a bulk molecule would diffuse only 10^{-11} m in one minute, while water in crystalline ice would still diffuse $10^{-6} - 10^{-7}$ m, if not limited by reaction. It remains an open question how exactly the heterogeneous kinetics are influenced by limited diffusion of the bulk molecule and how the uptake process can be quantitatively described once the resistor model can no longer be used. The topic of how diffusivity limits reactivity has recently obtained increasing interest in atmospheric chemistry. Most approaches rely on the function of water as a plasticizer to change physical state, as this is a likely scenario for particles in an air parcel following an atmospheric trajectory.
A study by Shiraiwa et al. (2011), following the ozonolysis of proteins at different humidities and O_3 concentrations in a coated wall flow tube, demonstrated that decreases in reactivity could be linked to decreasing humidity. From comparison of their measured γ with modeling results they inferred that self-diffusion of the semi-solid proteins is low enough that a gradient develops not only for O_3 but also the proteins themselves. Similar conclusions were already drawn in 2002 by Smith et al. regarding the ozonolysis of oleic acid, where the size dependence of the uptake coefficient was ascribed to limited oleic acid diffusion in a matrix increasingly viscous due to the reaction products.
This case is usually not considered in heterogeneous kinetics and can not be de-

scribed by resistor model formulations. Shiraiwa et al. (2011) therefore used a multilayer kinetic model (KM-SUB, Shiraiwa et al., 2010) to model their experimental data. The same model was also applied in a variety of other studies on the topic. Shiraiwa et al. (2012a) measured and modeled the temporal evolution of γ for NO_3 uptake to dry levoglucosan and abietic acid. The uptake was measured in a rotating-wall flow-tube reactor. To extend the data on which to apply the model, they also included older experimental data of the dependence of the uptake coefficient on NO_3 concentration from Knopf et al. (2011). Shiraiwa et al. (2012b) investigated the nitration of bovine serum albumin in an aerosol flow tube. Here the model was fit to the dependence of NO_2 uptake on O_3 and NO_2 concentrations as well as the evolution of the fraction of nitrogen measured in the particle phase compared to the gas phase. All these studies came to similar conclusions regarding the formation of a gradient. A slightly different approach was taken by Zhou et al. (2013). Here, the depletion of benzo[a]pyrene via ozonolysis was measured. The benzo[a]pyrene was deposited on ammonium sulfate particles, which were then coated with a layer of SOA from α-pinene ozonolysis. Since the ozonolysis of benzo[a]pyrene is a surface reaction, the chemical needs to diffuse through the SOA-matrix to react. The pseudo-first order rate constant of the reaction as a function of O_3 concentration was measured at different humidities and then modeled with the KM-SUB model. The reactivity here also strongly depended on humidity and formation of a gradient of the reactant in the matrix was inferred from the model. Note that this is a special case as only the surface reaction is relevant, which simplifies the system as only one diffusivity has to be taken into account. Further evidence of decreasing reactivity with decreasing diffusivity in viscous substances was shown by Gallimore et al. (2011) for maleic acid ozonolysis, by Kuwata and Martin (2012) for organonitrogen formation from reaction of ammonia with α-pinene SOM, and by Slade and Knopf (2014) for OH uptake on levoglucosan. These studies do not specifically look at the underlying kinetic mechanisms.

While formation of a gradient in the bulk reactant currently seems to be the common assumption for glassy and semi-solid particles, it was never directly observed but only implied from the model results. This is somewhat problematic, as the KM-SUB model involves many not well constrained parameters and may therefore not be well defined for the limited amount of data sets it was fit to in the studies cited above. It is therefore possible that the solution is not unique and other kinetic scenarios are possible. The goal of this thesis is to investigate the ki-

netics of a model system, shikimic acid ozonolysis, in detail and find out how they are influenced by changes in diffusivity. Shikimic acid is a carboxylic acid with a cyclic double bond. It has been detected in biomass burning aerosol (Medeiros and Simoneit, 2008) and can be seen as a proxy for highly oxidized, water soluble OM. In particular we are interested in the question of whether and under which conditions a gradient forms. We therefore use a technique which should allow us to observe a gradient directly and provide a large number of flow tube data sets under different environmental conditions to restrict the degrees of freedom in the KM-SUB model.

1.5 Thesis outline

The aim of this thesis was to study the ozonolysis of shikimic acid to get a comprehensive understanding on how aerosol reactivity is influenced by mass transport limitations within the condensed phase. To understand how changes in physical state and therefore diffusivity influence the reaction kinetics, one first needs to understand if and how the physical state changes with environmental variables such as temperature and humidity.
Chapter 2 shows how to monitor the physical state and the retrieval of a corresponding parametrization of the water diffusion coefficient from measurements of water uptake on single, levitated particles. Apart from this kinetic information, parametrizations of density and shikimic acid concentration as a function of RH were retrieved. They are needed in the following chapters for rate law assessments.
The next two chapters, Chapter 3 and Chapter 4, then deal with how a change in RH and therefore mass transport influences the shikimic acid ozonolysis.
In Chapter 3, *in situ* scanning transmission X-ray microscopy (STXM) combined with near edge X-ray absorption fine structure (NEXAFS) spectroscopy was used to probe the ozonolysis. The advantage of this technique is that the degradation of shikimic acid can be directly observed in the condensed phase. Single particles below micron size can be probed and the resulting chemical maps yield spatially resolved information about the reaction.
In contrast to the STXM-NEXAFS experiments, the flow tube experiments described in Chapter 4 measure shikimic acid degradation indirectly by following the O_3 loss in the gas phase. Better time resolution, availability of the instrument and sensitivity to changes in the gas phase enabled us to probe different kinetic

regimes from those accessible via STXM-NEXAFS. The flow tube data was analyzed in two different ways: with a resistor model approach, assuming steady-state kinetics, and by applying the multilayer kinetic model KM-SUB. This allows us to assess how to best describe the reaction kinetics of the investigated system.

Bibliography

Ammann, M., Cox, R. A., Crowley, J. N., Jenkin, M. E., Mellouki, A., Rossi, M. J., Troe, J., Wallington, T. J.: Evaluated kinetic and photochemical data for atmospheric chemistry: Volume VI - heterogeneous reactions with liquid substrates, *Atmos. Chem. Phys*, **13**, 8045–8228, 2013.

Angell, C. A.: Formation of Glasses from Liquids and Biopolymers, *Science*, **267**, 1924–1935, 1995.

Bartels-Rausch, T., Jacobi, H. W., Kahan, T. F., Thomas, J. L., Thomson, E. S., Abbatt, J. P. D., Ammann, M., Blackford, J. R., Bluhm, H., Boxe, C., Domine, F., Frey, M. M., Gladich, I., Guzmán, M. I., Heger, D., Huthwelker, Th., Klán, P., Kuhs, W. F., Kuo, M. H., Maus, S., Moussa, S. G., McNeill, V. F., Newberg, J. T., Pettersson, J. B. C., Roeselová, M., Sodeau, J. R.: A review of air-ice chemical and physical interactions (AICI): liquids, quasi-liquids, and solids in snow, *Atmos. Chem. Phys.*, **14**, 1587–1633, 2014.

Bernstein, J. A. (Ed.), Alexis, N., Barnes, C., Bernstein, I. L., Nel, A., Peden, D., Diaz-Sanchez, D., Tarlo, S. M., Williams, P. B., and Bernstein, J. A.: Health effects of air pollution, *J. Allergy Clin. Immunol.*, **114**, 1116–1123, 2004.

Bones, D. L., Henricksen, D. K., Mang, S. A., Gonsior, M., Bateman, A. P., Nguyen, T. B., Cooper, W. J., and Nizkorodov, S. A.: Appearance of strong absorbers and fluorophores in limonene-O_3 secondary organic aerosol due to NH_4^+-mediated chemical aging over long time scales, *J. Geophys. Res. Atmos.*, **115**, D05203, 2010.

Bones, D. L., Reid, J. P., Lienhard, D. M., and Krieger, U. K.: Comparing the mechanism of water condensation and evaporation in glassy aerosol, *P. Natl. Acad. Sci. USA*, **109**, 11613–11618,

2012.

Boucher, O., Randall, D., Artaxo, P., Bretherton, C., Feingold, G., Forster, P., Kerminen, V.-M., Kondo, Y, Liao, H., Lohmann, U., Rasch, P., Satheesh, S. K., Sherwood, S., Stevens, B., and Zhang, X. Y.: Clouds and Aerosols. In: Climate Change 2013: The Physical Science Basis. Contribution of Working Group I to the Fifth Assessment Report of the Intergovernmental Panel on Climate Change, Cambridge University Press, Cambridge, United Kingdom and New York, NY, USA, 2013.

Boyd, P. W., Ellwood, M. J.: The biogeochemical cycle of iron in the ocean, *Nat. Geosci.*, **3**, 675–682, 2010.

Carslaw, K. S., and Peter, T.: Uncertainties in reactive uptake coefficients for solid stratospheric particles-I. Surface chemistry, *Geophys. Res. Lett.*, **24**, 1743, 1997.

Debenedetti, P. G., and Stillinger, F. H.: Supercooled liquids and the glass transition, *Nature*, **410**, 259-267, 2001.

Decesari, S., Facchini, M. C., Fuzzi, S., and Tagliavini, E.: Characterization of water-soluble organic compounds in atmospheric aerosol: a new approach, *J. Geophys. Res.-Atmos.*, **105**, 1481–1489, 2000.

Dentener, F. J., Carmichael, G. R., Zhang, Y., Lelieveld, J., and Crutzen, P. J.: Role of mineral aerosol as a reactive surface in the global troposphere, *J. Geophys. Res.-Atmos.*, **101**, 22869–22889, 1996.

Duce, R. A., Tindale, N. W.: Atmospheric Transport of Iron and Its Deposition in the Ocean, *Limnol. Oceanogr.*, **36**, 1715–1726, 1991.

Elbert, W., Taylor, P. E., Andreae, M. O., Pöschl, U.: Contribution of fungi to primary biogenic aerosols in the atmosphere: wet and dry discharged spores, carbohydrates, and inorganic ions, *Atmos. Chem. Phys.*, **7**, 4569–4588, 2007.

Franze, T., Weller, M. G., Niessner, R., and Pöschl, U.: Protein Nitration by Polluted Air, *Environ. Sci. Technol.*, **39**, 1673–1678, 2005.

Gallimore, P. J., Achakulwisut, P., Pope, F. D., Davies, J. F., Spring, D. R., and Kalberer, M.: Importance of relative humidity in the oxidative ageing of organic aerosols: case study of the ozonolysis of maleic acid aerosol, *Atmos. Chem. Phys.*, **11**, 12181–12195, 2011.

Galloway, M. M., Chhabra, P. S., Chan, A. W. H., Surratt, J. D., Flagan, R. C., Seinfeld, J. H., and Keutsch, F. N.: Glyoxal uptake on ammonium sulphate seed aerosol: reaction products and reversibility of uptake under dark and irradiated conditions, *Atmos. Chem. Phys.*, **9**, 3331–3345, 2009.

Goldstein, A. H., and Galbally, I. E.: Known and unexplored organic constituents in the earth's atmosphere, *Environ. Sci. Technol.*, **41**, 1514–1521, 2007.

Gordon, M., Taylor, J. S.: Ideal copolymers and the second-order transitions of synthetic rubbers. I. non-crystalline copolymers, *J. Appl. Chem.*, **2**, 493–500, 1952.

Griffin, D. W., Garrison, V. H., Herman, J. R., and Shinn, E. A.: African desert dust in the Caribbean atmosphere: Microbiology and public health, *Aerobiologia*, **17**, 203–213, 2001.

Hanson, D. R.: Reaction of $ClONO_2$ with H_2O and HCl in sulfuric acid and $HNO_3/H_2SO_4/H_2O$ mixtures, *J. Phys. Chem. A*, **102**, 4794–4807, 1998.

Hanson, D. R., Ravishankara, A. R., and Solomon, S.: Heterogeneous Reactions in Sulfuric-Acid Aerosols - a Framework for Model-Calculations, *J. Geophys. Res. Atmos.*, **99**, 3615–3629, 1994.

Hanson, D. R., and Lovejoy, E. R.: Heterogeneous Reactions in Liquid Sulfuric Acid: HOCl + HCl as a Model System, *J. Phys. Chem.*, **100**, 6397–6405, 1996.

Hess, M., Krieger, U. K., Marcolli, C., Peter, Th., Doremus, R. H., and Lanford, W. A.: Diffusion constants of Br in NaCl measured by Rutherford backscattering spectroscopy, *J. Appl. Phys.*, **105**, 124910, 2009.

Hosny, N. A., Fitzgerald, C., Tong, C., Kalberer, M., Kuimova, M. K., and Pope, F. D.: Fluorescent lifetime imaging of atmospheric aerosols: a direct probe of aerosol viscosity, *Faraday Discuss.*, **165**, 343–356, 2013.

Jimenez, J. L., Canagaratna, M. R., Donahue, N. M., Prevot, A. S. H., Zhang, Q., Kroll, J. H., DeCarlo, P. F., Allan, J. D., Coe, H., Ng, N. L., Aiken, A. C., Docherty, K. S., Ulbrich, I. M., Grieshop, A. P., Robinson, A. L., Duplissy, J., Smith, J. D., Wilson, K. R., Lanz, V. A., Hueglin, C., Sun, Y. L., Tian, J., Laaksonen, A., Raatikainen, T., Rautiainen, J., Vaattovaara, P., Ehn, M., Kulmala, M., Tomlinson, J. M., Collins, D. R., Cubison, M. J., Dunlea, E. J., Huffman, J. A., Onasch, T. B., Alfarra, M. R., Williams, P. I., Bower, K., Kondo, Y., Schneider, J., Drewnick, F., Borrmann, S., Weimer, S., Demerjian, K., Salcedo, D., Cottrell, L., Griffin, R., Takami, A., Miyoshi, T., Hatakeyama, S., Shimono, A., Sun, J. Y., Zhang, Y. M., Dzepina, K., Kimmel, J. R., Sueper, D., Jayne, J. T., Herndon, S. C., Trimborn, A. M., Williams, L. R., Wood, E. C., Middlebrook, A. M., Kolb, C. E., Baltensperger, U., and Worsnop, D. R.: Evolution of Organic Aerosols in the Atmosphere, *Science*, **326**, 1525–1529, 2009.

Kanakidou, M., Seinfeld, J. H., Pandis, S. N., Barnes, I., Dentener, F. J., Facchini, M. C., Van Dingenen, R., Ervens, B., Nenes, A., Nielsen, C. J., Swietlicki, E., Putaud, J. P., Balkanski, Y., Fuzzi, S., Horth, J., Moortgat, G. K., Winterhalter, R., Myhre, C. E. L., Tsigaridis, K., Vignati, E., Stephanou, E. G., and Wilson, J.: Organic aerosol and global climate modelling: a review, *Atmos. Chem. Phys.*, **5**, 1053–1123, 2005.

Karagulian, F., Santschi, C., and Rossi, M. J.: The heterogeneous chemical kinetics of N_2O_5 on $CaCO_3$ and other atmospheric mineral dust surrogates, *Atmos. Chem. Phys.*, **6**, 1373–1388, 2006.

Knopf, D. A., Forrester, S. M., Slade, J. H.: Heterogeneous oxidation kinetics of organic biomass burning aerosol surrogates by O_3, NO_2, N_2O_5, and NO_3, *Phys. Chem. Chem. Phys.*, **13**, 21050–21062, 2011.

Kohl, I., Bachmann, L., Hallbrucker, A., Mayer, E., and Loerting, T.: Liquid-like relaxation in hyperquenched water at $\leq$140 K, *Phys. Chem. Chem. Phys.*, **7**, 3210–3220, 2005.

Koop, T., Bookhold, J., Shiraiwa, M., and Pöschl, U.: Glass transition and phase state of organic compounds: dependency on molecular properties and implications for secondary organic aerosols in the atmosphere, *Phys. Chem. Chem. Phys.*, **13**, 19238–19255, 2011.

Kuwata, M. and Martin, S. T.: Phase of atmospheric secondary organic material affects its reactivity, *P. Natl. Acad. Sci. USA*, **109**, 17354–17359, 2012.

Laskin, J., Laskin, A., Roach, P. J., Slysz, G. W., Anderson, G. A., Nizkorodov, S. A., Bones, D. L., Nguyen, L. Q.: High-Resolution Desorption Electrospray Ionization Mass Spectrometry for Chemical Characterization of Organic Aerosols, *Anal. Chem.*, **82**, 2048-2058, 2010.

Lohmann, U., and Feichter, J.: Global indirect aerosol effects: a review, *Atmos. Chem. Phys.*, **5**, 715–737, 2005.

Loza, C. L., Coggon, M. M., Nguyen, T. B., Zuend, A., Flagan, R. C., and Seinfeld, J. H.: On the Mixing and Evaporation of Secondary Organic Aerosol Components, *Environ. Sci. Technol.*, **47**, 6173–6180, 2013.

Marcolli, C., Luo, B., and Peter, T.: Mixing of the Organic Aerosol Fractions: Liquids as the Thermodynamically Stable Phases, *J. Phys. Chem. A*, **108**, 2216–2224, 2004.

Medeiros, P. M. and Simoneit, B. R. T.: Source Profiles of Organic Compounds Emitted upon Combustion of Green Vegetation from Temperate Climate Forests, *Environ. Sci. Technol.*, **42**, 8310–-8316, 2008.

Moise, T., Rudich, Y.: Reactive Uptake of Ozone by Aerosol-Associated Unsaturated Fatty Acids: Kinetics, Mechanism, and Products, *J. Phys. Chem. A*, **106**, 6469-6476, 2002.

Murray, B. J.: Inhibition of ice crystallisation in highly viscous aqueous organic acid droplets, *Atmos. Chem. Phys.*, **8**, 5423–5433, 2008.

Nel, A.: Air pollution-related illness: Effects of particles, *Science*, **308**, 804–806, 2005.

Nel, A. E., Diaz-Sanchez, D., Ng, D.,Hiura, T., and Saxon, A.: Enhancement of allergic inflammation by the interaction between diesel exhaust particles and the immune system, *J. Allergy Clin. Immunol.*, **102**, 539–554, 1998.

Nozière, B., and Esteve, W.: Organic reactions increasing the absorption index of atmospheric sulfuric acid aerosols, *Geophys. Res. Lett.*, **32**, L03812, 2005.

Odum, J. R., Hoffmann, T., Bowman, F., Collins, D., Flagan, R. C., and Seinfeld, J. H.: Gas/particle partitioning and secondary organic aerosol yields, *Environ. Sci. Technol.*, **30**, 2580–2585, 1996.

Pankow, J. F.: An Absorption-Model of the Gas Aerosol Partitioning Involved in the Formation of Secondary Organic Aerosol, *Atmos. Environ.*, **28**, 189–193, 1994.

Perraud, V., Bruns, E. A., Ezell, M. J., Johnson, S. N., Yu, Y., Alexander, M. L., Zelenyuk, A., Imre, D., Chang, W. L., Dabdub, D., Pankow, J. F., and Finlayson-Pitts, B. J.: Nonequilibrium atmospheric secondary organic aerosol formation and growth, *P. Natl. Acad. Sci. USA*, **109**, 2836–2841, 2012.

Peters, A., Dockery, D. W., Muller, J. E., and Mittleman, M. A.: Increased Particulate Air Pollution and the Triggering of Myocardial Infarction, *Circulation*, **103**, 2810–2815, 2001.

Pope III, C. A, Burnett, R. T., Thun, M. J., Calle, E. E., Krewski, D., Ito, K., and Thurston, G. D., Lung cancer, cardiopulmonary mortality, and long-term exposure to fine particulate air pollution, *JAMA*, **287**, 1132–1141, 2002.

Pope III, C. A, Burnett, R. T., Thurston, G. D., Thun, M. J., Calle, E. E., Krewski, D., and Godleski, J. J.: Cardiovascular Mortality and Long-Term Exposure to Particulate Air Pollution: Epidemiological Evidence of General Pathophysiological Pathways of Disease, *Circulation*, **109**, 71-77, 2004.

Pöschl, U.: Formation and Decomposition of Hazardous Chemical Components Contained in Atmospheric Aerosol Particles, *J. Aerosol. Med.*, **15**, 203–212, 2002.

Power, R. M., Simpson, S. H., Reid, J. P., and Hudson, A. J.: The transition from liquid to solid-like behaviour in ultrahigh viscosity aerosol particles, *Chem. Sci.*, **4**, 2597–2604, 2013.

Rogge, W. F., Mazurek, M. A., Hildemann, L. M., Cass, G. R., and Simoneit, B. R. T.: Quantification of urban organic aerosols at a molecular-level – identification, abundance and seasonal-variation, *Atmos. Environ.*, **27**, 1309–1330, 1993.

Rouvière, A., Sosedova, Y., Ammann, M.: Uptake of Ozone to Deliquesced KI and Mixed KI/-NaCl Aerosol Particles, *J. Phys. Chem. A*, **114**, 7085–7093, 2010.

Rudich, Y., Donahue, N. M., and Mentel, T. F.: Aging of Organic Aerosol: Bridging the Gap Between Laboratory and Field Studies, *Annu. Rev. Phys. Chem.*, **58**, 321–352, 2007.

Samet, J. M., Dominici, F., Curriero, F. C., Coursac, I., and Zeger, S. L.: Fine Particulate Air Pollution and Mortality in 20 U.S. Cities, 1987–1994, *New Engl. J. Med.*, **343**, 1742–1749, 2000.

Saxena, P. and Hildemann, L.: Water-soluble organics in atmospheric particles: a critical review of the literature and application of thermodynamics to identify candidate compounds, *J. Atmos. Chem.*, **24**, 57–109, 1996.

Seinfeld, J. H., and Pandis, S. N.: Atmospheric chemistry and physics: from air pollution to climate change, John Wiley & Sons, 1998.

Segal-Rosenheimer, M., and Dubowski, Y.: Heterogeneous Ozonolysis of Cypermethrin Using Real-Time Monitoring FTIR Techniques, *J. Phys. Chem. C*, **111**, 11682–11691, 2007.

Shiraiwa, M., Pfrang, C., and Pöschl, U.: Kinetic multi-layer model of aerosol surface and bulk chemistry (KM-SUB): the influence of interfacial transport and bulk diffusion on the oxidation of oleic acid by ozone, *Atmos. Chem. Phys.*, **10**, 3673–3691, 2010.

Shiraiwa, M., Ammann, M., Koop, T., and Pöschl, U.: Gas uptake and chemical aging of semisolid organic aerosol particles, *P. Natl. Acad. Sci. USA*, **108**, 11003–11008, 2011.

Shiraiwa, M., Pöschl, U., and Knopf, D. A.: Multiphase Chemical Kinetics of NO_3 Radicals Reacting with Organic Aerosol Components from Biomass Burning, *Environ. Sci. Technol.*, **46**, 6630–6636, 2012a.

Shiraiwa, M., Selzle, K., Yang, H., Sosedova, Y., Ammann, M., and Pöschl, U.: Multiphase Chemical Kinetics of the Nitration of Aerosolized Protein by Ozone and Nitrogen Dioxide, *Environ. Sci. Technol.*, **46**, 6672–-6680, 2012b.

Slade, J. H., and Knopf, D. A.: Multiphase OH oxidation kinetics of organic aerosol: The role of particle phase state and relative humidity, *Geophys. Res. Lett.*, **41**, 5297–5306, 2014.

Smith, G. D., Woods, E., DeForest, C. L., Baer, T., Miller, R. E.: Reactive Uptake of Ozone by Oleic Acid Aerosol Particles: Application of Single-Particle Mass Spectrometry to Heterogeneous Reaction Kinetics, *J. Phys. Chem. A*, **106**, 8085–8095, 2002.

Taylor, P. E., Flagan, R. C., Miguel, A. G., Valenta, R., and Glovsky, M. M.: Birch pollen rupture and the release of aerosols of respirable allergens, *Clin. Exp. Allergy*, **34**, 1591–1596, 2004.

Thornton, J. A., Braban, C. F., and Abbatt, J. P. D.: N_2O_5 hydrolysis on sub-micron organic aerosols: the effect of relative humidity, particle phase, and particle size, *Phys. Chem. Chem. Phys.*, **5**, 4593–4603, 2003.

Updyke, K. M., Nguyen, T. B., and Nizkorodov, S. A.: Formation of brown carbon via reactions of ammonia with secondary organic aerosols from biogenic and anthropogenic precursors, *Atmos. Environ.*, **63**, 22–31, 2012.

Vaden, T. D., Imre, D., Beranek, J., Shrivastava, M., and Zelenyuk, A.: Evaporation kinetics and phase of laboratory and ambient secondary organic aerosol, *P. Natl. Acad. Sci. USA*, **108**, 2190–2195, 2011.

Varutbangkul, V., Brechtel, F. J., Bahreini, R., Ng, N. L., Keywood, M. D., Kroll, J. H., Flagan, R. C., Seinfeld, J. H., Lee, A., and Goldstein, A. H.: Hygroscopicity of secondary organic aerosols formed by oxidation of cycloalkenes, monoterpenes, sesquiterpenes, and related com-

pounds, *Atmos. Chem. Phys.*, **6**, 2367–2388, 2006.

Vesna, O., Sjogren, S., Weingartner, E., Samburova, V., Kalberer, M., Gäggeler, H. W., and Ammann, M.: Changes of fatty acid aerosol hygroscopicity induced by ozonolysis under humid conditions, *Atmos. Chem. Phys.*, **8**, 4683–4690. 2008.

Virtanen, A., Joutsensaari, J., Koop, T., Kannosto, J., Yli-Pirilä, P., Leskinen, J., Mäkelä, J. M., Holopainen, J. K., Pöschl, U., Kulmala, M., Worsnop, D. R., and Laaksonen, A.: An amorphous solid state of biogenic secondary organic aerosol particles, *Nature*, **467**, 824–827, 2010.

Vlasenko, A., Huthwelker, T., Gaggeler, H. W., and Ammann, M.: Kinetics of the heterogeneous reaction of nitric acid with mineral dust particles: an aerosol flowtube study, *Phys. Chem. Chem. Phys.*, **11**, 7921–7930, 2009.

Zhang, Q., Jimenez, J. L., Canagaratna, M. R., Allan, J. D., Coe, H., Ulbrich, I., Alfarra, M. R., Takami, A., Middlebrook, A. M., Sun, Y. L., Dzepina, K., Dunlea, E., Docherty, K., DeCarlo, P. F., Salcedo, D., Onasch, T., Jayne, J. T., Miyoshi, T., Shimono, A., Hatakeyama, S., Takegawa, N., Kondo, Y., Schneider, J., Drewnick, F., Borrmann, S., Weimer, S., Demerjian, K., Williams, P., Bower, K., Bahreini, R., Cottrell, L., Griffin, R. J., Rautiainen, J., Sun, J. Y., Zhang, Y. M., and Worsnop, D. R.: Ubiquity and dominance of oxygenated species in organic aerosols in anthropogenically-influenced Northern Hemisphere midlatitudes, *Geophys. Res. Lett.*, **34**, L13801, 2007.

Zhou, S., Shiraiwa, M., McWhinney, R. D., Pöschl, U., and Abbatt, J. P. D.: Kinetic limitations in gas-particle reactions arising from slow diffusion in secondary organic aerosol, *Faraday Discuss.*, **165**, 391–406, 2013.

Zobrist, B., Marcolli, C., Pedernera, D. A., and Koop, T.: Do atmospheric aerosols form glasses?, *Atmos. Chem. Phys.*, **8**, 5221–5244, 2008.

Zobrist, B., Soonsin, V., Luo, B. P., Krieger, U. K., Marcolli, C., Peter, Th., and Koop, T.: Ultraslow water diffusion in aqueous sucrose glasses, *Phys. Chem. Chem. Phys.*, **13**, 3514–3526, 2011.

CHAPTER 2

Electrodynamic balance measurements of thermodynamic, kinetic, and optical aerosol properties inaccessible to bulk methods

Published as: Steimer, S. S., Krieger, U. K., Te, Y.-F., Lienhard, D. M., Huisman, A. J., Ammann, M., and Peter, T.: Electrodynamic balance measurements of thermodynamic, kinetic, and optical aerosol properties inaccessible to bulk methods, *Atmos. Meas. Tech. Discuss.*, **8**, 689-719, 2015.

2.1 Abstract

Measurements of a single, levitated particle in an electrodynamic balance are an established tool for deriving thermodynamic and material data such as density, refractive index and activities of components of an aqueous solution under supersaturated conditions, where bulk measurements are not possible. The retrieval relies on combining mass-to-charge data and size data from light scattering. Here, we use a combination of low- and high-resolution Mie resonance spectroscopy to

obtain radius data, enabling an accurate size determination not only when the particle is in equilibrium, but also when it is out of equilibrium due to kinetic limitation of mass transport. With the data measured under non-equilibrium conditions, it is possible to retrieve the water diffusivity. A challenge is that the radius retrieval by comparing measured light scattering with Mie theory requires the knowledge of refractive index as a function of concentration. Here, we show an iterative retrieval of refractive index and size for compounds for which data cannot be obtained in the bulk either due to lack of sufficient amounts of sample or limited solubility. We demonstrate the measurement strategy and the retrieval of water activity, density, refractive index and water diffusivity for aqueous shikimic acid. Water diffusivity in concentrated shikimic acid decreases by 6 orders of magnitude at 250 K compared to that at room temperature.

2.2 Introduction

In 1935 Millikan stated that his famous oil drop experiment may be used as a very sensitive balance: "This device is simply an electrical balance in place of a mechanical one, and it will weigh accurately and easily to one ten-billionth of a milligram.". As early as 1960, Gucker and Rowell reported light scattering experiments on single levitated droplets in a Millikan-type setup. Since then, the techniques to measure charge-to-mass ratio and to size single, levitated droplets using light scattering have considerably matured and have been applied extensively to investigate atmospheric aerosols. For example, Tang and Munkelwitz used light scattering data of single aqueous salt droplets levitated in an electrodynamic balance (EDB) to determine water activity, density and refractive indicies (Tang and Munkelwitz, 1991, 1994). These measurements were made in quasi-thermodynamic equilibrium, whereas measurements of organic aerosol particles are often subject to kinetic limitations of water transport within the condensed phase. They also could take advantage of having enough sample material to perform bulk measurements, which allowed them to tie the experiments on single droplets to those obtained with more traditional techniques. Here we present a measurement and retrieval technique to obtain these data also for systems, which suffer from both: strong water uptake impedance and low solubility and/or limited amount of sample material.

We will illustrate our approach using shikimic acid as an example of a compound with comparably low solubility in water (180 $\mathrm{g\,L^{-1}}$ at 23 °C (Budavari, 1996),

corresponding to a mole fraction of 0.025 at saturation), so that the water activity of the saturated solution is close to 1 Shikimic acid is a carboxylic acid which has been detected in biomass burning aerosol (Medeiros and Simoneit, 2008). In recent years it has been shown that atmospheric organic matter can adopt an amorphous solid state (Zobrist et al., 2008; Virtanen et al., 2010).In the case that organic aerosols host chemical reactions, the gradual decrease in diffusivity from liquid to amorphous solid state is likely to cause a reduction in reaction rate, an effect well known for crystalline material (Moise and Rudich, 2002). First investigations of this effect for amorphous material have been made by Shiraiwa et al. (2011), Kuwata and Martin (2012) and Zhou et al. (2013). As we are using the ozonolysis of shikimic acid as a model system to investigate the interplay of physical and chemical kinetics (Chapter 3/Steimer et al., 2014 and Chapter 4), we need a detailed understanding of how relative humidity affects the physical state and diffusivity of water in shikimic acid. Additionally, the dependence of the concentration on water activity has to be known to determine initial bulk phase concentrations of shikimic acid for rate law assessments.

2.3 Experimental setup

The basic setup of the electrodynamic balance (EDB) has been described previously (Krieger et al., 2000; Colberg et al., 2004; Lienhard et al., 2014). Here, we summarize its basic features as follows: The EDB is placed in a double-jacketed glass chamber, with a cooling liquid flowing between the inner walls and an insulation vacuum between the outer walls. The temperature can be adjusted between 180 **K** and 320 **K**, covering the entire atmospheric range. A gas mixture is pumped continuously through the chamber to adjust/control relative humidity; the total pressure can be varied between 150 and 1000 **hPa**. The EDB is loaded by a single particle generator (Hewlett-Packard 51633A ink jet cartridge) filled with a dilute aqueous solution of the sample material. Relative humidity (RH) is measured by a capacitive RH probe with an integrated temperature sensor (U.P.S.I., France, model G-TUS.13R) mounted in the upper end cap of the EDB in close proximity to the levitated particle ($<$ 10 **mm** distance). The sensor was calibrated with deliquescence relative humidities of common salts and the saturation vapor pressure over ice at several temperatures. Capacitive RH probes are known to show some hysteresis and we conservatively estimate the accuracy to be no worse than $\pm 3\,\%$.

Four independent methods to characterize the aerosol particle are used: (i) the DC voltage applied to compensate the gravitational force is proportional to and used as a measure for the mass of the particle. (ii) The two-dimensional angular scattering pattern is measured over a scattering angle ranging from 78° to 101° and used to estimate the radius of the particle and to detect phase changes (Krieger and Meier, 2011). (iii) Mie resonance spectroscopy with a LED-"white"-light source for illumination is used to follow the radius change of a spherical particle (e.g. a liquid droplet); the wavelength of the LED is centered at the sodium D-Line (589 nm). The back-scattered light from the LED is collected by a spectrograph with a slow scan back-illuminated CCD array detector as an optical multichannel analyzer, for details see (Zardini et al., 2006; Zardini and Krieger, 2009). (iv) High resolution Mie resonance spectroscopy is used to measure size and refractive index simultaneously with high precision as described in more detail below.

The pioneering work of Ashkin and Dziedzic (1977) showed that size and refractive index of spherical particles may be obtained from Mie resonance spectra with very high precision. These Mie resonances, also called whispering gallery modes, have been observed for both elastic (e.g. Chylek et al., 1983; Ray et al., 1991) and inelastic scattering (e.g. Conwell et al., 1984; Preston and Reid, 2013). Conventionally, those spectra have been measured using a fixed wavelength, while drying or humidifying a particle and hence changing its size. In this approach, the Mie parameter, X, varies with time ($X(t) = 2\pi r(t)/\lambda$, with λ being the wavelength and r being the radius). This method becomes difficult to apply if the rate of size change is small, because several resonances are needed to compare measured spectra with Mie scattering computations. Hence, the technique can not be applied to compounds which need extended equilibration times because of low water diffusivity.

These problems do not arise when using a wavelength tunable light source. Huckaby et al. (1994) achieved relative errors in radius and refractive index of 3×10^{-5} and determined dispersion over the experimental spectral range. They analyzed the elastic scattering of a levitated particle at a scattering angle of $\pi/2$ and used two detectors in the planes parallel and perpendicular to the electric field vector of the incident beam stemming from a scanning ring dye laser. Conceptually, our approach (Te, 2011) is similar, but we use a narrow bandwidth tunable diode laser (TDL, New Focus, model Velocity 6312, tuning range 765–781 nm, linewidth (5 s) $<$ 5 MHz) instead of a dye laser and only one detector (Si photo diode, New Focus femtowatt photo receiver, model 2151), also at a scattering angle of $\pi/2$.

At this angle, transverse electric (TE) mode resonances can be detected in the plane perpendicular to the plane of polarization and transverse magnetic (TM) mode resonances can be detected in the plane parallel to the plane of polarization (Huckaby et al., 1994). To observe both TE- and TM-mode resonances separately, we use a $\lambda/2$-wave plate to rotate the polarization of the incoming beam and measure both polarizations sequentially. The detector samples the scattered light through the same optics that are used to collect the two-dimension angular scattering pattern. This has the advantage of measuring both phase function and Mie resonance spectra over the same scattering angle range and the disadvantage of a rather large collection angle for the Mie resonance spectroscopy. To account for intensity modulation caused by weak etaloning of the laser during scan and by some residual interference at the windows of the chamber we use a second detector to monitor the intensity of the reflected incoming beam as reference.
To avoid being limited by the accuracy of the wavelength reported by the commercial laser (approximately 0.1 nm) we use a custom-made wavemeter, following the design of Fox et al. (1999). As a reference laser we use a HeNe-laser (Stone et al., 2009), which is frequency stabilized using the design of Balhorn et al. (1972), yielding a relative uncertainty of the frequency stabilization of about 1 part in 10^7. Overall, the precision of the wavemeter is of the order of a few parts in 10^6, which was verified by measuring the hyperfine structure of the Rubidium D_2 line (centered at 780.04 nm), see Appendix A: Hyperfine spectrum of Rubidium.

In the present application we need the high resolution spectroscopy only to measure the radius and the real part of the refractive index at a number of discrete relative humidities, because we follow the radius change with the "white"-light resonance spectroscopy (see discussion in Section 2.4.2). Hence, we do analyze the spectra without any advanced fitting algorithm, but compare measured with calculated spectra manually, as shown in Figure 2.1. For an initial guess of size we use the measured phase function and apply Chylek's approximation of the spacing between resonances (Chylek, 1976, 1990). We find the best fit in size at a fixed refractive index testing a reasonable range of refractive indicies. In this way, we can easily determine the real part of the refractive index, m_{TDL}, with an accuracy of better than 0.005 and a corresponding accuracy in size of about 2×10^{-3} µm. This is sufficient for the type of experiments we are discussing here, since the limiting factor in the analysis of the data is the uncertainty in measured relative humidity. As mentioned above, we continuously measure low resolution Mie spectra using the LED centered at the wavelength of the sodium

D-line (589 nm). These spectra are then used to track changes in the radius. Since the radius at specific relative humidities is now known from the concurrent high resolution measurements, the refractive index at the sodium D-Line needed for retrieval of this data, m_{D}, can be determined by a Mie fit to the low resolution spectrum using dispersion, $m_{\mathrm{D}} > m_{\mathrm{TDL}}$, and the radius as a constraint.

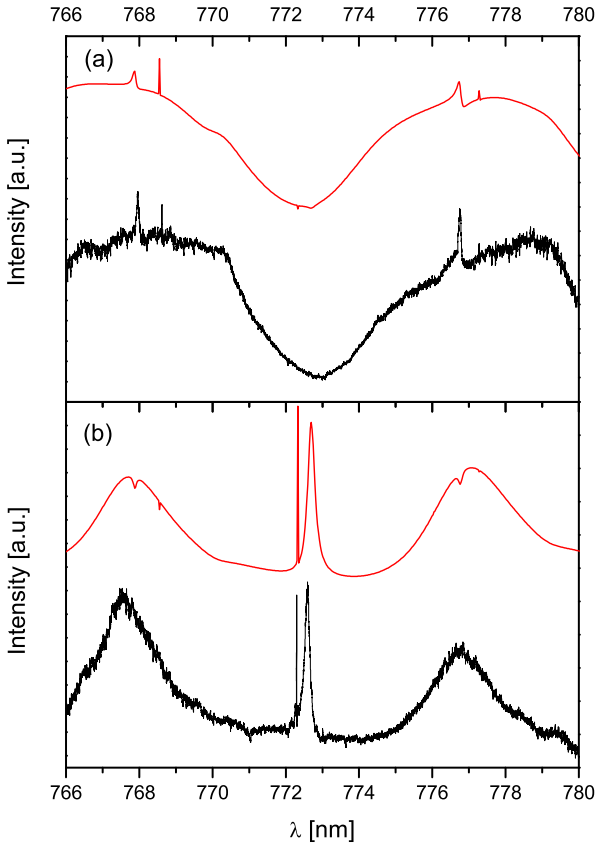

Figure 2.1: **(a)** TE and **(b)** TM spectra of shikimic acid particle under dry conditions at room temperature. Black line: experimental data. Red line: Mie calculation for a homogeneous particle with radius 7.756 µm and refractive index of 1.540.

2.4 Measurement strategy and data analysis

It has been shown previously that water diffusion constants can be deduced by combining stepwise changes in relative humidity with an accurate measurement

of the response in size of a levitated particle (Zobrist et al., 2011; Bones et al., 2012; Lienhard et al., 2014). In these previous investigations, additional data were available (refractive indicies, densities) helping to constrain the size retrieval. Here, we want to illustrate how we deduce the refractive index, density and water activity of an aerosol particle if such data are either completely lacking, or only available for a very limited concentration range.

2.4.1 Retrieval of mass growth factor

Traditionally, water activity data have been obtained utilizing the DC voltage compensating the gravitation force in the EDB (Tang and Munkelwitz, 1994; Zardini et al., 2008). As the exact charge of the particle is not known, only relative changes in mass can be inferred; a reference state is needed to calculate a mass growth factor. If bulk data cannot be obtained either because the amount of sample material is limited, or because solubility is very low, the voltage measured under dry conditions may serve as reference point. Figure 2.2 shows a typical experimental run performed at a constant temperature of 293.5 K.
A closer look at the data of Figure 2.2 shows that the accuracy of the voltage data is limited by spurious signals when a rapid change in relative humidity is applied. The DC voltage in our apparatus does not only compensate the gravitational force but also counteracts the Stokes force of the gas flow. Since the relative humidity is adjusted by changing the gas flow ratio of dry and humidified flow, very rapid changes lead to a response in the feedback loop adjusting the DC voltage, due to finite response of the mass flow controllers. This limits the accuracy of the voltage data to about ±2 V. The data in panel d showing the shift in resonance wavelength are free from this artifact.

For an aqueous aerosol particle with negligible vapor pressure of the solute(s) ($p_{\text{solute}} \leq 10^{-7}$ Pa) only water is exchanged between gas and particle phase. Under these conditions, the particle's mass growth factor can be directly inferred from the DC voltage compensating the gravitational force once the voltage under dry conditions has been measured. For aqueous organic systems, the kinetic uptake impedance due to slow water diffusion in semi-solid or glassy aerosol may substantially lengthen the time needed to reach thermodynamic equilibrium (whereas the transport of H_2O molecules through gas phase by ventilation and molecular diffusion is very fast). This becomes evident when plotting the DC-voltage data

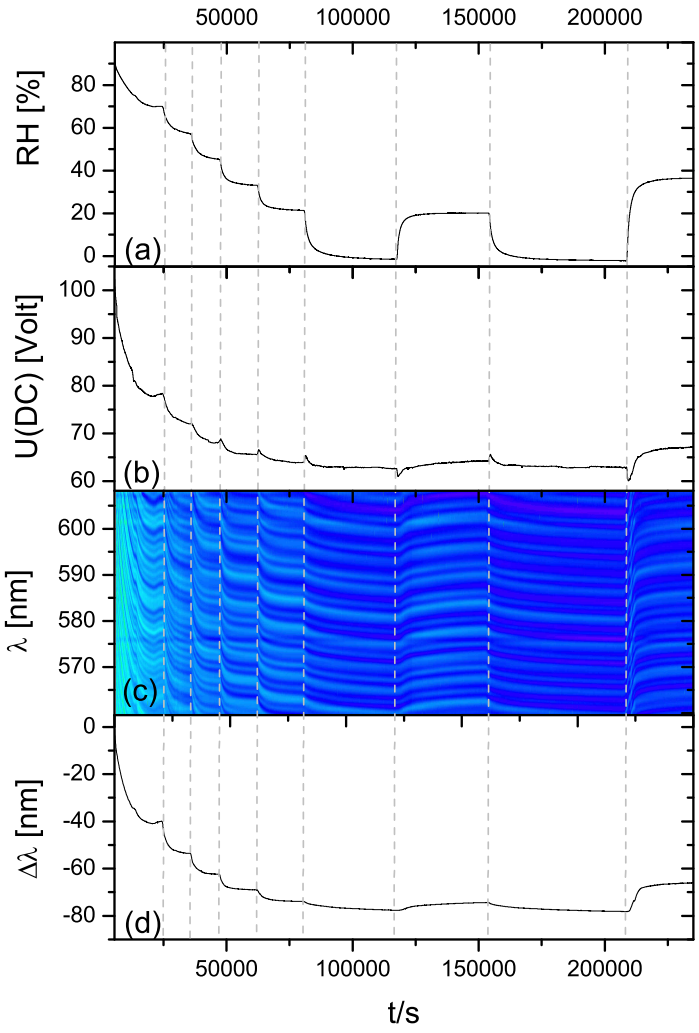

Figure 2.2: Typical experimental run on a shikimic acid particle with dry radius of 8.385 µm at $T = 293.5$ K. **(a)** Relative humidity measured close to the droplet. **(b)** DC voltage compensating gravitational force. **(c)** False color map of intensity of Mie resonance spectra measured with the LED (dark color low intensity, bright color high intensity). **(d)** Shift in wavelength $\Delta\lambda = \lambda(t) - \lambda_0$ of a resonance initially ($t = 0$) being observed at $\lambda_0 = 578.99$ nm. When this resonance leaves the spectral window, we continue by following another resonance as described by Zardini et al. (2006). Vertical dashed lines indicate humidity change.

of Figure 2.2 vs. relative humidity as done in Figure 2.3a and the inferred mass growth as in panel c. Below a relative humidity of about 0.3 the data show hysteresis loops, indicating delayed water uptake upon humidification and delayed water release upon drying (Zobrist et al., 2011). (Note that growth factors smaller than 1 derived from DC voltage data originate from the uncertainty of the measurement.) In this study, we determine the equilibrium data of e.g. growth factor, by considering the points where both branches of the loop overlap. Such overlap occurs either at higher RH, where equilibrium within the particle phase is fast, or after prolonged waiting time at low RH. An important measure of the properties of the solution, which we measure here, is its water activity $a_w = p^{sol}_{H_2O}(T)/p^{w}_{H_2O}(T)$, where $p^{sol}_{H_2O}$ is the H_2O vapor pressure of the solution and $p^{w}_{H_2O}$ is the H_2O vapor pressure of pure water, both at the same temperature. Under equilibrium conditions, the water activity (a_w) of the aqueous solution is equal to the measured relative humidity.
Note that the inverse of the mass growth factor ($g = m(\mathrm{RH})/m(\mathrm{RH}=0) = (m_s + m_{H_2O})/m_s$, with m_s being the mass of the solute and m_{H_2O} being the mass of water) is equal to the mass fraction of solute, w_s, since the change in mass is only caused by water uptake. We will use mass fraction data to constrain the density as explained in the following section.

2.4.2 Conversion of Mie resonance data to size and concentration

In Section 2.3 we explained how we obtain size and refractive index at a fixed RH using the high resolution Mie resonance spectra. When the particle radius is r_0 at time t_0, the LED based resonance shift, $\Delta\lambda$, shown in Figure 2.2d can be used to calculate the radius at other times, $r(t)$. If the refractive index did not change with size, the radius were easily obtained by noting that the Mie parameter, X, of a specific resonance, $X_0 = 2\pi r_0/\lambda_0$, stays constant,i.e. $X(t) = X_0$ (Zardini et al., 2006):

$$r(t) = \frac{(\lambda_0 + \Delta\lambda(t))r_0}{\lambda_0} \tag{2.1}$$

However, when the radius change is accompanied by a change in composition, e.g. uptake of water by an aqueous particle, the refractive index of the particle will change as well. A change in the real part of the refractive index from $m_{D,0}$ to

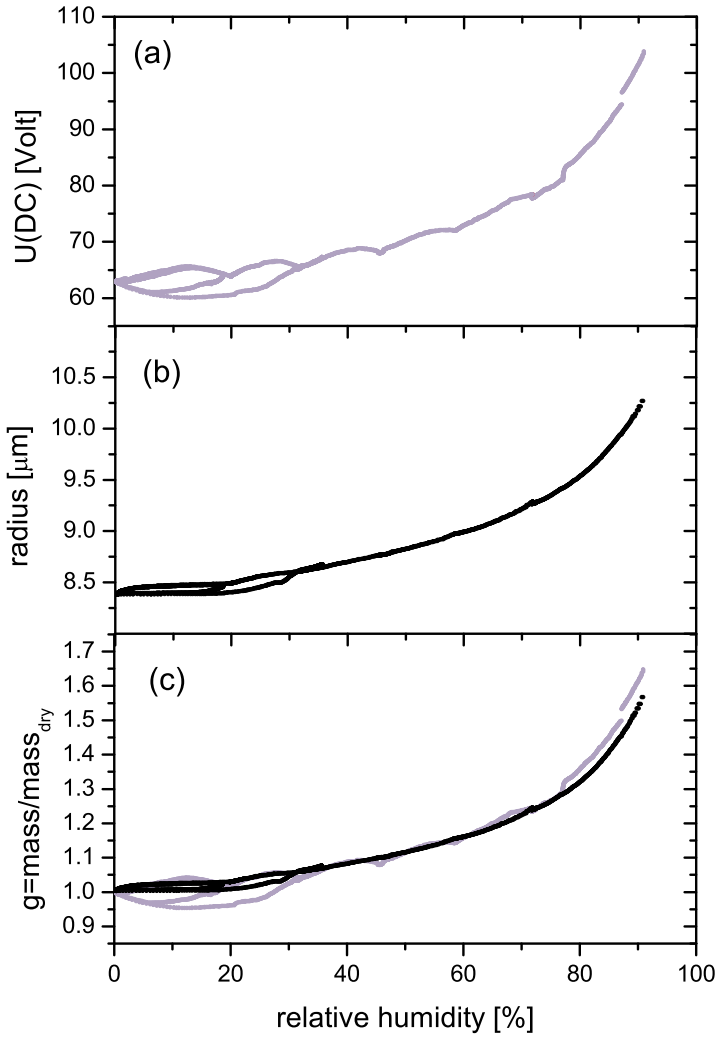

Figure 2.3: Data of Figure 2.2 plotted vs. relative humidity. **(a)** DC voltage compensating gravitational force. **(b)** Radius data, see text on how to obtain those from the data of Figure 2.2d. **(c)** Mass to dry mass ratio (growth factor g) calculated from both voltage (gray) and radius data (black).

$m_D(t)$ leads to an additional shift in the wavelength of a mode in the Mie resonance spectrum (Ray et al., 1991). The combined effect can be accounted for by solving iteratively Eq. 2.2 for the radius as a function of time:

$$r(t) = \left\{ 1 - K(m_D(t), X) \frac{m_D(t) - m_{D,0}}{m_{D,0}} \right\} \frac{(\lambda_0 + \Delta\lambda(t))r_0}{\lambda_0} \tag{2.2}$$

An iterative calculation is needed, because the implicit radius dependence of $m_D(t)$. In general, the proportionality factor, K, depends on refractive index and Mie parameter, but Ray et al. (1991) have shown that $K(m_D, X)$ varies between 0.94 and 0.96 for $1.30 \leq m_D \leq 2.00$ when the Mie parameter, X, is of the order of 100 as is the case in our experiments. In this study, we take K as a constant factor of 0.95.

Neither the refractive index of the solute nor its concentration dependence in aqueous solution are known a priori. Our approach for retrieving the concentration dependence of refractive index is therefore as follows. The dependence of the refractive index on concentration in aqueous solution is well described using the molar refractivity of the solute (Born and Wolf, 1980), i.e. the refractive index is linear with solute molarity. Hence the refractive index, $m_D(w_s)$, as a function of mass fraction of solute, w_s, is

$$m_D(w_s) = m_{D,H_2O} + \frac{\rho(w_s)}{\rho_s}(m_{D,s} - m_{D,H_2O})w_s, \tag{2.3}$$

with $m_{D,s}$ being the refractive index of the pure solute, ρ_s being the density of the pure solute and $\rho(w_s)$ being the density of the aqueous solution at the concentration w_s. To determine $m_{D,s}$, first the refractive index of an aqueous solution close to saturation concentration was measured using an Abbe type of refractometer at the sodium D-Line wavelength and the density at this concentration was measured using a pycnometer, see Figure 2.4. Since shikimic acid is not very soluble in water (mole fraction at saturation 0.025), these data alone lead to accurate estimates neither of the density of the solute, ρ_s (or the equivalent molar volume) nor of $m_{D,s}$ (or the molar refractivity). For other samples of interest the amount of material available may not be sufficient to perform these type of bulk experiments at all. Therefore, we measure a high resolution Mie resonance spectrum and use the concurrent LED spectrum as described in Section 2.3 at very dry conditions to determine the refractive indices, m_{TDL} and m_D. This yields the refractive index, $m_{D,s}$, of the solute as we assume $w_s = 1$.

What remains to be determined is the the density of the solution, $\rho(w_s)$. We assume that the density of binary aqueous solutions can be adequately approximated using the density of each the pure solute and water and the conventional volume additivity rule:

$$\rho(w_s) = \left(\frac{1 - w_s}{\rho_{H_2O}} + \frac{w_s}{\rho_s} \right)^{-1} \tag{2.4}$$

with ρ_{H_2O} the density of water, and ρ_s the density of the dry, amorphous solute. For a number of selected aqueous organic mixtures (e.g. citric acid) this approximation proved to be accurate within 1 % of the data (Lienhard et al., 2012).

The density of the pure solute, ρ_s, is the only remaining unknown. To determine it we start using an initial guess, which allows us to calculate the refractive index m_D for all concentrations using Eq. 2.4 and Eq. 2.3. Then $r(t)$ is computed solving Eq. 2.2. The mass growth factor can be calculated using the corresponding density and compared to the measured data shown in Figure 2.3c. If mass growth from the DC-voltage data do not agree with the mass growth calculated from the spectra, we update the initial guess of ρ_s and calculate again until the agreement is satisfactory. For aqueous shikimic acid solutions this leads to densities and refractive indices at a temperature of 293.5 K as shown in Figure 2.4. In addition to measuring the refractive index at very dry conditions we measured the refractive index at several humidities as shown in panel b. These measurements support the value of the refractive index of the pure solute, $m_{TDL,s}$, and through Eq. 2.3 also the density of the pure solute, ρ_s.
Note that we implicitly assume the particle to be homogeneous in the analysis outlined above. If there is a gradient in concentration within a particle due to kinetic uptake limitations, its refractive index will show a corresponding gradient. Strictly, Eq. 2.2 is no longer valid and a numerical modeling of the Mie resonance spectra of the inhomogeneous particle is needed to calculate the radius. However, the difference between the exact modeled results and those generated by applying Eq. 2.2 to an inhomogeneous particle is small compared to the uncertainty in our experiments (related to the accuracy of relative humidity probe) (Lienhard et al., 2014).

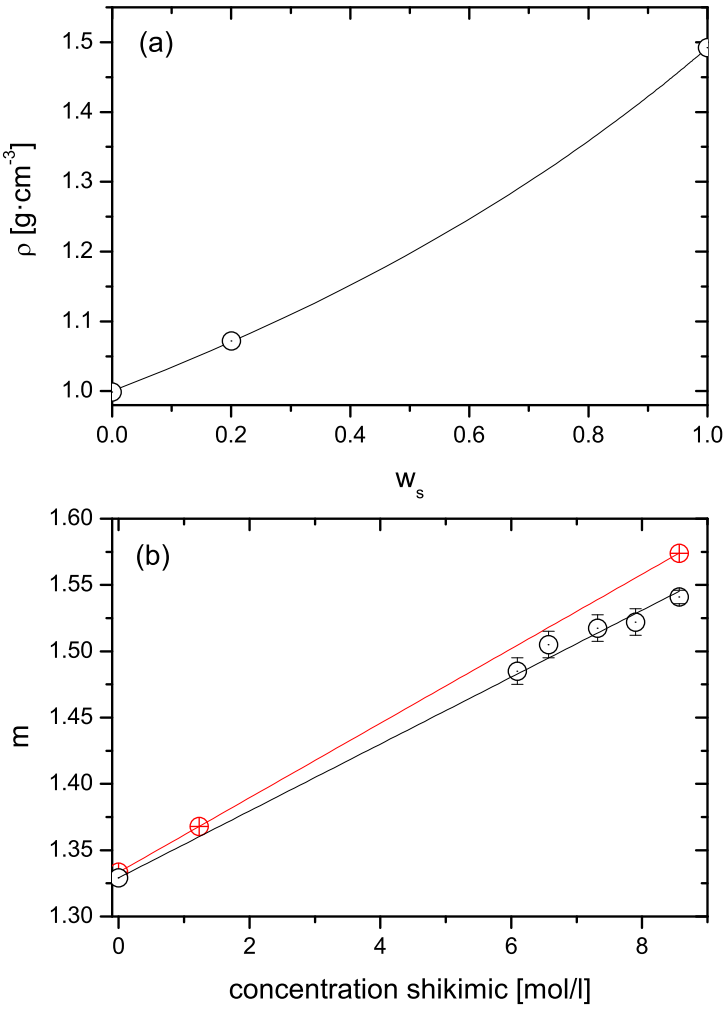

Figure 2.4: **(a)** Density vs. mass fraction parametrization of shikimic acid, the data point at $w = 0.2001$, $\rho = 1.072$ g cm^{-3} was measured with a pycnometer, the density of the solute $\rho_s = 1.492$ g cm^{-3} was determined as described in the text, the line is a plot of Eq. 2.4. **(b)** Refractive indices vs. molarity. m_{TDL} from high resolution Mie resonance spectra (black symbols), m_D (red symbols), lines are linear fits for the two different wavelengths to Eq. 2.3: $m_{TDL,H_2O} = 1.3292$, $m_{TDL,s} = 1.541$, $m_{D,H_2O} = 1.3334$, $m_{D,s} = 1.574$.

2.4.3 Parametrization of water activity

From the type of data shown in Figure 2.3c we derive a parametrization of water activity vs. concentration by noting that the inverse of the mass growth factor is equal to the mass fraction of solute (w_s) providing that only water is partitioning between gas and particle phase. The data of Figure 2.3c are replotted as w_s vs. a_w in Figure 2.5. From these data we select discrete data points at humidities at which the particle is in equilibrium with the gas phase by assuring that the same w_s was measured upon humidifying and drying. Such data were measured at 293.5 **K** for three different particles injected from fresh solutions. In addition, we used a commercial water activity meter (AquaLab, Model 3TE, Decagon Devices, U.S.A) to measure the a_w close to a saturated solution. As can be seen in Figure 2.5 and Figure 2.6, this data point does not significantly constrain the parametrization, because the water activity of the saturated solution is very close to that of pure water.

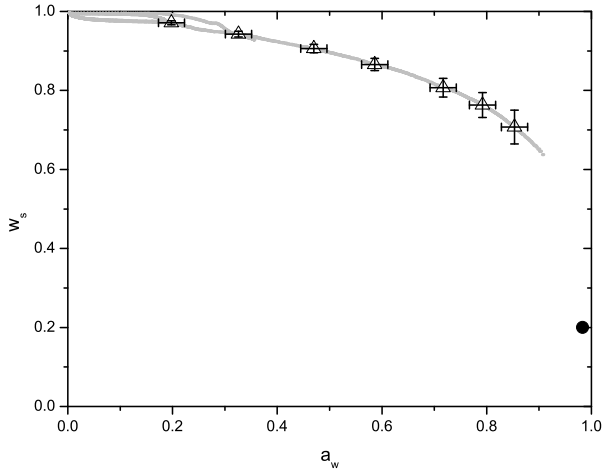

Figure 2.5: Mass growth data retrieved from radius measurements of Figure 2.3c plotted as mass fraction of solute vs. a_w (gray line). The Black circle marks a bulk data point of the saturated solution. We pick some discrete data points at humidities at which the particle is in equilibrium with the gas phase (open triangles) for fitting.

We convert w_s to mole fraction, x_s, and obtain the water activity coefficients, γ_w, according to

$$\ln \gamma_w = {x_s}^2 \left\{ (E + 3F + 5G) - (4F + 16G)x_s + 12G{x_s}^2 \right\} \tag{2.5}$$

(McGlashan, 1963), where E, F, G are fitting parameters (see Figure 2.6).

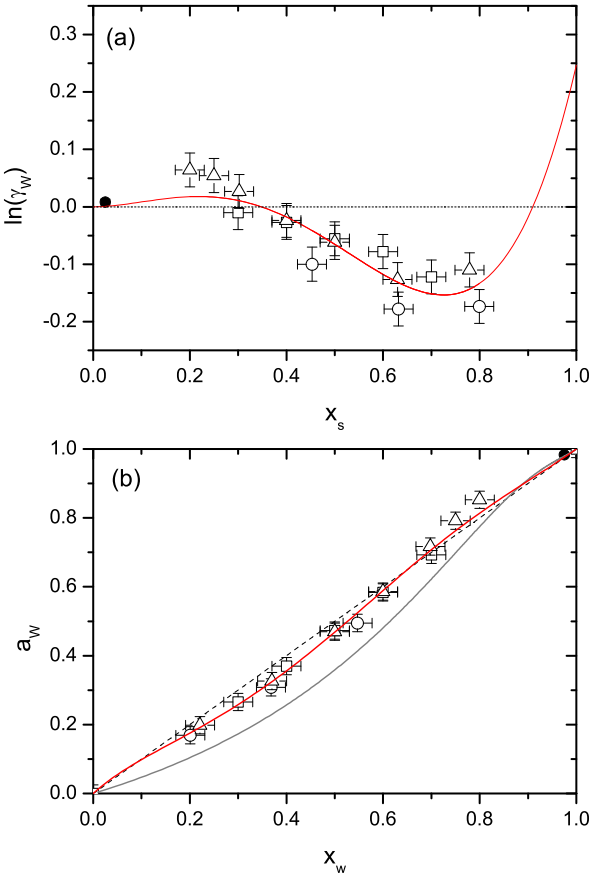

Figure 2.6: **(a)** natural logarithm of water activity coefficient γ_w vs. mole fraction of shikimic acid, symbols are data for three independent particles, solid circle is the bulk data point, dashed line represents ideal behavior (Raoult's law), red line is the fit of Eq. 2.5 to the data. **(b)** the same data plotted as water activity vs. mole fraction of water, the gray line is the prediction of the thermodynamic model AIOMFAC (Zuend et al., 2011).

The advantage of this approach is that once the fitting parameters are determined, it allows the direct calculation of the activity coefficient of the solute, γ_s, via the Duhem–Margules relations as (McGlashan, 1963):

$$\ln \gamma_s = {x_w}^2 \left\{ (E+F+G) - (4F+8G)x_w + 12G{x_w}^2 \right\} \tag{2.6}$$

For shikimic acid, we found $E = -0.182$, $F = -0.079$ and $G = 0.349$. It is evident from Figure 2.6 that the water activity of aqueous shikimic acid solutions deviate only slightly from ideal behavior (Raoult's law). The prediction by the thermodynamic model AIOMFAC (Zuend et al., 2011), namely lower a_w than ideal for high concentrations of shikimic acid and crossing to higher a_w than ideal at low shikimic acid concentration, is in agreement with the data. However, the magnitude of the deviation is smaller than predicted and the crossing is at higher concentration of shikimic acid than predicted.

We did not study the temperature dependence of a_w systematically, but obtained some data with known concentration at low temperatures at which the particles where equilibrated for a long time. We take the particle as equilibrated if the growth factor at a particular relative humidity is the same upon humidification and drying. The time required depends on both, RH and temperature. Our data suggest a positive slope of da_w/dT of about 4×10^{-3} K^{-1}, see Figure 2.7. Since our uncertainty in RH is almost as large as the shift in a_w over the temperature range considered in this study, we do not correct for the temperature dependence of a_w when analyzing the kinetic data at low temperatures.

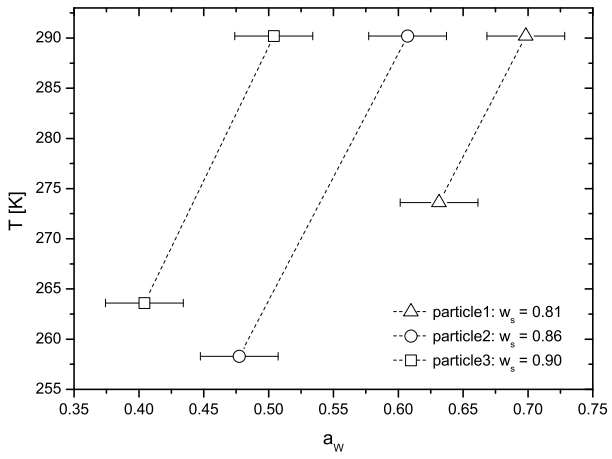

Figure 2.7: Temperature vs. a_w for three different particles at the fixed concentrations (as indicated in the legend). The dashed lines serve only as a guide to the eye.

2.4.4 Analysis of kinetic data

Having characterized the thermodynamics of aqueous shikimic acid, we will proceed analyzing the kinetic behavior, which is apparent in the raw data of Figure 2.3 as hysteresis loops (cf. discussion in Zobrist et al., 2011). In Section 2.4.4 we briefly summarize the numerical diffusion model used for analysis and report water diffusivity as a function of temperature and concentration in Section 2.4.4.

Diffusion model

In aqueous organic solutions, water acts as a plasticizer (Koop et al., 2011) and hence the water diffusion coefficient becomes concentration dependent. We solve the diffusion equation in spherical coordinates to retrieve concentration dependent water diffusion coefficients. Since our approach has been already described in depth by Zobrist et al. (2011), we will give only a brief summary of the underlying principles. The diffusion equation equation is

$$\frac{\partial n}{\partial t} = \nabla \left(D_{\mathrm{H_2O}}(n,T) \nabla n \right) = \frac{1}{r^2} \frac{\partial}{\partial r} \left(r^2 D_{\mathrm{H_2O}}(n,T) \frac{\partial n}{\partial r} \right) \tag{2.7}$$

where n is the number density of water molecules in the particle, t time and r the distance from the particle center. Due to the concentration dependence of $D_{\mathrm{H_2O}}$, the diffusion equation becomes non-linear. This leads to steep diffusion fronts instead of the more commonly known creeping diffusion tails (Crank, 1975). It also means that a general analytical solution for Eq. 2.7 cannot be found and the problem instead needs to be solved numerically. Our numerical model separates the particle into up to several thousands of individual shells. Growth and shrinkage of the particle are then the result of water diffusion between those shells. The change of the number of water molecules, ΔN_i, within the shell i is described by:

$$\Delta N_i = \left(f_{i-\frac{1}{2}} - f_{i+\frac{1}{2}} \right) \Delta t \tag{2.8}$$

where $f_{i-\frac{1}{2}}$ is the flux of water molecules from shell $i-1$ to shell i, whereas $f_{i+\frac{1}{2}}$ describes the flux of water molecules from shell i to shell $i+1$. The time interval,Δt, is chosen so that ΔN_i does not vary by more than a specified amount (usually $\leq 2\,\%$) within one time step. Shell thickness was adjusted dynamically to enable resolution of steep gradients when necessary. However, a minimum thickness of

0.3 nm was chosen to represent the size of a water molecule. Note that the surface layer of the particle (i.e. the outermost shell) is kept in equilibrium with the gas phase at all times so that mass transport is never limited by gas-phase diffusion. While gas phase diffusion under our experimental condition is indeed significantly faster than liquid phase diffusion (Zobrist et al., 2011), recent experiments have shown a difference between adsorption and desorption at low humidity (Lienhard et al., 2014). These findings question the assumption of the outermost shell always being in thermodynamic equilibrium, but this does not alter the derived diffusion coefficients significantly (Lienhard et al., 2014).

Water diffusivity parametrization of aqueous shikimic acid

To obtain water diffusivity from data as shown in Figure 2.2, we first calculate radius vs. time as explained in section Section 2.4.2 and then run the numerical model with different test dependencies of $\log D_{H_2O}$ vs. a_w until the fit appeared satisfactory upon manual inspection. An example of the fit results to the data of Figure 2.2 is shown in Figure 2.8.

As in Figure 2.8 a typical experiment at constant temperature covers a certain range of a_w where deviations from instantaneous equilibration are detectable. For a global fit of diffusivity we extract data points roughly spaced 0.15 in water activity within the humidity range covered by the specific experiment. The diffusivities at all investigated temperatures and concentrations are shown in Figure 2.9. We performed measurements between 294 and 251 K and from dry conditions to about 80 % RH. However, above about 50 % RH it is not possible to extract diffusion coefficients with our setup, because the rate of humidity change with time has an upper limit. This mainly due to limitations in gas flow because higher flow rates affect the stability of the particle in the EDB.

Analogous to Lienhard et al. (2014), we use a modified Vignes-type equation (Vignes, 1966) to empirically fit these data:

$$D_{H_2O} = (D^0_{H_2O})^{x_w \alpha} (D^0_s)^{1-x_w \alpha}, \tag{2.9}$$

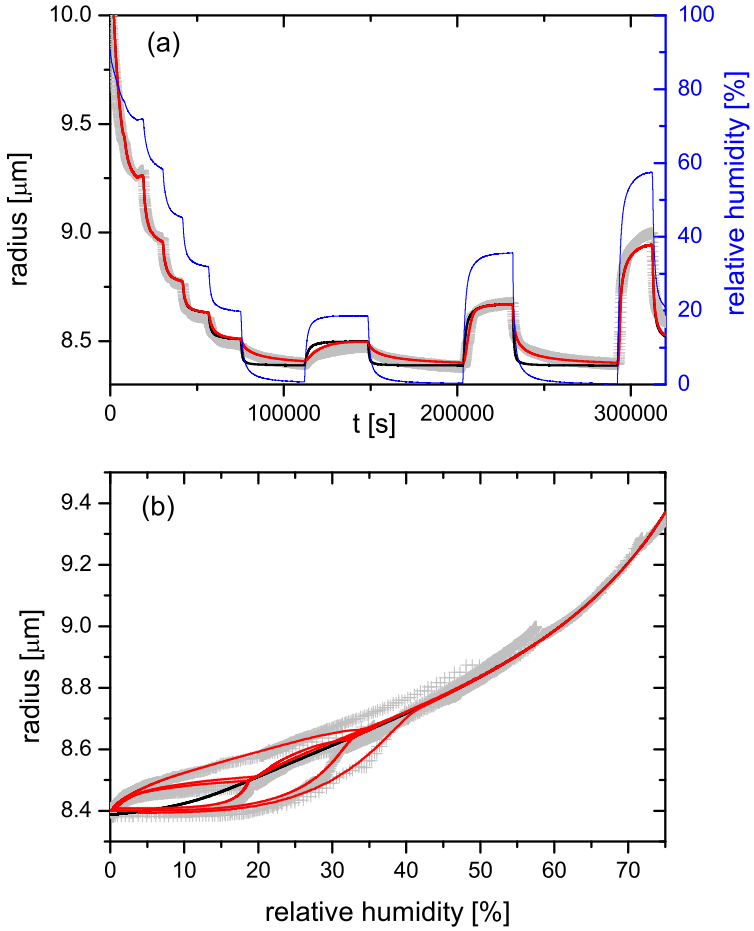

Figure 2.8: **(a)** data of Figure 2.2 converted to radius vs. time (gray crosses), equilibrium prediction of radius using the activity parametrization of section Section 2.4.3 (black line), diffusion model with a diffusivity of $\log(D_{H_2O}) = -8.7 - 7.5(1 - a_w)$ using the same activity parametrization (red line). Relative humidity (blue line) right axis. **(b)** The same data plotted vs. relative humidity. At RH $> 40\,\%$ at 293.5 K we observe no kinetic limitations to water uptake or release, while below that humidity kinetic limitations become clearly visible by the hysteresis loops in water uptake and release.

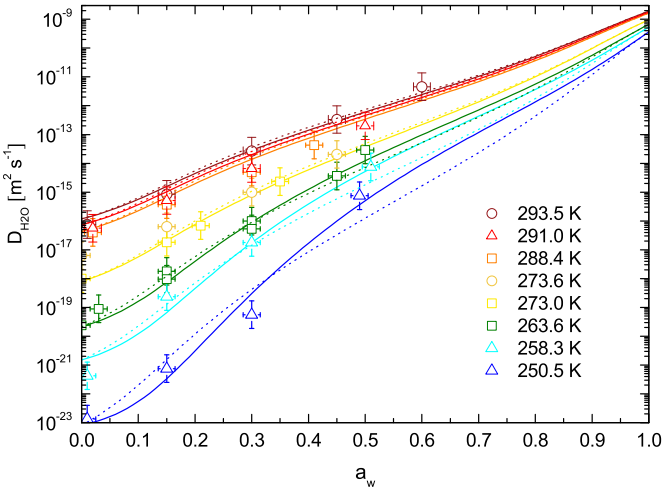

Figure 2.9: D_{H_2O} as a function of a_w for the investigated temperatures indicated by different colors. Different symbols represent different particles. The lines represent fits to equation Eq. 2.9. Solid lines were fitted with an α calculated according to Eq. 2.12, dotted lines with $\alpha = 1$

where $D^0_{H_2O}$ and D^0_s are the diffusion coefficients for water in pure water and pure shikimic acid, respectively. Their temperature dependence can be fitted to a Vogel-Fulcher-Tammann expression:

$$\log_{10}(D^0_{H_2O}) = -6.514 - \frac{387.4}{T - 118}, \tag{2.10}$$

and

$$\log_{10}(D^0_s) = -9.35 - \frac{542.8}{T - 211}, \tag{2.11}$$

where the numbers for $D^0_{H_2O}$ are taken from Smith and Kay (1999). To be consistent with our previous work (Lienhard et al., 2014), we introduce an empirical correction parameter α, having the form of an activity coefficient:

$$\ln(\alpha) = (1 - x_w)^2[C + 3D - 4D(1 - x_w)], \tag{2.12}$$

where C and D are temperature dependent:

$$C = -6.55 + 0.025T, \tag{2.13}$$

$$D = 7.122 - 0.0261T, \tag{2.14}$$

with $C(T > 273\ \mathrm{K}) = C(T = 273\ \mathrm{K})$ and $D(T > 258\ \mathrm{K}) = D(T = 258\ \mathrm{K})$.

The resulting fit to Eq. 2.9 with α calculated according to Eq. 2.12 is shown in Figure 2.9. The correction parameter α stays close to 1 in this fit for the entire temperature and concentration range. Therefore, we plot in Figure 2.9 also the contours for the different temperatures without correction (i.e. $\alpha = 1$). This leads to significant differences only for temperatures below 258 K. However, as only few data are available in this temperature range and the fits are just starting to diverge, measurements at even lower temperatures would be helpful for a more throughout comparison of the two fits. We conclude that the three parameter fit without correction term describe the water diffusivity satisfactorily.

2.5 Conclusions

We have presented a measurement and data retrieval technique to extract water activity, density, refractive index and water diffusion constants from mass-to-charge data and light scattering data of single levitated droplets in an electrodynamic balance. In particular, we have shown that an iterative procedure combining mass-to-charge data with Mie resonance spectroscopy yields robust data for parametrizing activity as well as water diffusivity. If solubility and amount of material available allow for bulk measurements of water activity, density and refractive index, these measurements provide constraints for simple mixing rules and hence further increase the accuracy of the parametrizations. However, even if measurements in the bulk are not available or possible, the technique presented here allows to constrain parametrizations well enough to be of use for atmospheric applications. We plan to use it to characterize secondary organic aerosol, which was collected on filters during oxidation experiments in which only about a milligram of material is available.

We studied aqueous shikimic acid aerosol in detail, a model system for aged, oxygenated organic aerosol. Due to its single carbon-carbon double bond it is especially well suited for heterogeneous chemistry studies, because the consumption of this double bond can be easily monitored with different spectroscopic techniques. Our study show that its activity in aqueous solution is close to ideal, i.e. almost follows Raoult's law. In addition the water diffusivity in aqueous shikimic

acid turns out to follow closely the simple empirical Vignes equation in contrast to other binary systems, e.g. aqueous citric acid. Comparison with secondary organic aerosol samples in the future will show how well shikimic acid represents the physical and chemical properties of atmospheric organic aerosol.

Appendix A: Hyperfine spectrum of Rubidium

To determine the accuracy and precision of the homemade wavemeter we measured the hyperfine structure of the Rubidium D_2 line. The laser emission of the TDL is split into two beams by a 50/50 beamsplitter. One beam is focused into a Rubidium glass cell, the other beam is fed into the Michelson interferometer to perform the wavelength measurement. A photodetector (New Focus Visible Femtowatt Photoreceiver, model 2151) is used to detect the fluorescence of the excited Rubidium. The fluorescence signal and the wavelength measurements are simultaneously recorded; the results is shown in Figure 2.10. The measured wavelengths deviate from literature data by not more than 0.001 nm.

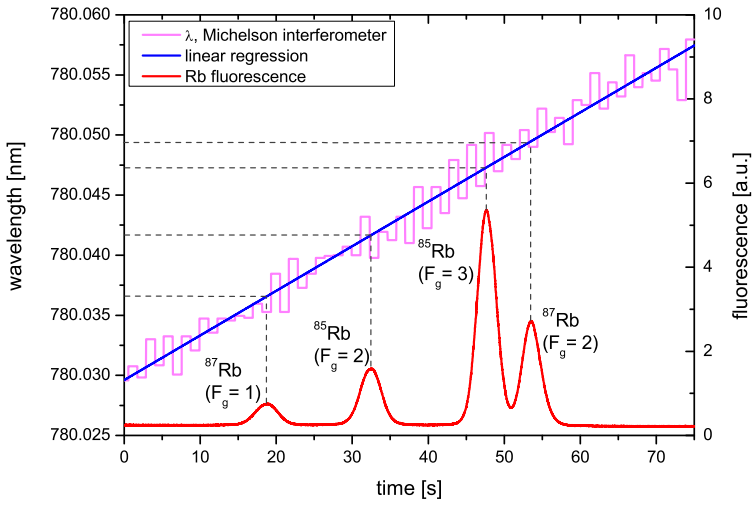

Figure 2.10: Rubidium spectroscopy using the piezoelectrically tuned TDL (780.030–780.060 nm with 0.0004 $\mathrm{nm\,s^{-1}}$ scan speed). The red line depicts the fluorescence light intensity and the violet line the Michelson interferometer wavelength measurement. The gray dashed lines denote the measured wavelengths needed to excite the D_2 transitions. With the resolution of our experiment the hyperfine splitting of the level $5P_{3/2}$ is not resolved, while the numbers F_g denotes the hyperfine levels of $5S_{1/2}$.

Acknowledgements

We acknowledge Andreas Zuend for calculating the AIOMFAC prediction of Figure 2.6 and Claudia Marcolli for helpful discussions. This work was supported by the ETH Research Grant ETH-0210-1 and by the Swiss National Science Foundation under project no. P2EZP2-152205. S. S. Steimer and M. Ammann acknowledge support by the EU FP7 project PEGASOS and by the University of Bern.

Bibliography

Ashkin, A. and Dziedzic, J. M.: Observation of Resonances in the Radiation Pressure on Dielectric Spheres, *Phys. Rev. Lett.*, **38**, 1351–1354, 1977.

Balhorn, R., Kunzmann, H., and Lebowsky, F.: Frequency Stabilization of Internal-Mirror Helium-Neon Lasers, *Appl. Opt.*, **11**, 742–744, 1972.

Bones, D. L., Reid, J. P., Lienhard, D. M., and Krieger, U. K.: Comparing the mechanism of water condensation and evaporation in glassy aerosol, *Proc. Natl. Acad. Sci.*, **109**, 11613–11618, 2012.

Born, M. and Wolf, E.: Principles of Optics, 6th edition, Pergamon Press, Oxford, UK, 1980.

Budavari, B. (Ed.): The Merck Index: an Encyclopedia of Chemicals, Drugs, and Biologicals, 12th edition, Merck & Co., Whitehouse Station, USA, 1458, 1996.

Chylek, P.: Partial-wave resonances and the ripple structure in the Mie normalized extinction cross section, *J. Opt. Soc. Am.*, **66**, 285–287, 1976.

Chylek, P., Ramaswamy, V., Ashkin, A., and Dziedzic, J. M.: Simultaneous determination of refractive index and size of spherical dielectric particles from light scattering data, *Appl. Opt.*, **22**, 2302–2307, 1983.

Chylek, P.: Resonance structure of Mie scattering: distance between resonances, *J. Opt. Soc. Am. A*, **7**, 1609–1613, 1990.

Colberg, C. A., Krieger, U. K., and Peter, Th.: Morphological Investigations of Single Levitated $H_2SO_4/NH_3/H_2O$ Aerosol Particles during Deliquescence/Efflorescence Experiments, *J. Phys.*

Chem. A, **108**, 2700–2709, 2004.

Conwell, P. R., Rushforth, C. K., Benner, R. E., and Hill, S. C.: Efficient automated algorithm for the sizing of dielectric microspheres using the resonance spectrum, *J. Opt. Soc. Am. A*, **1**, 1181–1187, 1984.

Crank, J.: The Mathematics of Diffusion, Clarendon Press, Oxford, 1975.

Fox, P. J., Scholten, R. E., Walkiewicz, M. R., and Drullinger, R. E.: A reliable, compact, and low-cost Michelson wavemeter for laser wavelength measurement, *Am. J. Phys.*, **67**, 624–630, 1999.

Gucker, F. T. and Rowell, R. L.: The angular variation of light scattered by single dioctyl phthalate aerosol droplets, Discuss. Faraday Soc., **30**, 185–191, 1960.

Huckaby, J. L., Ray, A. K., and Das, B.: Determination of size, refractive index, and dispersion of single droplets from wavelength-dependent scattering spectra, *Appl. Opt.*, **33**, 7112–7125, 1994.

Koop, T., Bookhold, J., Shiraiwa, M., and Pöschel, U.: Glass transition and phase state of organic compounds: dependency on molecular properties and implications for secondary organic aerosols in the atmosphere, *Phys. Chem. Chem. Phys.*, **13**, 19238–19255, 2011.

Krieger, U. K., Colberg, C. A., Weers, U., Koop, T., and Peter, Th.: Supercooling of single H_2SO_4/H_2O aerosols to 158 K: No evidence for the occurrence of the octahydrate, *Geophys. Res. Lett.*, **27**, 2097–2100, 2000.

Krieger, U. K. and Meier, P.: Observations and calculations of two-dimensional angular optical scattering (TAOS) patterns of a single levitated cluster of two and four microspheres, *J. Quant. Spectr. Rad. Trans.*, **112**, 1761–1765, 2011.

Kuwata, M., and Martin, S. T.: Phase of atmospheric secondary organic material affects its reactivity, *Proc. Natl. Acad. Sci.*, **109**, 17354–17359, 2012.

Lienhard, D. M., Bones, D. L., Zuend, A., Krieger, U. K., Reid, J. P., and Peter, T.: Measurements of Thermodynamic and Optical Properties of Selected Aqueous Organic and Organic-Inorganic Mixtures of Atmospheric Relevance, *J. Phys. Chem. A*, **116**, 9954–9968, 2012.

Lienhard, D. M., Huisman, A. J., Bones, D. L., Te, Y.-F., Luo, B. P., Krieger, U. K., and Reid, J. P.: Retrieving the translational diffusion coefficient of water from experiments on single levitated aerosol droplets, *Phys. Chem. Chem. Phys.*, **16**, 16677–16683, 2014.

McGlashan, M. L.: Deviations from Raoult's Law, *J. Chem. Edu.*, **40**, 516–518, 1963.

Medeiros, P. M. and Simoneit, B. R. T.: Source Profiles of Organic Compounds Emitted upon Combustion of Green Vegetation from Temperate Climate Forests, *Environ. Sci. Technol.*, **42**, 8310–-8316, 2008.

Millikan, R. A.: Electrons (+ and -), protons, photons, neutrons and cosmic rays Cambridge University Press, Cambridge, UK, 1935.

Moise, T., and Rudich, Y.: Reactive Uptake of Ozone by Aerosol-Associated Unsaturated Fatty Acids: Kinetics, Mechanism, and Products, J. *Phys. Chem. A*, **106**, 6469–6476, 2002.

Preston, T. C. and Reid, J. P.: Accurate and efficient determination of the radius, refractive index, and dispersion of weakly absorbing spherical particle using whispering gallery modes, *J. Opt. Soc. Am. B*, **30**, 2113–2122, 2013.

Ray, A. K., Soury, A., Davis, E. J., and Allen, T. M.: Precision of light scattering techniques for measuring optical parameters of microspheres, *Appl. Opt.*, **30**, 3974–3983, 1991.

Shiraiwa, M., Ammann, M., Koop, T., and Pöschl, U.: Gas uptake and chemical aging of semisolid organic aerosol particles, *Proc. Natl. Acad. Sci.*, **108**, 11003-–11008, 2011.

Smith, R. S. and Kay, B. D.: The existence of supercooled liquid water at 150 K, *Nature*, **398**, 788–791, 1999.

Steimer, S. S., Lampimäki, M., Coz, E., Grzinic, G., and Ammann, M.: The influence of physical state on shikimic acid ozonolysis: a case for in situ microspectroscopy, *Atmos. Chem. Phys.*, **14**, 10761–10772, 2014.

Stone, J. A., Decker, J. E., Gill, P., Juncar, P., Lewis, A., Rovera, G. D., and Viliesid, M.: Advice from the CCL on the use of unstabilized lasers as standards of wavelength: the helium–neon laser at 633nm, *Metrologia*, **46**, 11–18, 2009.

Tang, I. N. and Munkelwitz, H. R.: Simultaneous Determination of Refractive Index and Density of an Evaporating Aqueous Solution Droplet, *Aerosol Sci. Technol.*, **15**, 201–207, 1991.

Tang, I. N. and Munkelwitz, H. R.: Water activities, densities, and refractive indices of aqueous sulfates and sodium nitrate droplets of atmospheric importance, *J. Geophys. Res.*, **99**, 18,801–18,808, 1994.

Te, Y.-F.: Mie resonance spectroscopy of single levitated particle, MSc Thesis, University of Zurich, http://www.physik.uzh.ch/groups/schilling/bama/MATe.pdf, 2011.

Vignes, A.: Diffusion in Binary Solutions. Variation of Diffusion Coefficient with Composition *Ind. Eng. Chem. Fundamen.*, **5**, 189–199, 1966.

Virtanen, A., Joutsensaari, J., Koop, T., Kannosto, J., Yli-Pirilä, P., Leskinen, J., Mäkelä, J. M., Holopainen, J. K., Pöschl, U., Kulmala, M., Worsnop, D. R., and Laaksonen, A.: An amorphous solid state of biogenic secondary organic aerosol particles, *Nature*, **467**, 824–827, 2010.

Zardini, A. A., Krieger, U. K., and Marcolli, C.: White light Mie resonance spectroscopy used to measure very low vapor pressures of substances in aqueous solution aerosol particles, *Opt. Express*, **14**, 6951–6962, 2006.

Zardini, A. A., Sjogren, S., Marcolli, M., Krieger, U. K., Gysel, M., Weingartner, E., Baltensperger, U., and Peter, T.: A combined particle trap/HTDMA hygroscopicity study of mixed inorganic/organic aerosol particles *Atmos. Chem. Phys.*, **8**, 5589–5601, 2008.

Zardini, A. A. and Krieger, U. K.: Evaporation kinetics of a non-spherical, levitated aerosol particle using optical resonance spectroscopy for precision sizing, *Opt. Express*, **17**, 4659–4669, 2009.

Zhou, S., Shiraiwa, M., McWhinney, R. D., Pöschl, U., and Abbatt, J. P. D.: Kinetic limitations in gas-particle reactions arising from slow diffusion in secondary organic aerosol, *Faraday Discuss.*, **165**, 391–406, 2013.

Zobrist, B., Marcolli, C., Pedernera, D. A., and Koop, T.: Do atmospheric aerosols form glasses?, *Atmos. Chem. Phys.*, **8**, 5221–5244, 2008.

Zobrist, B., Soonsin, V., Luo, B. P., Krieger, U. K., Marcolli, C., Peter, Th., and Koop, T.: Ultra-slow water diffusion in aqueous sucrose glasses, *Phys. Chem. Chem. Phys.*, **13**, 3514–3526, 2011.

Zuend, A., Marcolli, C., Booth, A. M., Lienhard, D. M., Soonsin, V., Krieger, U. K., Topping, D. O., McFiggans, G., Peter, T., and Seinfeld, J. H.: New and extended parameterization of the thermodynamic model AIOMFAC: calculation of activity coefficients for organic-inorganic mixtures containing carboxyl, hydroxyl, carbonyl, ether, ester, alkenyl, alkyl, and aromatic functional groups, *Atmos. Chem. Phys.*, **11**, 9155–9206, 2011. http://www.aiomfac.caltech.edu

CHAPTER 3

The influence of physical state on shikimic acid ozonolysis: a case for in situ microspectroscopy

Published as: Steimer, S. S., Lampimäki M., Coz, E., Grzinic, G., and Ammann, M.: The influence of physical state on shikimic acid ozonolysis: a case for in situ microspectroscopy, *Atmos. Chem. Phys.*, **14**, 10761-10772, 2014.

3.1 Abstract

Atmospheric soluble organic aerosol material can become solid or semi-solid. Due to increasing viscosity and decreasing diffusivity, this can impact important processes such as gas uptake and reactivity within aerosols containing such substances. This work explores the dependence of shikimic acid ozonolysis on humidity and thereby viscosity. Shikimic acid, a proxy for oxygenated reactive organic material, reacts with O_3 in a Criegee-type reaction. We used an environmental microreactor embedded in a Scanning Transmission X-ray Microscope (STXM) to probe this oxidation process. This technique facilitates in situ measurements with single micron-sized particles and allows to obtain Near Edge X-ray Absorption Fine

Structure (NEXAFS) spectra with high spatial resolution. Thus, the chemical evolution of the interior of the particles can be followed under reaction conditions. The experiments show that the overall degradation rate of shikimic acid is depending on the relative humidity in a way that is controlled by the decreasing diffusivity of ozone with decreasing humidity. This decreasing diffusivity is most likely linked to the increasing viscosity of the shikimic acid-water mixture. The degradation rate was also depending on particle size, most congruent with a reacto-diffusion limited kinetic case where the reaction progresses only in a shallow layer within the bulk. No gradient in the shikimic acid concentration was observed within the bulk material at any humidity indicating that the diffusivity of shikimic acid is still high enough to allow its equilibration throughout the particles on the time scale of hours at higher humidity and that the thickness of the oxidized layer under dry conditions, where the particles are solid, is beyond the resolution of STXM.

3.2 Introduction

Atmospheric aerosols are an important focus of environmental research due to their effect on atmosphere, climate and health (Pöschl, 2005). It has been shown that organic matter can account for a significant and sometimes major mass fraction of aerosols, depending on location (Kanakidou et al., 2005; Zhang et al., 2007). Around 20–70 % of organic particulate matter is comprised of water soluble organics, such as carboxylic acids, polyols, polyphenols, sugars and other highly functionalized compounds (Rogge et al., 1993; Saxena and Hildemann, 1996; Decesari et al., 2000). It was recently shown that aqueous solutions and solution droplets of such organics are likely to form glasses or highly viscous amorphous semi-solids such as rubbers, gels and ultra-viscous liquids under atmospherically relevant conditions (Murray, 2008; Zobrist et al., 2008; Mikhailov et al., 2009). Additionally, recent experimental findings both from field and laboratory measurements suggest an amorphous solid state for organic aerosols (Virtanen et al., 2010; Saukko et al., 2012). Amorphous solids and semi-solids are highly viscous. Solid glasses have viscosities $\geq 10^{12}$ Pas (Debenedetti and Stillinger, 2001), while the viscosity of semi-solids is lower ($> 10^{10}$ to $> 10^{4}$ Pas) (Mikhailov et al., 2009) but still high compared to liquid water ($\sim 10^{-3}$ Pas). At high viscosities, diffusion is significantly slower, which is likely to decrease the reaction rate, diminish water uptake, inhibit ice nucleation and influence the formation and growth of SOA (Murray,

2008; Mikhailov et al., 2009; Shiraiwa et al., 2011; Zobrist et al., 2011; Perraud et al., 2012; Shiraiwa and Seinfeld, 2012). Reactions within the bulk of aerosol particles are dependent on diffusion of reactive molecules (oxidant gases) into the bulk. If viscosity is too high, diffusion could become the rate limiting process. This phenomenon is well known for crystalline solids, where reactivity is generally limited to the surface (Moise and Rudich, 2002; Renbaum and Smith, 2009). Therefore, formation of amorphous solids and semi-solids should severely slow down or even inhibit reactions. This change in reactivity has important implications for the lifetime of particles and their constituents and the particles' physical and chemical properties. It is therefore necessary to thoroughly investigate the existence and extent of the influence of the physical state on reactivity. First indications of such a link between physical state and reactivity were shown by Shiraiwa et al. (2011). In their study, the authors used a kinetic model (KM-SUB) (Shiraiwa et al., 2010) to evaluate experimental data from flow tube experiments of ozonolysis of thin protein films and obtain information on the kinetic regimes as a function of viscosity. The temporal behavior of the uptake coefficient was interpreted as driven by diffusion in the condensed phase. Since then, only two additional studies, both of them using aerosol flow tubes and mass spectrometric detection, have been conducted: a study by Kuwata and Martin (2012) proposing a connection between physical state and the formation rate of organonitrates in α-pinene SOA and one by Zhou et al. (2013), showing that the extent of the reaction of benzo[a]pyrene with ozone (O_3) is limited by diffusion through SOA coatings at humidities of 50 % and lower.

When studying the effects of physical state on the reactivity of aerosol particles, direct observation of the bulk reaction would be of an advantage. In Near Edge X-ray Absorption Fine Structure (NEXAFS) spectroscopy, core electrons are excited into unoccupied orbitals, resulting in resonant absorption peaks around the element specific ionization threshold (absorption edge). This resulting fine structure can be used to distinguish different functional groups (Hopkins et al., 2007; Takahama et al., 2007; Pöhlker et al., 2012). Scanning transmission x-ray microscopy (STXM) is a microscopy technique which offers a high spatial resolution of down to less than 20 nm (Raabe et al., 2008) though it is usually more around 30 nm for environmental applications (Bluhm et al., 2006). Combining the spectroscopic technique with microscopy therefore offers the possibility to measure chemical maps at this high spatial resolution (Russell et al., 2002; Maria et al., 2004; Moffet et al., 2010, 2013) that cannot be achieved by optical methods

such as Raman microscopy (Ivleva et al., 2007; Yeung et al., 2009). Since the ionization edge of carbon lies in the soft x-ray regime, carbon NEXAFS measurements are usually performed in vacuum to avoid absorption of the incident beam by air. To facilitate STXM/NEXAFS measurements of single particles under in situ exposure to various gases, we have developed an environmental microreactor (Huthwelker et al., 2010) based on a design by Drake et al. (2004). Our reactor has so far been used to observe water uptake on ammonium sulfate and mixed ammonium sulfate/adipic acid (Zelenay et al., 2011a) and soot particles (Zelenay et al., 2011c) as well as humidity driven chemical separation of complex organic matter such as fulvic and tannic acid (Zelenay et al., 2011b). A reactor of similar design with an in cell humidity probe was recently developed and characterized by Kelly et al. (2013). We have now utilized our microreactor to observe the ozonolysis of single shikimic acid particles in situ and under different relative humidities, to provide new insights into the dependence of reactivity on physical state. While Drake et al. (2004) have already used their cell to monitor oxidation state changes in a silica-supported copper catalyst, this is to our best knowledge the first successful application of STXM/NEXAFS to observe a chemical reaction of an environmentally relevant organic material in situ. The organic compound in question, shikimic acid ((3*R*,4*S*,5*R*)-3,4,5-trihydroxycyclohex-1-ene-1-carboxylic acid, Figure 3.1), was chosen as a proxy for oxygenated organic material and has been shown to be present in biomass burning aerosol (Medeiros and Simoneit, 2008). Shikimic acid undergoes humidity dependent changes in physical state (Chapter 2/Steimer et al., 2015) and both shikimic acid as well as its first generation ozonolysis products are unlikely to be volatile, making it a suitable compound for a STXM investigation of the influence of physical state on reactivity.

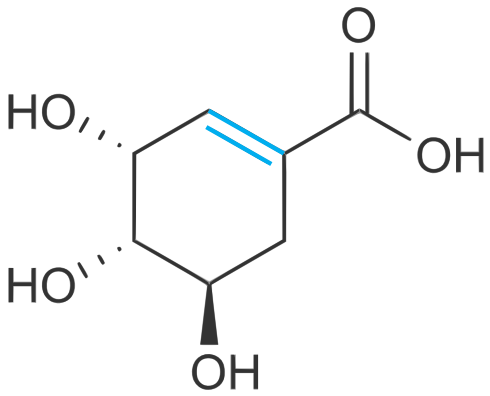

Figure 3.1: Structure of shikimic acid.

3.3 Experimental section

3.3.1 Sample preparation

Shikimic acid ($\geq 99\,\%$) was purchased from Sigma-Aldrich and used without further purification. Aerosol particles were generated by nebulizing a solution containing a few grams per liter of shikimic acid in ultrapure water 18 **M**cm, MilliQ) with a custom-built ultrasonic particle generator. The particles were then dried with a Nafion membrane diffusion drier, charge equilibrated by passing them through a Kr-85 source and size-selected using a differential mobility analyzer (DMA) at a voltage of 1.9 **kV**. The selected particles were counted with a condensation particle counter (CPC) and deposited via impaction on a silicon nitride (Si_3N_4) membrane supported by a Si-window frame, which is attached to the removable front piece of the environmental microreactor.

3.3.2 Environmental microreactor

Usage of an environmental microreactor made it possible to expose the particles to various gases within a temperature and humidity controlled environment during microspectroscopy measurements. A detailed description of the reactor can be found elsewhere (Huthwelker et al., 2010). Briefly, the microreactor consists of two main parts: a removable front piece, holding the window on which the sample is deposited, and the body. The latter includes a gas in- and outlet and is capped with another window. These windows consist of 5 **mm** $\times$ 5 **mm** silicon frames with small openings in the center (0.5 **mm** $\times$ 0.5 **mm** front window, 1 **mm** $\times$ 1 **mm** back window,) supporting 50 **nm** thick Si_3N_4 membranes. They are attached to the cell with wax (crystal bond 509, SPI suppliers). The front piece is mounted onto the main body with screws, resulting in a leak tight chamber of about 300 **µm** $\times$ 5 **mm** $\times$ 5 **mm** inner dimensions which is permeable to x-rays through the windows aligned along the beam axis. The cell was left at room temperature during the present measurements. Temperature was constantly monitored with a thermocouple attached to the reactor body.
The atmosphere within the reactor was adjusted by varying the flow of the different gases used in this study. The two main gases were helium (He) and oxygen (O_2) used at ratios from 4 : 1 to 7 : 1. Part of the oxygen was converted to ozone (O_3)

using an adjustable O_3 generator based on a mercury UV-lamp resulting in ozone partial pressures of 2.5×10^{-6} to 6.5×10^{-6} atm. The O_3 concentration was measured at the exhaust of the reactor with a home-built UV absorption setup, which was calibrated with a commercial ozone analyzer (Model 400E UV Absorption O_3 Analyzer, Teledyne-API). We neglect loss of O_3 to tubing and the micro reactor as we assume passivation to be fast at these high concentrations. Humidity was adjusted by passing a variable fraction of the He flow through a humidifier. Experiments were conducted at four different relative humidities (RH): 12 %, 52 %, 71 % and 82 %. RH was measured using capacitance sensors at the entrance and exit of the microscope chamber. The sensors were operated at room temperature and regularly compared to a dewpoint sensor (DewMaster, EdgeTech). The relative humidity in the microreactor was calculated from the capacitance sensor output by taking into account the microreactor temperature measured by the thermocouple and the small but measurable pressure drop between inlet and outlet. The pressure within the reactor was set to 150 mbar throughout all experiments.

3.3.3 STXM-NEXAFS

All measurements were performed at the PolLux beamline (X07DA) of the Swiss Light Source (SLS) at Paul Scherrer Institute, Switzerland. This beamline provides photons with an energy range of 200–1400 eV at an energy resolution ($E/\Delta E$) of about 3000. The endstation is a Scanning Transmission X-ray Microspectroscope (Raabe et al., 2008) with a spatial resolution of about 40 nm under the conditions of the present experiments. Additional energy calibration of spectra beyond the routine calibration of the beamline was done by comparing the measured lowest energy peak of polystyrene with its literature value (285.18 eV) (Dhez et al., 2003). To convert from transmission to absorption and normalize spectra and images to the incident light intensity, the Lambert–Beer law ($\mathrm{OD} = -\ln(I/I_0) = d\mu$) was used. Here OD is the optical density, μ the linear absorption coefficient, d the thickness of the sample, I the transmitted light intensity through the particle and I_0 the incident light intensity. Two different modes of measurement were employed during the experiments. Carbon spectra were measured in image stack mode, in which a series of images is taken at closely spaced energy steps, yielding spatially resolved spectra (Jacobsen et al., 2000).
The step sizes for the present experiments were 1 eV in the range of 280 to 284 eV, 0.2 eV in the range of 284.1–290 eV and 1.9 eV in the range of 291–320 eV with

a dwell time of 1 ms for each energy. The spatial resolution was either 30 × 30 or 40 × 40 pixels over a rectangular area typically 3 to 5 µm. Spatial as well as energy resolution were kept relatively low to increase time resolution and, in addition with the low dwell time, avoid beam damage. For a less noisy, well resolved line spectrum of shikimic acid see suppl. Figure 3.8. To obtain chemical maps, stacks of transmission images with higher spatial resolution (65 × 65 or 70 × 70 pixels) were measured at only few selected energies: 279.5 eV, 281.5 eV (pre edge), 284.1 eV, 284.2 eV, 284.3 eV, 284.4 eV (1s-π^* transition peak) and 311.0 eV, 319.5 eV (post edge), all with a dwell time of 3 ms. These images were then converted to OD images. The spatial distribution of the double bond of shikimic acid within a particle was assessed by calculating the ratio of the pre-edge subtracted image at peak maximum of the 1s-π^* transition peak to that of the pre-edge subtracted total carbon yield images. Since dividing the small values of the backgrounds of the OD images leads to large noise in the chemical maps, the background was masked to enhance visibility of the particles. The border between background and particle was drawn manually, judging by eye where the region of neighboring extreme values begins. Integration of these images yields radial profiles, which provide information about the radial distribution of the double bond at a higher signal-to-noise ratio. Additionally, low resolution spectra were extracted from these image series to provide additional data for the analysis of the humidity and size dependence of the shikimic acid degradation. All spectra were normalized by the averaged post-edge absorption at 310–320 eV. Particles were always only measured once to avoid any effect of beam damage on the retrieval of degradation rates. Due to carbon contamination along the beamline, optical elements and windows, and the influence of small amounts of higher order light, all measured spectra shown are slightly distorted around the carbon K-edge (near 290 eV), where only little light reaches the sample and greater relative proportion of higher-order light leads to an apparently lower absorption. This should however not affect the regions of the spectra used for data analysis (see Supplementary material). All data analysis was done using aXis2000 (Hitchcock, 1998).

3.4 Results and discussion

3.4.1 Evolution of carbon NEXAFS spectra during ozonolysis

Shikimic acid is oxidized upon exposure to O_3 Figure 3.2. Spectrum a shows the averaged NEXAFS carbon K-edge spectrum of dry, fresh shikimic acid particles. The main identifiable feature is the 1s-π^* transition at 284.4 eV. Upon oxidation at 82 % RH (spectrum b and c), this peak decreases since the shikimic acid double bond is broken in a Criegee reaction (Criegee, 1975). This demonstrates our ability to monitor the degradation by STXM/NEXAFS in situ. Apart from the decrease at 284.4 eV, two additional changing features can be observed: the appearance of a small peak at 286.4 eV and an increase as well as a small shift of the carboxyl peak at 288.2 eV. The appearance respectively increase of these two peaks is indicative of an increase in oxidized bonds. Additional oxygen functionality is consistent with secondary chemistry during condensed phase ozonolysis of alkenes (Zahardis and Petrucci, 2007). We refrain from further interpreting these peaks in terms of different conceivable products. Since it is easiest to identify and least likely to be affected by beamline contamination (see Supplementary material for discussion and an example of a less affected spectrum (suppl. Figure 3.8)), the decrease of the 1s-π^* transition peak was chosen to quantitatively follow the progression of the reaction. Note that the spectra are normalized to the averaged absorption between 310 and 320 eV, i.e., total carbon, so that the peak height of the 1s-π^* transition is proportional to the shikimic acid concentration in an individual particle and differences in particle size are accounted for.

3.4.2 Humidity dependence

The evolution of the 1s-π^* transition peak with exposure to O_3 was monitored at four different relative humidities: 12 %, 52 %, 71 % and 82 %. This was done by normalizing the peak height per particle after a certain time of oxidation to the average initial height measured in particles prior to oxidation at this humidity (Figure 3.3a). Peak height per particle was calculated as an average over the projected particle area. The ratio of the two peak heights before and after oxidation equals the relative loss of shikimic acid $[Y]_b/[Y]_{b,0}$ where $[Y]_b$ is the current bulk concentration of shikimic acid of the measured particle and $[Y]_{b,0}$ the associated

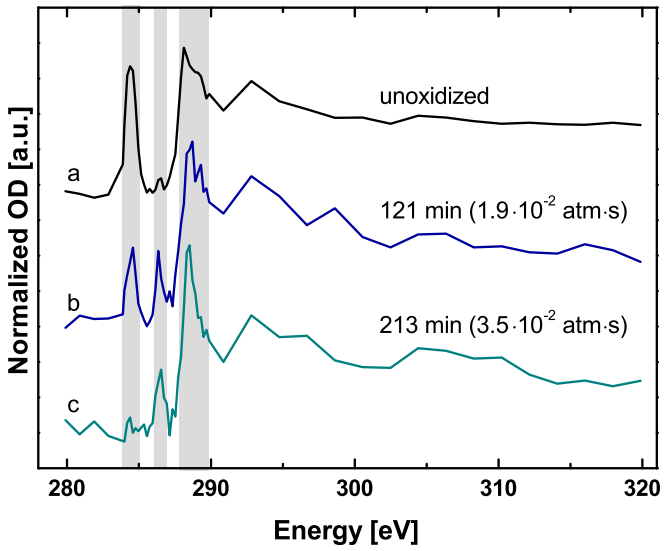

Figure 3.2: Averaged spectra of single particles before and after oxidation at a relative humidity of 82 %. The gray areas denote regions in which spectral changes can be observed. The main feature of the oxidation is the decrease of the 1s-π^* peak at 284.4 eV.

average initial bulk concentration. In other words, for one sample, after taking spectra on a number of particles (2–9) to determine the average signal proportional to the initial concentration $[Y]_{b,0}$, exposure starts at the same time for all particles, but the signal proportional to $[Y]_b$ is quantified for different other individual particles at different times, i.e. $[Y]_b$ is only measured once for each individual particle. Therefore, each data point in Fig. 3 represents the ratio $[Y]_b/[Y]_{b,0}$ for a different particle. Beam damage prevents observing the degradation for the same particle over longer times.

Figure 3.3 clearly demonstrates that the degradation rate of shikimic acid is depending on humidity. In the following, the degradation rate laws are discussed for different conceivable kinetic regimes. Assuming a pseudo first order reaction, the depletion rate is linearly dependent on $[Y]_b$ (Eq. 3.1)

$$\frac{d[Y]_b}{dt} = -k^{II}[O_3]_b[Y]_b = -k^{II}H_{O_3}p_{O_3}[Y]_b = -k^{I}_{Y}[Y]_b, \tag{3.1}$$

where $[O_3]_b$ equals the O_3 concentration in the aerosol bulk in $\mathrm{mol\,L^{-1}}$, k^{II} the second order rate constant in $\mathrm{L\,mol^{-1}\,s^{-1}}$, H_{O_3} the Henry constant in $\mathrm{mol\,L^{-1}\,atm^{-1}}$,

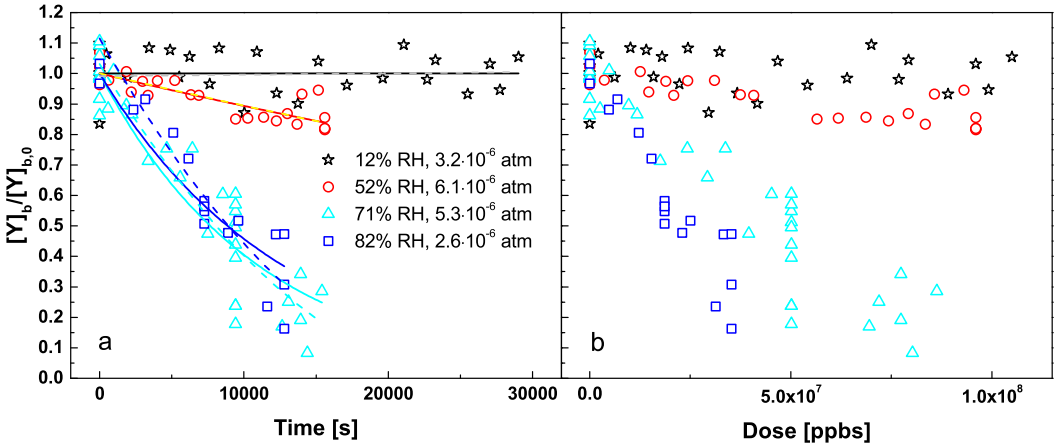

Figure 3.3: **(a)** Depletion of shikimic acid as a function of exposure time via the decrease in the normalized OD at 284.4 eV (relative loss). The depletion was measured at four different relative humidities. The lines show the respective fits for that humidity assuming pseudo first order decay (black, red, blue and cyan, solid line) and reacto-diffusive limitation (grey, yellow, blue and cyan, dashed line). **(b)** Depletion of shikimic acid as a function of O_3 dose via the decrease in the normalized OD at 284.4 eV at four different relative humidities.

p_{O_3} the absolute pressure of O_3 in the system in atm and k_Y^I the pseudo first order rate constant with respect to shikimic acid depletion in s^{-1}. Solving the differential equation shows that the relative loss as a function of time can be fitted with an exponential decay (Eq. 3.2).

$$\frac{[Y]_b}{[Y]_{b,0}} = e^{-k_Y^I t} \tag{3.2}$$

Equation 3.1 is valid, if the reactants (O_3 and Y) remain well mixed throughout the particle volume and depletion is only limited by the rate of the reaction. This is referred to as the bulk reaction limited case (Berkemeier et al., 2013) or often also referred to as volume limited uptake. In contrast to that, if the reaction is fast compared to diffusion so that O_3 does not reach far into the interior of the particle, the loss rate of $[Y]_b$ exhibits a square root dependence of $[Y]_b$ which is traditionally referred to as reacto-diffusive limitation (Eq. 3.3),

$$\frac{d[Y]_b}{dt} = -H_{O_3} RT \sqrt{D_{O_3} k_b^{II}} \frac{S_p}{V_p} [O_3]_g \sqrt{[Y]_b} = -k^D \sqrt{[Y]_b}, \tag{3.3}$$

where R is the gas constant in $\mathrm{L\,atm\,K^{-1}\,mol^{-1}}$, D_{O_3} the diffusion coefficient of O_3 in the bulk in $\mathrm{cm^2\,s^{-1}}$, $[O_3]_g$ the gas phase ozone concentration in $\mathrm{mol\,L^{-1}}$, S_p the particle surface in $\mathrm{cm^2}$ and V_p the particle volume in $\mathrm{cm^3}$. The relative loss can then be described by a second order polynomial as a function of time (Eq. 3.4),

$$\frac{[Y]_b}{[Y]_{b,0}} = \left(\frac{-k^D t + 2\sqrt{[Y]_{b,0}}}{2\sqrt{[Y]_{b,0}}} \right)^2, \tag{3.4}$$

which is a more general form of the equation described by Worsnop et al. (2002) for reacto-diffusive limitation in spherical particles. In this case $[Y]_{b,0}$ is needed to fit the data; these concentrations at different humidities were derived from measurements of the growth of dry shikimic acid particles as a function of humidity in an electrodynamic balance (EDB) (Chapter 2/Steimer et al., 2015). As one can see from comparison of the fits for the different kinetic regimes in Figure 3.3a, the two regimes can not be distinguished with the available data. By fitting a linearized version of the respective integrated rate law to the measured data (Figure 3.4), one can determine k^I_Y $[\mathrm{s^{-1}}]$ (Eq. 3.5)

$$\ln\left(\frac{[Y]_b}{[Y]_{b,0}}\right) = -k^I_Y t \tag{3.5}$$

and k^D $[\mathrm{mol^{0.5}\,L^{-0.5}\,s^{-1}}$ (Eq. 3.6)

$$2\sqrt{[Y]_b} - 2\sqrt{[Y]_{b,0}} = -k^D t \tag{3.6}$$

from the slope of the fits. The resulting rate constants are listed in Table 3.1. Using the relation of pseudo first order and second order rate constant (Eq. 3.1) and the description of the uptake coefficient γ for a bulk reaction limited system (Eq. 3.7),

$$\gamma_{O_3} = \frac{4k^{II}H_{O_3}RT[Y]_b}{\bar{c}}\frac{V_p}{S_p} \tag{3.7}$$

one can use the obtained data to calculate the uptake coefficient γ (Eq. 3.8), which describes the net uptake to the particle normalized by the collision rate.

$$\gamma_{O_3} = \frac{4k^I_Y RT[Y]_b}{\bar{c}p_{O_3}}\frac{V_p}{S_p} \tag{3.8}$$

We thereby assume that the rate of disappearance of the double bond is equal to the rate of ozone uptake, i.e., no additional ozone loss occurs. The values obtained are also inherently linked to the assumption of the bulk reaction limited regime. The resulting values for γ assuming a 1 µm hemispherical particle can be found in Table 3.1. The uptake varies by more than two orders of magnitude, from

RH [%]	p_{O_3} [atm]	$[Y]_0$ [mol L^{-1}]	k^I [s^{-1}]	k^D [mol$^{0.5}$ L$^{-0.5}$ s^{-1}]	γ_{O_3}
12	3.2×10^{-6}	8.4	4.9×10^{-7} ($\pm1.3\times10^{-6}$)	1.5×10^{-6} ($\pm3.8\times10^{-6}$)	5.8×10^{-8} ($\pm1.6\times10^{-7}$)
52	6.1×10^{-6}	7.3	1.1×10^{-5} ($\pm1.2\times10^{-6}$)	2.8×10^{-5} ($\pm3.1\times10^{-6}$)	5.9×10^{-7} ($\pm1.1\times10^{-7}$)
71	5.3×10^{-6}	6.3	1.1×10^{-4} ($\pm1.1\times10^{-5}$)	2.0×10^{-4} ($\pm1.5\times10^{-5}$)	5.9×10^{-6} ($\pm1.1\times10^{-6}$)
82	2.6×10^{-6}	5.2	1.0×10^{-4} ($\pm1.5\times10^{-5}$)	1.8×10^{-4} ($\pm2.1\times10^{-5}$)	9.0×10^{-6} ($\pm2.2\times10^{-6}$)

Table 3.1: First order rate constants for the reaction limited case (k^I) and rate constants under reacto-diffusive limitation (k^D) with standard error, determined from the linear fits and uptake coefficient for O_3 on shikimic acid calculated assuming reaction limitation.

5.8×10^{-8} at 12 % RH to 9.0×10^{-6} at 82 % RH. Using the pseudo-first order rate constant determined at 82 % RH for the bulk reaction limited case and the Henry's law constant for O_3 solubility in water at 298 K, 1.3×10^{-2} mol L^{-1} atm^{-1} (Utter et al., 1992), the second order rate constant of the reaction was calculated. With $k^{II} = 3\times10^3$ L mol^{-1} s^{-1}, the reactivity of shikimic acid with O_3 is comparable to similarly functionalized compounds in aqueous solution, such as fumaric acid, where the reaction is about a factor of two faster (6×10^3 L mol^{-1} s^{-1}) (Hoigné and Bader, 1983). The rate constant for shikimic acid is about three orders of magnitude lower than that for oleic acid (1×10^6 L mol^{-1} s^{-1}, Razumovskii and Zaikov, 1980), a compound frequently used in aerosol chemistry to address condensed phase kinetics (Zahardis and Petrucci, 2007).

While a similar calculation could, in principle, also be done to extract k^{II} from k^D, the lack of data on the humidity dependent diffusion coefficient of O_3, D_{O_3}, prevents quantitative evaluation. When plotting against the total O_3 dose instead of time to account for differences in O_3 gas phase concentration, it can be clearly observed that the depletion rate increases with increasing humidity (Figure 3.3b). For both bulk reaction limited and reacto-diffusion limited reaction (Eq. 3.1 and Eq. 3.3), one would usually expect a decrease in reactivity with increasing humidity since the bulk concentration of shikimic acid decreases with increasing water activity. One other parameter influencing the ozone uptake in both cases is the Henry constant. However, ozone solubility tends to be higher for liquid organics compared to water (Biń, 2006), so that one would generally expect a reactivity decrease with increasing humidity due to solubility decreasing

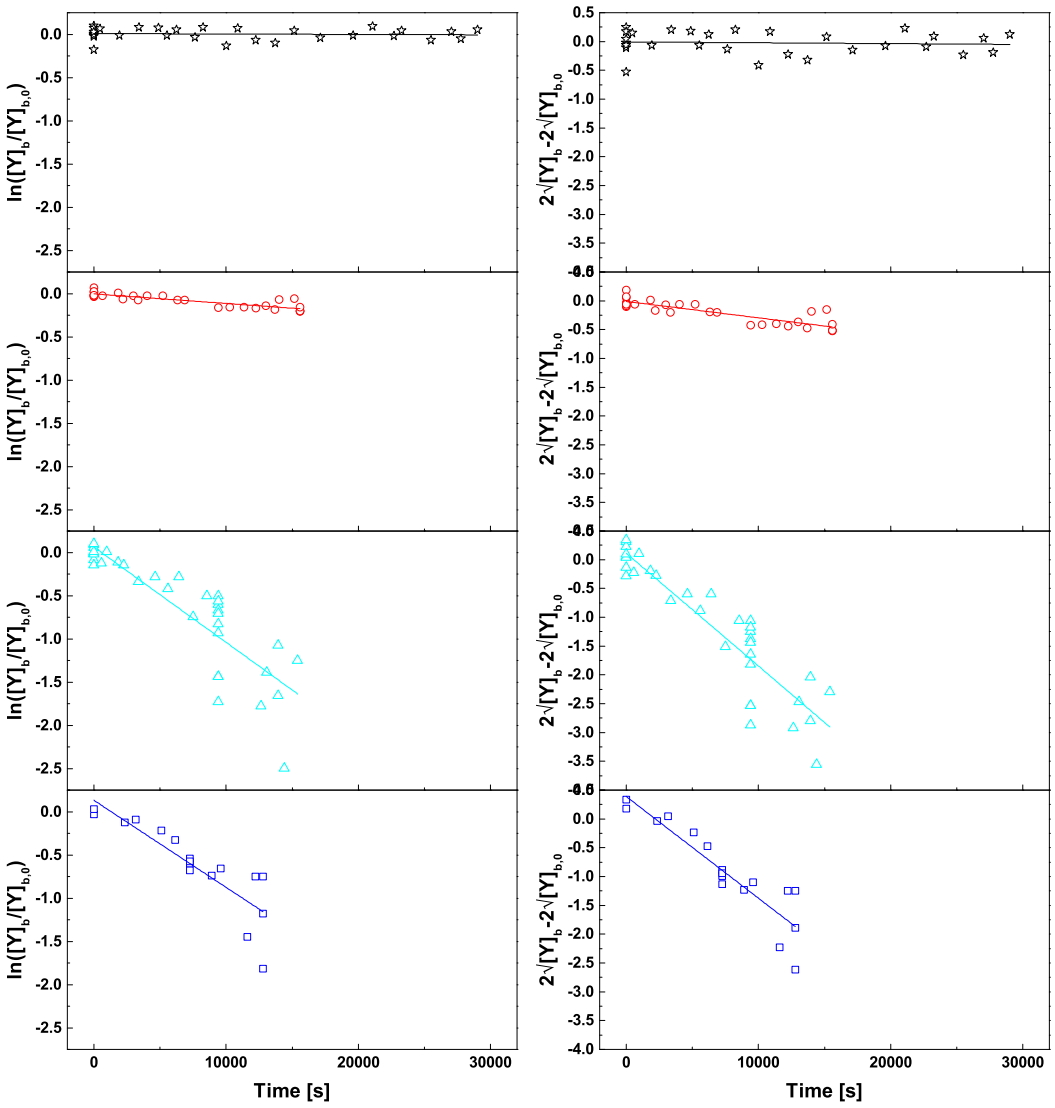

Figure 3.4: Linearized plots for pseudo first order volume limited (left) and reacto-diffusion limited reaction (right): linearized plots for the reacto-diffusive case: 12 % RH (black stars, 3.2×10^{-6} atm), 52 % RH (red circles, 6.1×10^{-6} atm), 71 % RH (light blue triangles, 5.3×10^{-6} atm) and 83 % RH (blue squares, 2.6×10^{-6} atm). The slope of the linear fit equals the corresponding rate constant.

towards that of pure water. As amorphous solids have only a small difference in free energy compared to the liquid, thermodynamic properties such as solubility should not be strongly affected and we expect the same trend for solubility of O_3 in shikimic acid. Therefore, the trend of decreasing degradation rate with decreasing humidity goes in the opposite direction to that expected based on shikimic acid concentration and solubility for either of the kinetic regimes.
However, the reacto-diffusive uptake is also influenced by the diffusion coefficient, D_{O_3} (Eq. 3.3). The degradation rate may become increasingly limited by diffusion towards lower humidity, because of the low diffusivity expected for the semi-solid and solid physical states that shikimic acid is likely to attain. If water acts as a plasticizer, the increasing humidity would lead to an increase in diffusivity, enabling a faster degradation rate. The fact that the reactivity increases with increasing water content in this experiment can therefore be seen as an indication for a reacto-diffusion limited regime showing a connection between physical state and reactivity. For simplicity, we assume that H_{O_3} remains the same for all humidities and corresponds to the O_3 solubility in water and that k^{II} derived for the volume limited case at 82 % RH remains also the same for all conditions. If we thus assume that the reactivity change with humidity is solely due to changing diffusivity and shikimic acid concentration, we can estimate the range over which the diffusivity of ozone would need to change from humid to dry conditions from the values obtained for k^D. D_{O_3} would have to decrease from 7.6×10^{-7} $cm^2 s^{-1}$ at 71 % RH to 1.2×10^{-10} $cm^2 s^{-1}$ at 12 % RH. The latter value is typical for small guest molecules in a glassy matrix (Koop et al., 2011). These estimates thus indicate that the changing degradation rate with humidity can be consistently interpreted in terms of the changing diffusivity likely caused by corresponding changes in viscosity.

3.4.3 Size dependence

By plotting the ratio of normalized OD at 284.4 eV to initial peak height against OD of total carbon, one can observe a dependence of the reaction progression on particle thickness (Figure 3.5). OD of total carbon (indicating particle thickness) was chosen here as a proxy of size instead of particle radius since low contrast for some of the particles prevented reliable determination of cross sectional area and shape from the absorption profile. In addition, under higher humidity conditions, the particles were not spherical anymore, but tended to spread out beyond half spheres (see supporting information). Under those conditions, the size as determined by the projected area would not be the appropriate measure of the radius of the particles. The ozonolysis progresses faster for thinner particles. The change in ratio is proportional to a change in concentration of shikimic acid, which should be independent of particle size in case of a volume limited reaction (Eq. 3.1). A diffusion limited reaction on the other hand depends on the ratio of surface to volume (Eq. 3.3), which is larger for small particles. It can easily be seen why when considering the reacto-diffusive length l (Eq. 3.9), which describes how far a gaseous molecule can diffuse before it reacts:

$$l = \sqrt{\frac{D_{O_3}}{k^{I}_{O_3}}} \tag{3.9}$$

Smaller particles have a higher surface to volume ratio so that the thin layer in which the reaction takes place takes up a proportionally larger part of the total particle volume. Using the k^{II} value estimated in 3.2, one can calculate $k^{I}_{O_3}$. Under the assumption that we have a liquid of low viscosity at 82 % RH ($D_{O_3} = 1 \times 10^{-5}$ cm^2 s^{-1}), the reacto-diffusive length is 253 nm. Taking the estimates of the diffusion coefficients obtained above, the values of l range from 70 to 0.9 nm from 71 % RH to 12 % RH. Thus, this would provide an a posteriori justification for the assumption made in Section 3.4.2 that from 71 % RH to 12 % RH the reacto-diffusion limited is the more likely scenario (l is much smaller than the particle dimension/thickness), while at 82 % extracting the rate constant under the bulk reaction limited regime would be warranted, especially since the particles at this humidity spread to a shape thinner than hemispherical. Of course formation of an oxidized layer could further influence the uptake due to a change in physical parameters affecting the phase transfer, but a decrease in viscosity remains vital in formation of such a layer. It is also a possibility that reaction products could

in general affect viscosity of the particle. Different product yields at different humidities could therefore lead to unforeseeable effects on diffusivity, a possibility neglected in our data evaluation. Further uncertainties arise from the fact that the concept of reacto-diffusive length is strictly speaking only valid for cases in which the bulk reactant is well mixed. Due to the not so well defined shape of the particles at higher humidity, we also refrain from application of a correction to Eq. 3.3 to account for non-planar surfaces.

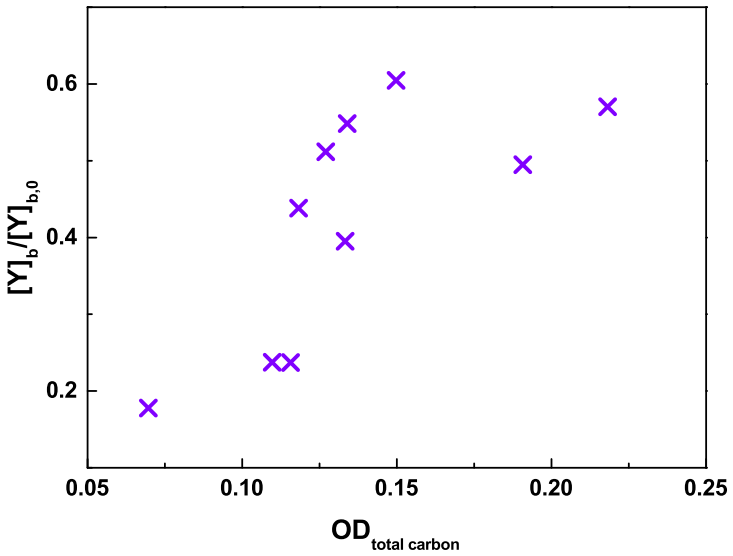

Figure 3.5: Size dependence of the oxidation rate: the amount of material already oxidized differs for particles of different thickness, all oxidized at 71 % RH with an ozone dose of 5.0×10^{-2} atm s.

3.4.4 Chemical maps

For a highly viscous particle with low diffusion coefficients, a gradient of the condensed phase reactant might build up in the bulk material, as suggested by Shiraiwa et al. (2011) for the case of ozonolysis of a protein. The kinetic analysis at different humidities and the size dependence have also led us to suggest that the reaction occurs within a thin layer close to the surface (for the medium and lower humidities) and that the differences between the humidities would be attributed to a change in diffusion coefficient by four orders of magnitude. It would thus be con-

ceivable to assume that the diffusion coefficient of shikimic acid could become low enough so that the diminished exchange within the bulk phase leads to a gradient within the particles. Therefore, we extracted chemical maps showing the distribution of the double bond throughout the particles at various steps of the oxidation process at 13 % RH, 52 % RH and 71 % RH. Figure 3.6a–c show the progress of the oxidation for different particles at 71 % RH. These figures again clearly show that the concentration of the double bond decreases with an increasing O_3 dose (Section 3.4.1). In Figure 3.6c, one can clearly see that the smaller particle of the two is oxidized to a larger degree than the larger one (Section 3.4.3). This decrease occurs homogeneously throughout the particle, as would be expected for particles at high humidity, where the diffusivity of shikimic acid is likely large enough to allow sufficient exchange throughout the particle, in spite of the fact that the actual reaction occurs within the reacto-diffusive depth of O_3. The radial profiles in Figure 3.6d support this conclusion. Also at 52 % RH no gradient was apparent in spite of measurable overall degradation. Plots e to g in Figure 3.6 on the other hand depict the progress of oxidation at 12 % RH. No oxidation is observable, as also seen from the radial profiles in Figure 3.6h. Progression of the reaction from the surface towards the interior was obviously too slow to be observed within the duration of the experiment, and the layer of oxidized material too thin to become apparent within the resolution of the method. As estimated above, the reacto-diffusive length of O_3 would be 0.9 nm at this humidity. Accordingly, the integrated analysis of many more particles shown in Figure 3.3 likewise does not show an apparent degradation under these dry conditions. To demonstrate the capability of the method to actually identify marked chemical gradients at the scale of more than about 100 nm, we show an image of a particle with an accidental contamination as an inclusion in the supplementary material (suppl. Figure 3.10).

The lack of a visible gradient combined with the existence of size dependence points to a classic reacto-diffusive case where a gradient only exists in O_3, while the bulk material is well mixed for humidities at and above 52 %. Under conditions, where the diffusion coefficient of ozone drops to 1×10^{-10} cm^2 s^{-1}, it is likely that the self diffusion coefficients can be very low, easily below 10^{-16} cm^2 s^{-1} in magnitude (Koop et al., 2011). Thus, if the location of oxidation is confined to a layer of thickness l of 0.9 nm estimated above, it would take 280 h for the oxidation front to migrate over more than 100 nm for $D = 10^{-16}$ cm^2 s^{-1} so that it could become apparent in our STXM images, which was beyond the time scale of our experiment. To resolve a gradient, we propose using a different model sys-

tem to which one of the two following conditions apply. The easiest case would be a system where diffusion of the bulk reactant is already so low that full exchange of bulk molecules does not happen on timescales of the experiments (such as in our low humidity case), but with a diffusion of the small gas phase reactant which is still sufficiently high to guarantee reaction over an observable distance. Proteins, in which small molecules can move via percolation, might be one such system. Shiraiwa et al. (2012) have suggested such gradients to occur during nitration of proteins. Another conceivable situation would be that the ratio of the diffusion coefficient to the first order loss rate constant would be of the same order of magnitude for the two reacting species. Since for the conditions of a STXM experiment the condensed phase reactant needs to be at high concentrations to provide sufficient dynamic range, only very soluble oxidants would be feasible for such experiments.

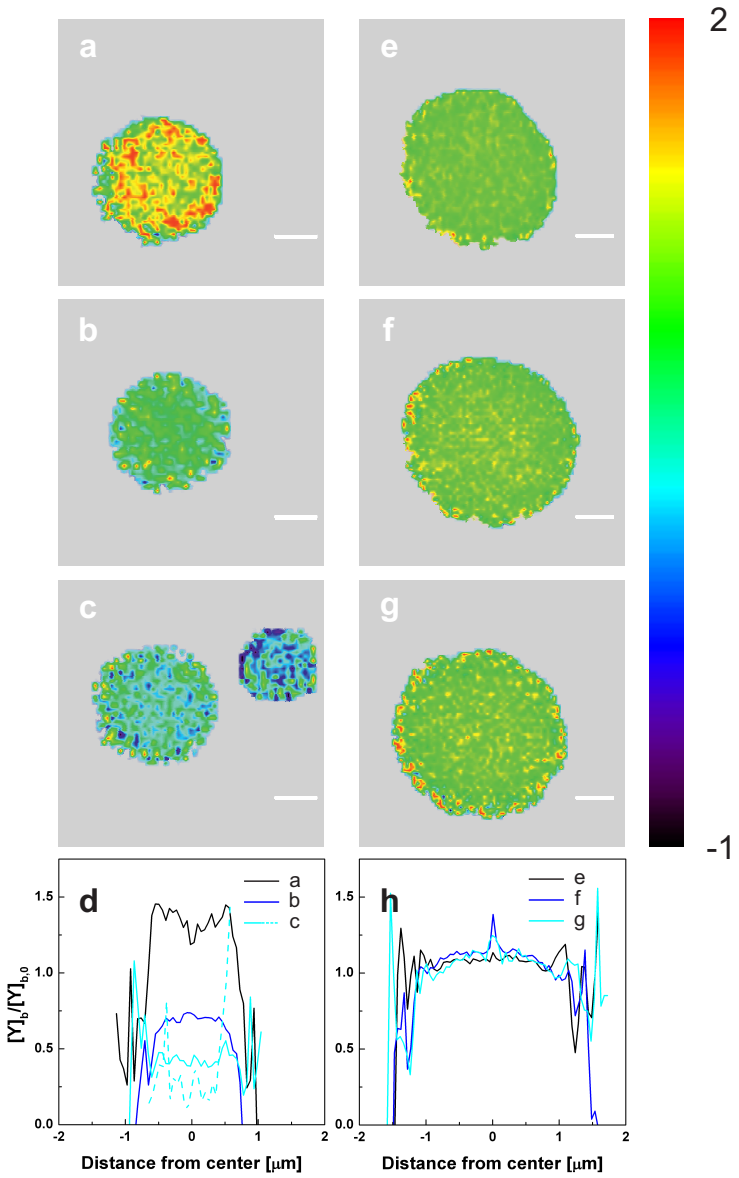

Figure 3.6: Depletion of shikimic acid via the decrease of OD at the maximum of the 1s-π^* transition peak around 284.4 eV normalized to total carbon. **(a–c)** show the progress of the reaction for four different particles at 71 % RH at O_3 doses of 0 atms **(a)**, 5.0×10^{-2} atms **(b)** and 7.7×10^{-2} atms **(c)**. **(d)** depicts the respective radial profiles of the particles: **(a)** (black line), **(b)** (dark blue line) and **(c)** (light blue lines, solid (larger particle) and dashed (smaller particle)). **(e–g)** show the progress of the reaction for three different particles at 13 % RH with O_3 doses of 0 atms **(e)**, 1.4×10^{-2} atms **(f)** and 7.9×10^{-2} atms **(g)**. **(h)** depicts the radial profiles of the imaged particles: **(e)** (black line), **(f)** (dark blue line) and **(g)** (light blue line). The scale bar denotes 500 nm. The the appearance of clusters of red pixels at the edge of some of the particles arises from alignment issues combined with the relatively low contrast of the carbon K-edge measurements. The images show that no observable concentration gradient has formed at either humidity.

3.5 Conclusions and implications

In this study, we demonstrated that in situ STXM/NEXAFS is a useful tool to investigate the oxidation kinetics of liquid and semi-solid particles. We have successfully shown that the degradation kinetics of shikimic acid depends on humidity and is therefore likely influenced by their physical state. While the depletion curves alone do not provide enough information to distinguish between a bulk reaction limited case and reacto-diffusive limitation, additional information from the size dependence of the reaction points to reacto-diffusive limitation. No gradient of shikimic acid was observed in any of our measurements. Assuming reacto-diffusive limitation, this means that it is either beyond the spatial or temporal resolution of our method or that the limitation is only enforced by a gradient in O_3.

This study shows that in the transition from aqueous liquid to semi-solid or glassy states at lower humidity, the oxidation of unsaturated organics is largely suppressed and confined to a thin surface layer. This increases the life time of reactive organic compounds by many orders of magnitude. Assuming the reaction is pseudo-first order with respect to O_3 we can use the apparent first order rate constants listed in Table 1 to estimate atmospheric lifetimes. Using the Henry's law constant for O_3 solubility in water at 298 kelvin (Utter et al., 1992), we calculate a shikimic acid lifetime of 7.5 days at 82 % RH, while the lifetime of particles at 12 % RH would be over 5 years at 40 ppb atmospheric O_3. Such large variations in atmospheric lifetime could for example influence source apportionments if the fate of a marker compound used for the latter is affected. In this case, one might need to take into account the temperature and humidity history of the air mass to make a valid assessment. In other terms, the increased viscosity in semi-solid or glassy particle extends the lifetime of toxic compounds.

It should be noted that according to our observations kinetic limitations become apparent already at 71 % RH. On the other hand, the particles seem well mixed down to 52 % RH and self diffusion of shikimic acid only becomes limiting at very low humidities where the particles become glassy. One should therefore be careful to imply morphological implications such as a core-shell structure from the mere presence of reacto-diffusive limitation.

Acknowledgements

This work is supported by the EU FP7 project PEGASOS and by the Swiss National Science Foundation (grant no 130175). E.C. was supported by a Swiss National Science Foundation International Short Visit grant (IZK0Z2_142687). The PolLux end station was financed by the German Minister für Bildung und Forschung (BMBF) through contracts 05KS4WE1/6 and 05KSWE. B. Watts, J. Raabe and B. Sarafimov were crucial in supporting the operation of our experimental infrastructure at the PolLux microscope. We thank M. Birrer for technical support and appreciate the helpful discussions with A. Huisman, U. Krieger, C. Marcolli and T. Peter.

Bibliography

Berkemeier, T., Huisman, A. J., Ammann, M., Shiraiwa, M., Koop, T., and Pöschl, U.: Kinetic regimes and limiting cases of gas uptake and heterogeneous reactions in atmospheric aerosols and clouds: a general classification scheme, *Atmos. Chem. Phys.*, **13**, 6663–6686, 2013.

Biń, A. K.: Ozone solubility in liquids, *Ozone-Sci. Eng.*, **28**, 67–75, 2006.

Bluhm, H, Andersson, K., Araki, T., Benzerara, K., Brown, G. E., Dynes, J. J., Ghosal, S., Gilles, M. K., Hansen, H.-Ch., Hemminger, J. C., Hitchcock, A. P., Ketteler, G., Kilcoyne, A. L. D., Kneedler, E., Lawrence, J. R., Leppard, G. G., Majzlam, J., Mun, B. S., Myneni, S. C. B., Nilsson, A., Ogasawara, H., Ogletree, D. F., Pecher, K., Salmeron, M., Shuh, D. K., Tonner, B., Tyliszczak, T., Warwick, T., and Yoon, T. H.: Soft X-ray microscopy and spectroscopy at the molecular environmental science beamline at the Advanced Light Source, *J. Electron Spectrosc.*, **150**, 86–104, 2006

Criegee, R.: Mechanism of ozonolysis, *Angew. Chem. Int. Edit.*, **14**, 745–752, 1975.

Debenedetti, P. G. and Stillinger, F. H.: Supercooled liquids and the glass transition, *Nature*, **410**, 259–267, 2001.

Decesari, S., Facchini, M. C., Fuzzi, S., and Tagliavini, E.: Characterization of water-soluble organic compounds in atmospheric aerosol: a new approach, *J. Geophys. Res.-Atmos.*, **105**, 1481–1489, 2000.

Dhez, O., Ade, H., and Urquhart, S. G.: Calibrated NEXAFS spectra of some common polymers, *J. Electron Spectrosc.*, **128**, 85–96, 2003.

Drake, I. J., Liu, T. C. N., Gilles, M., Tyliszczak, T., Kilcoyne, A. L. D., Shuh, D. K., Mathies, R. A., and Bell, A. T.: An in situ cell for characterization of solids by soft x-ray absorption, *Rev. Sci. Instrum.*, **75**, 3242–3247, 2004.

Hitchcock, A. P.: aXis2000, available at: http://unicorn.mcmaster.ca/aXis2000.html (last access: 11 March 2014), 1998.

Hoigné, J. and Bader, H.: Rate constants of reactions of ozone with organic and inorganic-compounds in water, 1. Non-dissociating organic-compounds, *Water Res.*, **17**, 173–183, 1983.

Hopkins, R. J., Tivanski, A. V., Marten, B. D., and Gilles, M. K.: Chemical bonding and structure of black carbon reference materials and individual carbonaceous atmospheric aerosols, *J. Aerosol Sci.*, **38**, 573–591, 2007.

Huthwelker, T., Zelenay, V., Birrer, M., Krepelova, A., Raabe, J., Tzvetkov, G., Vernooij, M. G. C., and Ammann, M.: An in situ cell to study phase transitions in individual aerosol particles on a substrate using Scanning Transmission x-ray Microspectroscopy, *Rev. Sci. Instrum.*, **81**, 113706, 2010.

Ivleva, N. P., McKeon, U., Niessner, R., and Pöschl, U.: Raman microspectroscopic analysis of size-resolved atmospheric aerosol particle samples collected with an ELPI: soot, humic-like substances, and inorganic compounds, *Aerosol Sci. Tech.*, **41**, 655–671, 2007.

Jacobsen, C., Wirick, S., Flynn, G., and Zimba, C.: Soft x-ray spectroscopy from image sequences with sub-100 nm spatial resolution, *J. Microsc.-Oxford*, **197**, 173–184, 2000.

Kanakidou, M., Seinfeld, J. H., Pandis, S. N., Barnes, I., Dentener, F. J., Facchini, M. C., Van Dingenen, R., Ervens, B., Nenes, A., Nielsen, C. J., Swietlicki, E., Putaud, J. P., Balkanski, Y., Fuzzi, S., Horth, J., Moortgat, G. K., Winterhalter, R., Myhre, C. E. L., Tsigaridis, K., Vignati, E., Stephanou, E. G., and Wilson, J.: Organic aerosol and global climate modelling: a review, *Atmos. Chem. Phys.*, **5**, 1053–1123, 2005.

Kelly, S. T., Nigge, P., Prakash, S., Laskin, A., Wang, B., Tyliszczak, T., Leone, S. R., and Gilles, M. K.: An environmental sample chamber for reliable scanning transmission x-ray microscopy measurements under water vapor, *Rev. Sci. Instrum.*, **84**, 73708–73709, 2013.

Koop, T., Bookhold, J., Shiraiwa, M., and Pöschl, U.: Glass transition and phase state of organic compounds: dependency on molecular properties and implications for secondary organic aerosols in the atmosphere, *Phys. Chem. Chem. Phys.*, **13**, 19238–19255, 2011.

Kuwata, M. and Martin, S. T.: Phase of atmospheric secondary organic material affects its reactivity, *P. Natl. Acad. Sci. USA*, **109**, 17354–17359, 2012.

Maria, S. F., Russell, L. M., Gilles, M. K., and Myneni, S. C. B.: Organic aerosol growth mechanisms and their climate-forcing implications, *Science*, **306**, 1921–1924, 2004.

Medeiros, P. M. and Simoneit, B. R. T.: Source profiles of organic compounds emitted upon combustion of green vegetation from temperate climate forests, *Environ. Sci. Technol.*, **42**, 8310–8316, 2008.

Mikhailov, E., Vlasenko, S., Martin, S. T., Koop, T., and Pöschl, U.: Amorphous and crystalline aerosol particles interacting with water vapor: conceptual framework and experimental evidence for restructuring, phase transitions and kinetic limitations, *Atmos. Chem. Phys.*, **9**, 9491–9522, 2009.

Moffet, R. C., Henn, T., Laskin, A., and Gilles, M. K.: Automated chemical analysis of internally mixed aerosol particles using x-ray spectromicroscopy at the carbon k-edge, *Anal. Chem.*, **82**, 7906–7914, 2010.

Moffet, R. C., Rödel, T. C., Kelly, S. T., Yu, X. Y., Carroll, G. T., Fast, J., Zaveri, R. A., Laskin, A., and Gilles, M. K.: Spectro-microscopic measurements of carbonaceous aerosol aging in Central California, *Atmos. Chem. Phys.*, **13**, 10445–10459, 2013.

Moise, T. and Rudich, Y.: Reactive Uptake of Ozone by Aerosol-Associated Unsaturated Fatty Acids: Kinetics, Mechanism, and Products, *J. Phys. Chem.*, **106**, 6469–6476, 2002.

Murray, B. J.: Inhibition of ice crystallisation in highly viscous aqueous organic acid droplets, *Atmos. Chem. Phys.*, **8**, 5423–5433, 2008.

Perraud, V., Bruns, E. A., Ezell, M. J., Johnson, S. N., Yu, Y., Alexander, M. L., Zelenyuk, A., Imre, D., Chang, W. L., Dabdub, D., Pankow, J. F., and Finlayson-Pitts, B. J.: Nonequilibrium atmospheric secondary organic aerosol formation and growth, *P. Natl. Acad. Sci. USA*, **109**, 2836–2841, 2012.

Pöhlker, C., Wiedemann, K. T., Sinha, B., Shiraiwa, M., Gunthe, S. S., Smith, M., Su, H., Artaxo, P., Chen, Q., Cheng, Y. F., Elbert, W., Gilles, M. K., Kilcoyne, A. L. D., Moffet, R. C., Weigand, M., Martin, S. T., Pöschl, U., and Andreae, M. O.: Biogenic potassium salt particles as seeds for secondary organic aerosol in the Amazon, *Science*, **337**, 1075–1078, 2012.

Pöschl, U.: Atmospheric aerosols: composition, transformation, climate and health effects, *Angew. Chem. Int. Edit.*, **44**, 7520–7540, 2005.

Raabe, J., Tzvetkov, G., Flechsig, U., Böge, M., Jaggi, A., Sarafimov, B., Vernooij, M. G. C., Huthwelker, T., Ade, H., Kilcoyne, D., Tyliszczak, T., Fink, R. H., and Quitmann, C.: PolLux: a new facility for soft x-ray spectromicroscopy at the Swiss Light Source, *Rev. Sci. Instrum.*, **79**, 113704, 2008.

Razumovskii, S. D. and Zaikov, G. E.: Kinetics and mechanism of ozone reactions with dual reactivity points, *Usp. Khim.+*, **49**, 2344–2376, 1980.

Renbaum, L. H. and Smith, G. D.: The importance of phase in the radical-initiated oxidation of model organic aerosols: reactions of solid and liquid brassidic acid particles, *Phys. Chem. Chem. Phys.*, **11**, 2441–-2451, 2009.

Rogge, W. F., Mazurek, M. A., Hildemann, L. M., Cass, G. R., and Simoneit, B. R. T.: Quantification of urban organic aerosols at a molecular-level – identification, abundance and seasonal-variation, *Atmos. Environ.*, **27**, 1309–1330, 1993.

Russell, L. M., Maria, S. F., and Myneni, S. C. B.: Mapping organic coatings on atmospheric particles, *Geophys. Res. Lett.*, **29**, 1779, 2002.

Saukko, E., Lambe, A. T., Massoli, P., Koop, T., Wright, J. P., Croasdale, D. R., Pedernera, D. A., Onasch, T. B., Laaksonen, A., Davidovits, P., Worsnop, D. R., and Virtanen, A.: Humidity-dependent phase state of SOA particles from biogenic and anthropogenic precursors, *Atmos. Chem. Phys.*, **12**, 7517–7529, 2012.

Saxena, P. and Hildemann, L.: Water-soluble organics in atmospheric particles: a critical review of the literature and application of thermodynamics to identify candidate compounds, *J. Atmos. Chem.*, **24**, 57–109, 1996.

Shiraiwa, M. and Seinfeld, J. H.: Equilibration timescale of atmospheric secondary organic aerosol partitioning, *Geophys. Res. Lett.*, **39**, L24801, 2012.

Shiraiwa, M., Pfrang, C., and Pöschl, U.: Kinetic multi-layer model of aerosol surface and bulk chemistry (KM-SUB): the influence of interfacial transport and bulk diffusion on the oxidation of oleic acid by ozone, *Atmos. Chem. Phys.*, **10**, 3673–3691, 2010.

Shiraiwa, M., Ammann, M., Koop, T., and Pöschl, U.: Gas uptake and chemical aging of semisolid organic aerosol particles, *P. Natl. Acad. Sci. USA*, **108**, 11003–11008, 2011.

Shiraiwa, M., Selzle, K., Yang, H., Sosedova, Y., Ammann, M., and Pöschl, U.: Multiphase Chemical Kinetics of the Nitration of Aerosolized Protein by Ozone and Nitrogen Dioxide, *Environ. Sci. Technol.*, **46**, 6672–-6680, 2012.

Steimer, S. S., Krieger, U. K., Te, Y.-F., Lienhard, D. M., Huisman, A. J., Ammann, M., and Peter, T.: Electrodynamic balance measurements of thermodynamic, kinetic, and optical aerosol properties inaccessible to bulk methods, *Atmos. Meas. Tech. Discuss.*, **8**, 689-719, 2015.

Takahama, S., Gilardoni, S., Russell, L. M., and Kilcoyne, A. L. D.: Classification of multiple types of organic carbon composition in atmospheric particles by Scanning Transmission X-ray Microscopy analysis, *Atmos. Environ.*, **41**, 9435–9451, 2007.

Utter, R. G., Burkholder, J. B., Howard, C. J., and Ravishankara, A. R.: Measurement of the mass accommodation coefficient of ozone on aqueous surfaces, *J. Phys. Chem.-US*, **96**, 4973–4979, 1992.

Virtanen, A., Joutsensaari, J., Koop, T., Kannosto, J., Yli-Pirilä, P., Leskinen, J., Mäkelä, J. M., Holopainen, J. K., Pöschl, U., Kulmala, M., Worsnop, D. R., and Laaksonen, A.: An amorphous solid state of biogenic secondary organic aerosol particles, *Nature*, **467**, 824–827, 2010.

Worsnop, D. R., Morris, J. W., Shi, Q., Davidovits, P., and Kolb, C. E.: A chemical kinetic model for reactive transformations of aerosol particles, *Geophys. Res. Lett.*, **29**, 1996, 2002.

Yeung, M. C., Lee, A. K. Y., and Chan, C. K.: Phase transition and hygroscopic properties of internally mixed Ammonium Sulfate and Adipic Acid (AS-AA) particles by optical microscopic imaging and raman spectroscopy, *Aerosol Sci. Tech.*, **43**, 387–399, 2009.

Zahardis, J. and Petrucci, G. A.: The oleic acid-ozone heterogeneous reaction system: products, kinetics, secondary chemistry, and atmospheric implications of a model system – a review, *Atmos. Chem. Phys.*, **7**, 1237–1274, 2007.

Zelenay, V., Ammann, M., Krepelova, A., Birrer, M., Tzvetkov, G., Vernooij, M. G. C., Raabe, J., and Huthwelker, T.: Direct observation of water uptake and release in individual submicrometer sized ammonium sulfate and ammonium sulfate/adipic acid particles using x-ray microspectroscopy, *J. Aerosol Sci.*, **42**, 38–51, 2011a.

Zelenay, V., Huthwelker, T., Krepelova, A., Rudich, Y., and Ammann, M.: Humidity driven nanoscale chemical separation in complex organic matter, *Environ. Chem.*, **8**, 450–460, 2011b.

Zelenay, V., Mooser, R., Tritscher, T., Křepelová, A., Heringa, M. F., Chirico, R., Prévôt, A. S. H., Weingartner, E., Baltensperger, U., Dommen, J., Watts, B., Raabe, J., Huthwelker, T., and Ammann, M.: Aging induced changes on NEXAFS fingerprints in individual combustion particles, *Atmos. Chem. Phys.*, **11**, 11777–11791, 2011c.

Zhang, Q., Jimenez, J. L., Canagaratna, M. R., Allan, J. D., Coe, H., Ulbrich, I., Alfarra, M. R., Takami, A., Middlebrook, A. M., Sun, Y. L., Dzepina, K., Dunlea, E., Docherty, K., DeCarlo, P. F., Salcedo, D., Onasch, T., Jayne, J. T., Miyoshi, T., Shimono, A., Hatakeyama, S., Takegawa, N., Kondo, Y., Schneider, J., Drewnick, F., Borrmann, S., Weimer, S., Demerjian, K., Williams, P., Bower, K., Bahreini, R., Cottrell, L., Griffin, R. J., Rautiainen, J., Sun, J. Y., Zhang, Y. M., and Worsnop, D. R.: Ubiquity and dominance of oxygenated species in organic aerosols in anthropogenically-influenced Northern Hemisphere midlatitudes, *Geophys. Res. Lett.*, **34**, L13801, 2007.

Zhou, S., Shiraiwa, M., McWhinney, R. D., Pöschl, U., and Abbatt, J. P. D.: Kinetic limitations in gas-particle reactions arising from slow diffusion in secondary organic aerosol, *Faraday Discuss.*, **165**, 391–406, 2013.

Zobrist, B., Marcolli, C., Pedernera, D. A., and Koop, T.: Do atmospheric aerosols form glasses?, *Atmos. Chem. Phys.*, **8**, 5221–5244, 2008.

Zobrist, B., Soonsin, V., Luo, B. P., Krieger, U. K., Marcolli, C., Peter, T., and Koop, T.: Ultra-slow water diffusion in aqueous sucrose glasses, *Phys. Chem. Chem. Phys.*, **13**, 3514–3526, 2011.

Supplementary material

Carbon contamination and spectral distortion

Carbon contamination of the optical elements and windows of the beamline is a problem for measurements at the carbon edge since it preferentially absorbs X-rays in the carbon K-edge - the spectral region of interest. This directly leads to a significant dip in the spectrum of the X-ray flux arriving at the detector and hence a reduction of count statistics and thereby increases noise. However, it also increases the relative contribution of higher order light since the X-rays passed by the monochromator at 2 and 3 times the nominally set photon energy (due to higher diffraction orders of the grating) is absorbed by the contamination far less strongly. Commonly utilized X-ray detectors do not separate X-ray photons of different energies and all counted X-rays are assumed to be of the principal photon energy, despite the fact that they interact with the sample very differently (usually much more penetrating). This tends to make the sample appear more transparent than it actually is, leading to a distortion of the spectrum. The amount of distortion can vary rapidly with photon energy across the carbon K-edge, largely because the principal spectrum is strongly affected by the beamline contamination, while the higher order contribution is fairly constant. As a general rule, one can expect the spectral distortions to be greatest where the detected signal is closest to zero.
An example of this can be seen in Figure 3.7, which shows the spectra of two particles from different samples, measured at beamtimes more than one year apart. The grey spectrum (particle 1) shows a strong distortion between 287 eV and 304 eV, in the energy region where the incident X-ray flux (blue, dashed line) is lowest and thus the relative contribution of higher order light is largest. The black spectrum (particle 2) was measured without the microreactor and after cleaning some of the optical elements, thereby reducing the influence of higher order light. This spectrum therefore shows much stronger absorption at 287 eV to 304 eV. This comparison also demonstrates that other energy regions (e.g. below 287 eV) are not significantly affected by the problem. Since we are only interested in spectral features outside the affected region for data analysis, distorted spectra can be included in our dataset without problems.

Figure 3.8 presents the spectrum of shikimic acid measured with optimized measurement parameters in order to show the more subtle features. For a more de-

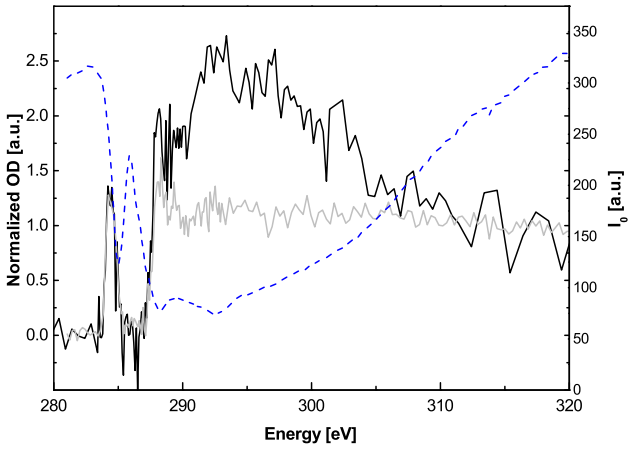

Figure 3.7: Spectrum of shikimic acid extracted from stack measurements of a particle measured at high levels of carbon contamination and low I0 (solid gray line), defocused line spectrum of a shikimic acid particle measured at low contamination and high I0 (solid black line) and a typical I0 spectrum with strong carbon contamination (dashed blue line).

tailed discussion of the problems encountered in carbon K-edge spectroscopy and approaches in solving these issues see Watts et al. (2006).

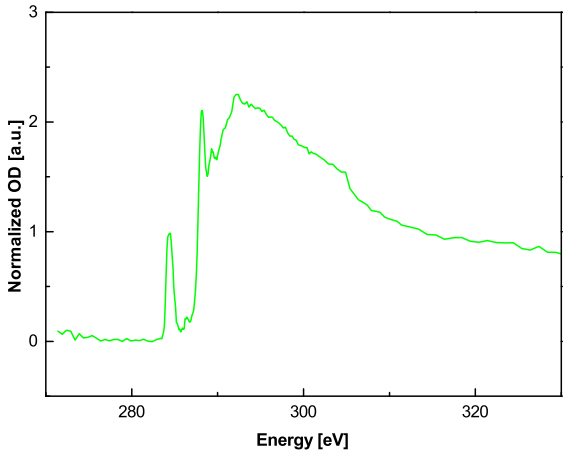

Figure 3.8: Optimized spectrum of shikimic acid

Particle shape

To determine particle shape, we compared the OD cross sections of unoxidized particles to the projection of a circle and a semicircle. Figure 3.9 is showing such a comparison for two particles at different humidities (0 % and 71 %). It can be seen that the shape of the dry particle is between spherical and hemispherical while the particle at 71 % RH is clearly flatter than hemispherical. Analysis of multiple OD cross sections shows this to be a general trend. However, no complete quantitative reconstruction is possible due to low contrast of the images.

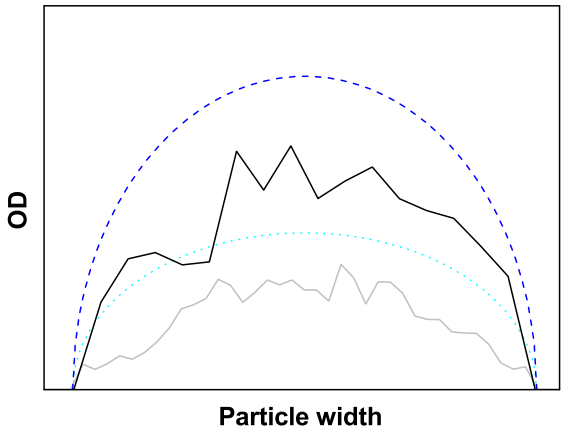

Figure 3.9: Example of a dry particle (black line) and a wet particle (71 %, grey line) cross section in comparison with the projection of a circle (dark blue, dashed line) and a semicircle (light blue, dotted line)

Chemical mapping

Chemical maps can be used to identify chemical inhomogenities. STXM-NEXAFS has previously been demonstrated to reveal the presence of chemical heterogenities on the order of 100 nm from spatial analysis of STXM images (Takahama et al., 2010). To demonstrate the capability of our experimental setup to identify small chemical heterogenities, we show here an image of a particle with an accidental contamination (suppl. Figure 3.10). These carbonaceous impurities of an unknown nature were found only during measurement of the 12 % RH sample in 3 out of 33 measured particles.

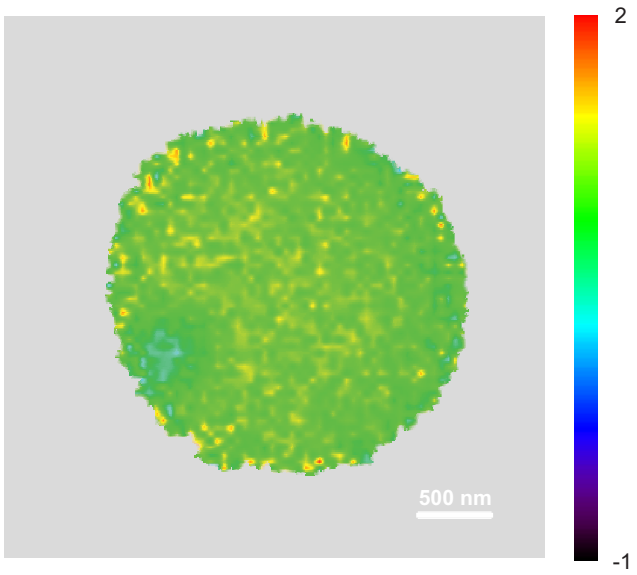

Figure 3.10: Chemical map showing the distribution of the shikimic acid double bond in an unoxidized particle at 13 % RH containing an inclusion of an accidental contamination.

Bibliography

Watts, B., Thomsen, L., and Dastoor, P. C.: Methods in carbon K-edge NEXAFS: Experiment and analysis, *J. Electron. Spectrosc. Relat. Phenom.* **151**, 105–120, 2006.

Takahama S., Liu S. and Russell, L. M.: Coatings and clusters of carboxylic acids in carbon-containing atmospheric particles from spectromicroscopy and their implications for cloud-nucleating and optical properties, *J. of Geophys. Res.*, **115**, D01202, 2010.

CHAPTER 4

Kinetics of ozone uptake on shikimic acid: flow tube experiments and modeling

Steimer, S. S., Berkemeier, T., Gilgen, A., Peter, T., Shiraiwa, M., and Ammann, M., in preparation for submission to *Phys. Chem. Chem. Phys.*

4.1 Abstract

Aging of particulate organic matter affects the composition and properties of atmospheric aerosol particles. Driven by temperature and humidity, the organic fraction can vary its physical state between liquid and amorphous solid, or rarely even crystalline. These transitions can influence the reaction kinetics due to varying limitations of mass transport, which in turn may influence the chemical aging of particles containing such compounds. We have used coated wall flow tube experiments to investigate the reaction kinetics of the ozonolysis of shikimic acid, which serves as a proxy for oxygenated, water soluble organic matter and can form a glass at room temperature. Particular attention was paid to how the presence of water influences the reaction, since it acts a plasticizer and thereby induces

changes in physical state. We analyzed the results by means of a traditional resistor model, which assumes steady-state conditions, and by a kinetic multi-layer flux model. The ozonolysis rate of shikimic acid is strongly increased in presence of water, a fact we attribute to the increased transport of O_3 and shikimic acid through the condensed phase at lower viscosities. The analysis with the resistor model suggests that the system undergoes both surface and bulk reaction. The second order rate constant of the bulk reaction is $(1.5 \pm {}^{1.5}_{0.5}) \times 10^3\ \mathrm{L\,mol^{-1}\,s^{-1}}$. At low humidities and long timescales the resistor model fails to describe the measurements, calling for alternative evaluation methods. The fit of the flux model results to the experimental data was optimized with a uniformly-sampled Monte-Carlo search combined with a genetic algorithm. Optimization of the flux model input parameters produces input parameter sets which fit the experimental data reasonably well with respect to the humidity dependence of the uptake. The flux model output confirms the presence of a surface reaction and suggests diffusion of shikimic acid in the condensed phase to be the limiting factor in the uptake at low humidity. However, no global parameter set was found which could convincingly explain all features of the experimental data, indicating a clear need for further refinement of the constraints on the input parameters and improvement of both the flux model, in terms of the representation of the processes involved, and the optimization method.

4.2 Introduction

Organic matter (OM) constitutes a significant fraction of the atmospheric aerosol mass (Kanakidou et al., 2005; Zhang et al., 2007). Aerosols undergo physical and chemical aging in the atmosphere, which can change properties such as absorptivity (Bones et al., 2010), hygroscopicity (Vesna et al., 2008) and toxicity (Segal-Rosenheimer and Dubowski, 2007). OM in aerosols has often been assumed to be well mixed, with respect to both gas-particle partitioning (Pankow, 1994; Odum et al., 1996) and reactions in the condensed phase (subsequently termed "bulk", in contrast to the surface region). This provides the basis for theoretical descriptions of secondary organic aerosols (SOA). However, recent studies of glass transition temperatures (Koop et al., 2011), particle bouncing behaviour (Virtanen et al., 2010), evaporation (Vaden et al., 2011; Abramson et al., 2013; Loza et al., 2013), thermal desorption (Cappa and Wilson, 2011) and response to physical

deformation (Renbaum-Wolff et al., 2013) show that OM can adopt a semi-solid or amorphous solid (glassy) state under environmental conditions. The self-diffusion coefficient in a glassy solid compared to a liquid matrix can drop to less than 10^{-20} $cm^2\,s^{-1}$, while the change in diffusivity of small guest molecules is much smaller (e.g. from 10^{-5} $cm^2\,s^{-1}$ to less than 10^{-10}-10^{-12} $cm^2\,s^{-1}$ for water at room temperature Koop et al., 2011). These changes in diffusion coefficients have important implications for mass transport based processes such as, for example, evaporation. A study by Abramson et al. (2013) on pyrene evaporation from α-pinene-derived SOA shows that pyrene present during SOA formation gets trapped and only evaporates slowly due to diminished diffusion within the bulk. Another example is a study on nonequilibrium formation and growth of SOA by Perraud et al. (2012), where organic nitrates were buried in α-pinene-derived SOA instead of following equilibrium partitioning. As diffusivity influences the supply of reactants, changes in physical state have the potential to change reaction rates and kinetic regime, which will in turn influence aerosol properties and lifetime.
First investigations of this phenomenon were performed by Shiraiwa et al. (2011) in a study on the ozonolysis of protein films, where a decrease in reactive uptake with decreasing humidity was ascribed to kinetic limitation by bulk diffusion. There are several other studies dealing with the influence of physical state on reactivity; for instance, Kuwata and Martin (2012) showed that formation of organonitrogen compounds in α-pinene SOA is contingent on high relative humidity (RH) while Zhou et al. (2013) saw a clear limitation of the reaction of benzo[a]pyrene with ozone (O_3) under dry conditions when coated with α-pinene SOA. In all three studies, changes in physical state were induced by varying RH, as water can act as a plasticizer for water soluble compounds.

We are using the same principle to probe the effect of limited diffusivity on shikimic acid at longer timescales and under a large number of different humidities and [O_3] to access a variety of kinetic regimes and provide a comprehensive dataset for kinetic modelling. Shikimic acid ((3R,4S,5R)-3,4,5-trihydroxycyclohex-1-ene-1-carboxylic acid) is a carboxylic acid which has been detected in biomass burning aerosol (Medeiros and Simoneit, 2008). It can be considered a proxy for a highly oxidized, water soluble OM. Its cyclic double bond is expected to react with O_3 in a Criegee reaction (Criegee, 1975) cleaving the bond and leading to more highly oxidized reaction products. We have previously shown that shikimic acid undergoes humidity induced glass transition (Chapter 2/Steimer et al., 2015) and that changes in humidity are accompanied by changing degradation rates, as

assessed by scanning transmission X-ray microscopy (STXM), combined with near edge X-ray absorption fine structure (NEXAFS) spectroscopy (Chapter 3/Steimer et al., 2014). On the long timescales observable in the STXM-NEXAFS experiments, this behaviour was found to be most consistent with classic reacto-diffusion limited kinetics. However, due to low time resolution of these measurements and difficulties to quantify $[O_3]$, further experiments are needed. In this study, we use coated wall flow tube (CWFT) measurements combined with the kinetic multilayer model KM-SUB (Shiraiwa et al., 2010) to provide a comprehensive analysis of the different kinetic regimes and their dependence on humidity and therefore physical state. This serves as a case study for the changing kinetics of glass-forming organics under changing environmental conditions. Additionally, we demonstrate the differences arising from usage of resistor model formulations vs. depth resolved models, which highlights the needs for depth-resolved modeling.

4.3 Methods

4.3.1 Experimental

Apparatus. All uptake experiments were conducted using an atmospheric pressure CWFT reactor (length 48 cm, inner diameter 1.2 cm) coupled to a commercial O_3 analyzer (Photometric O3 Analyzer - Model 400E; TELEDYNE Instruments). The reactor tube was encased in a cooling jacket connected to a thermostat to regulate the temperature within the reactor. Temperature was set to 22.5 °C throughout all experiments. The reactor is fitted with an injector system to facilitate reactant exposure under equilibrated conditions. The injector consists of a stainless steel rod with an inner polytetrafluoroethylene (PTFE) tube and a PTFE end cap with two openings on opposing sides of the cap. A mixed gas flow of N_2, O_2, H_2O and O_3 is passed through the injector. When the outlet is located at the downstream end of the flow tube, the film is not exposed to O_3. Movement of the injector towards the upstream end of the flow tube exposes the flow tube coating to the injector gas flow and therefore the reactant O_3. A second gas flow feeds into the reactor on the upstream end. This sheath gas flow prevents back flow and keeps the film equilibrated to the selected RH when not exposed to the injector flow. The RH is adjusted by bubbling both gas flows through water reservoirs lo-

cated in the same thermostat bath. This humidifier setup is required to guarantee that RH stays constant upon exposure to the injector gas flow.

Oxidant generation and flow conditions. O_3 was generated by passing the mixed O_2/N_2 flow through a quartz tube exposed to a UV-source of adjustable intensity. The total flow was set to 520 $\mathrm{mL\,min^{-1}}$ with the O_2 fraction varying between 20 and 100 $\mathrm{mL\,min^{-1}}$. The N_2 sheath gas flow was set to 500 $\mathrm{mL\,min^{-1}}$ for all experiments. Using the given flow rates and fine tuning via lamp intensity, the O_3 concentration was varied from 90 to 1984 ppb. All flows within this section are given for STP conditions. The Reynolds number under present flow conditions is 134, indicating laminar flow.

Sample preparation. Flow tube coatings were prepared from a solution of 5.0 mg shikimic acid ($\geq 99\,\%$, Sigma-Aldrich) in 600 µL ethanol (reagent ACS, VWR). Prior to sample application, the glass tube was etched with 5 % hydrofluoric acid. After application and distribution of the solution on the flow tube, the film was pre-equilibrated with a 500 $\mathrm{mL\,min^{-1}}$ flow of 85 % RH N_2 for at least 30 min. The pre-equilibrated flow-tube was then inserted into the reactor casing for equilibration to the RH and temperature set for the respective experiment for at least 1 h.

Measurements. After measuring the O_3 baseline concentration without reaction, the injector was moved to the upstream end of the flow tube to expose the shikimic acid film to O_3. The subsequent change in O_3 concentration was monitored over at least 14 h, after which the injector was moved back upstream to measure the O_3 concentration without reaction once more and detect potential drifts in the O_3 baseline. Such drifts in concentration could arise from fluctuations in the UV-light intensity. For most experiments an additional measurement of the O_3 baseline was performed after ca. 20 min of exposure to further constrain potential drifts.
A minimum of three measurements at 177-179 ppb O_3 concentration were performed at the following humidities: 0 % RH, 24 % RH, 45 % RH, 69 % RH, 83 % RH and 92 % RH. For two of these humidities, 24 % and 92 %, three measurements each were conducted at three additional O_3 concentrations: 89-90 ppb, 495-496 ppb and 1984-1985 ppb. Figure 4.1 shows the raw data of a measurement at 83 % RH and 177 ppb O_3 as well as the same data corrected for drift in the O_3 baseline.

Where applicable, data were corrected for drift in the O_3 concentration using a power function $f(x) = a + b \cdot x^c$.

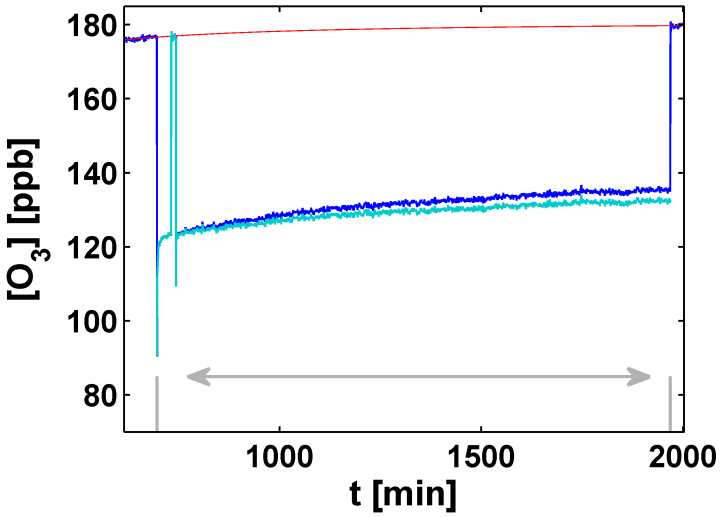

Figure 4.1: Ozone mixing ratio downstream of flow tube. Blue line: raw data of the O_3 loss as a function of time. Red line: power law fit to the O_3 baseline. Cyan line: corrected data (see text). Gray lines and arrow: time period of 21 h of exposure to O_3. Not shown: initialization period (first 2 h).

4.3.2 Determination of the uptake coefficient

The uptake coefficient, γ, describes the probability that a given molecule undergoing collision with a surface is subsequently taken up at that surface. It is defined as the net uptake normalized by the collision flux. It can be extracted from the measured O_3 concentrations assuming that the decay over the length of the flow tube follows pseudo-first order kinetics at each sampling time. In this case the decrease in O_3 can be described as:

$$\frac{\log[O_3]_{gs,l}}{\log[O_3]_{gs,0}} = k^I t_r = -\gamma \frac{\omega_{O_3}}{4} \frac{S}{V_g} t_r = \frac{\gamma \omega_{O_3} \pi d l}{4\varphi}, \tag{4.1}$$

where $[O_3]_{gs}$ describes molecular number density of O_3 in the gas phase near the surface in cm^{-3}: $[O_3]_{gs,0}$ is the number density at the entrance to the tube , while $[O_3]_{gs,l}$ describes the number density of O_3 at length l or equivalently at residence

time t_r [s] in the flow tube; k^{I} in s^{-1} is the pseudo-first order rate constant with respect to O_3, ω_{O_3} the mean thermal velocity of O_3 molecules in $\mathrm{cm\,s}^{-1}$ and S/V_{g} the ratio of surface area to gas phase volume in $\mathrm{cm}^2\,\mathrm{cm}^{-3}$; d [cm] describes the flow tube diameter and φ [$\mathrm{cm}^3\,\mathrm{s}^{-1}$] the volumetric flow rate. As $[O_3]_{\mathrm{gs},0}$ is assumed to stay constant during the measurements, γ can be determined from $[O_3]_{\mathrm{gs},0}$ and the measured value at $[O_3]_{\mathrm{gs},48\ \mathrm{cm}}$ (corresponding to the downstream end of the flow tube) at each sampling time during O_3 exposure. Since the measured $[O_3]$ are gas-phase instead of near-surface gas phase concentrations, corrections for the gradient arising from gas phase diffusion have to be made. We are using the diffusion correction by Murphy and Fahey (1987), based on the work by Cooney et al. (1974). For this method, the differential equation that governs the analyte mixing ratio as a function of axial and radial position in a cylindrical geometry under axial flow is solved using the boundary condition that a constant fraction of wall collisions result in reaction. This yields a transmission ratio corrected for wall loss. The calculated transmission ratios are then fitted to the experimental transmission ratio using γ as the only variable to determine the corrected value for the experimental γ.

4.3.3 KM-SUB model and global optimization

For a description of the reaction system without the limitation of steady-state assumptions, we use the kinetic multi-layer model KM-SUB. It couples mass-transport and chemical reactions at the surface and in the condensed phase of the organic film in a set of ordinary differential equations (Shiraiwa et al., 2010). As mentioned in the introduction, we also refer to the condensed phase as bulk, in accordance with the nomenclature of Shiraiwa et al. (2010) and current articles by the responsible IUPAC task group (Crowley et al., 2010; Ammann et al., 2013). KM-SUB consists of several compartments, namely from far distance towards the interior of the film: far-surface gas phase, near-surface gas phase, sorption layer, quasi-static surface layer and bulk layers. Mass transport between and within compartments is treated as chemical flux (Pöschl et al., 2007), generating a full concentration profile of all considered species. A list of explicitly treated mass transport processes includes: Gas-phase diffusion, Langmuir Hinshelwood-type surface adsorption/desorption on the particle surface, surface-bulk-exchange as well as bulk diffusion of trace gas and bulk material. The resulting list of kinetic input parameters for KM-SUB is given in Table 4.1.

We modify KM-SUB by introducing the parameter K_{bs}, which relates the instantaneous shikimic acid concentration in the near-surface bulk ($[Y]_{b1}$), i.e. in the topmost bulk layer labeled b1, to an equilibrium surface concentration in the quasi-static surface layer ($[Y]_{ss}$), i.e. a two-dimensional surface layer representing the surface-exposed fraction of the organic bulk matrix:

$$K_{bs} = \frac{[Y]_{ss}}{[Y]_{b1}}. \tag{4.2}$$

K_{bs} thus solves the problem of determining an effective concentration of reactive sites at a non-ordered surface. K_{bs} may be related to the surface tension if known as the surface tension depends on the surface concentration of shikimic acid.

Parameter	Unit	Description
k_{BR}^{II}	$cm^3\,s^{-1}$	Second order bulk reaction rate constant
k_{SLR}^{II}	$cm^2\,s^{-1}$	Second order surface layer reaction rate constant
k_{bs,O_3}	$cm\,s^{-1}$	Bulk to surface transfer rate coefficient for O_3
$k_{ssb,Y}$	s^{-1}	Surface to bulk transfer rate coefficient for shikimic acid
H	$mol\,cm^{-3}\,atm^{-1}$	Henry's law solubility of O_3
K_{bs}	cm	Equilibrium bulk to surface concentration ratio
τ_d	s	Desorption lifetime of O_3
$\alpha_{s,0}$	-	Surface accommodation coefficient
σ_{O_3}	cm^2	Adsorption cross-section of O_3
D_{g,O_3}	$cm^2\,s^{-1}$	Gas phase diffusivity of O_3
D_{b,O_3}	$cm^2\,s^{-1}$	Bulk diffusion coefficient of O_3
$D_{b,Y}$	$cm^2\,s^{-1}$	Self-diffusion coefficient of shikimic acid

Table 4.1: Kinetic input parameters for KM-SUB.

Furthermore, in the original KM-SUB model, k_{bs,O_3} and $k_{ssb,Y}$ are not independent input parameters, but parametrized by the corresponding diffusion coefficient. We here use a different parametrization, in which k_{bs,O_3} and $k_{ssb,Y}$ are decoupled from their respective diffusion constants. This allows for surface-exchange mechanisms that are not only governed by bulk diffusion, but might also be influenced by a reduced viscosity close to the surface of the film or surface tension effects. In this new parametrization, we introduce the factors f_{kbs,O_3} and $f_{kssb,Y}$ as additional input parameters for the model, so that

$$k_{bs,O_3} = \frac{2D_{b,O_3}}{L} f_{kbs,O_3} \tag{4.3}$$

and

$$k_{\mathrm{ssb,Y}} = \frac{2D_{\mathrm{b,Y}}}{LK_{\mathrm{bs}}} f_{k\mathrm{ssb,Y}} \tag{4.4}$$

where L is the thickness of the bulk layers. We have also simplified the geometrical factor in the equation.

In order to obtain a global kinetic parameter set which describes all experimental results, we used a global fitting method combining a uniformly-sampled Monte-Carlo (MC) search with a genetic algorithm (GA), i.e. a search heuristic that mimics the process of natural selection. In the MC search, kinetic parameters for KM-SUB were varied randomly within individual bounds. For each experimental run, the correlation between the uptake coefficient modeled by KM-SUB, $\gamma_{\mathrm{mod}}(t)$, and the experimentally determined uptake, $\gamma_{\mathrm{exp}}(t)$, was evaluated in a least-squares fashion. For each experimental run i, the residual R is calculated in log-space to account for the large range of γ observed during the experiments.

$$R = \frac{1}{I}\sum_{i}^{I}\frac{1}{J_i}\frac{1}{f_i}\sqrt{\sum_{j}^{J_i}\left(\log\gamma_{\mathrm{exp}}\left(t_j\right) - \log\gamma_{\mathrm{mod}}\left(t_j\right)\right)^2} \tag{4.5}$$

The data from each experimental run is weighted by its number of data points J_i and by a weighting constant f_i that accounts for scatter within each data set. In practice, we used for f_i the inverse of the minimal residue found for the single data set i. The globally best-fitting parameter sets, i.e. the sets with lowest R, were fed into the starting population of a genetic algorithm (Matlab Global Optimization Toolbox) in which they were optimized by processes resembling recombination and mutation in evolutionary biology. To ensure diversity within the pool of parameter sets and to counteract the sampling bias from shallow local minima, the same number of random KM-SUB input parameter sets was added to the starting population. In the GA step, the same parameter boundaries were used as in the preceding MC step. The optimization was stopped when the population was homogeneous and thus the increase in correlation to the experimental data had ceased. Both diffusion coefficients, $D_{\mathrm{b,O_3}}$ and $D_{\mathrm{b,Y}}$, are expected to vary with relative humidity (Shiraiwa et al., 2011), so for each humidity, an individual coefficient was assigned. For all other input parameters, RH-dependence was neglected and the same values for the input parameters are used for all experiments. $k_{\mathrm{bs,O_3}}$ and $k_{\mathrm{ssb,Y}}$ change automatically with RH due to their parametrization. Due to the large number of fitting parameters, a large number of KM-SUB model runs had to

be executed during the optimization procedure. In a typical optimization, 10 million single KM-SUB runs were performed, requiring about 1 day of computation time on 120 CPUs.

4.4 Results and discussion

The progression of the O_3 uptake with exposure time was measured at different RH and O_3 concentrations. Figure 4.2 shows γ as a function of time for six different RH and a fixed O_3 concentration of 177-179 ppb. The general progression is similar for all measurements: initially a plateau develops, which after about 2 min gives way to a lower, relatively stable long-term uptake, which after about 1 h slowly declines further, especially at lower humidity. With decreasing RH, γ decreases by about one order of magnitude from 6.0×10^{-7} at 0 % RH to 8.7×10^{-6} at 92 % RH (averaged value at 11 to 16 min exposure). Furthermore, the relative magnitude of the decrease from initial plateau to long-term value becomes smaller at higher RH and the slope of the decrease in long-term uptake varies between humidities. As the slope of the decrease depends on whether and how the baseline drift is corrected, there is some uncertainty in the exact slope. This is true in particular for uptake at low humidities where the absolute O_3 loss is small. However, the general trend is clear and consistent between measurements with and without baseline drift.
The dependence of γ on O_3 concentration at 24 % RH and 92 % RH is shown in Figure 4.3. In both cases, the height of the initial plateau decreases with increasing O_3 concentration until it basically vanishes at 1984-1985 ppb. As the collision flux is proportional to the O_3 concentration, γ will only stay constant with increasing gas-phase $[O_3]$ if the net uptake increases proportionally as well. This is the case for an Eley-Rideal reaction, as its reaction rate is directly proportional to the O_3 concentration in the gas phase. In case of a Langmuir-Hinshelwood type reaction, however, the reaction rate is proportional to the O_3 concentration on the surface, which in turn is only proportional to the gas-phase O_3 concentration as long as the surface is not saturated with O_3. At high $[O_3]$, once surface saturation is reached, only the collision rate increases while the net uptake stays constant, resulting in a decrease of γ. The decrease of the initial plateau with increasing O_3 therefore points to an involvement of a Langmuir-Hinshelwood type reaction in this time regime. At 24 % RH, the slope of the slow decrease of the steady-state uptake ($\geq 10^1$ min) stays nearly constant while at 92 % RH, a strong reduction in

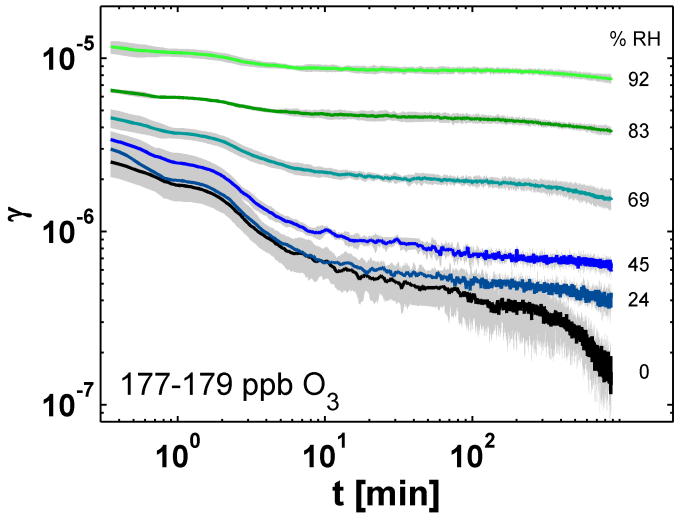

Figure 4.2: Evolution of γ at 177-179 ppb O_3 for six different humidities. From the bottom up: 0 % RH (black), 24 % RH (dark blue), 45 % RH (blue), 69 % RH (dark cyan), 83 % RH (green) and 92 % RH (bright green). Areas shaded in gray denote the standard deviations of the averaged measurements.

γ at 495-496 ppb and even more so at 1984-1985 ppb points towards a complete depletion of the organic film towards the end of the measurements ($\geq 10^3$ min). Integration of the measured O_3 loss over time yields a total loss of 1.66×10^{19} O_3 molecules. This is very close to the total number of shikimic molecules in the film (1.72×10^{19}), which confirms that the steeper decrease at these high O_3 concentrations at simultaneously high RH is caused by depletion of shikimic acid in the whole coated wall flow tube (CWFT) film.

4.4.1 Steady-state evaluation

As concluded from the shapes of the uptake curves above, at least two different reactive loss processes, surface and bulk reaction, must be involved in the total O_3 loss. In case of multiple loss processes, a resistor model can be applied to describe the system under steady-state assumptions. The resistor model formulation for a species X undergoing both surface and a bulk reaction is accordingly (Ammann et al., 2013):

$$\frac{1}{\gamma_X} = \frac{1}{\alpha_{s,0}} + \frac{1}{\frac{1}{\Gamma_b} + \frac{k_d}{\alpha_{s,0} k_{sb}}} + \Gamma_s \tag{4.6}$$

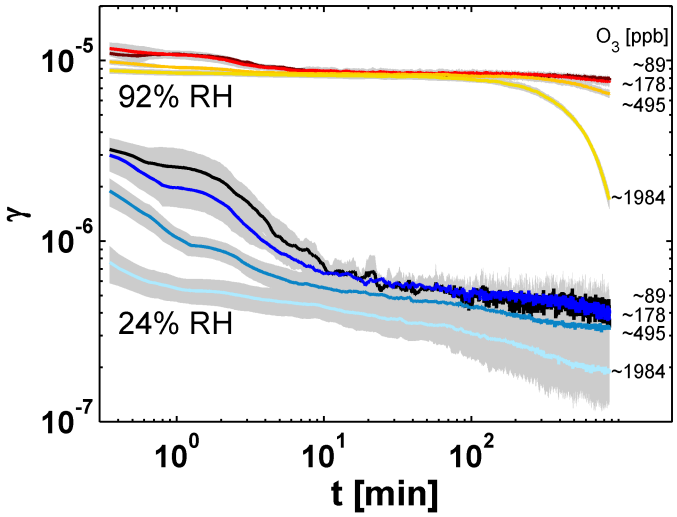

Figure 4.3: Evolution of γ for four different concentrations of O_3 at two different humidities: 24 % RH (89-90 ppb (black), 177-179 ppb (blue) 495-496 ppb (dark cyan), 1984-1985 ppb (light blue)) and 92 % RH (89-90 ppb (dark red), 177-179 ppb (red) 495-496 ppb (orange), 1984-1985 ppb (yellow)). Areas shaded in gray denote the standard deviations of the averaged measurements.

Where $\alpha_{s,0}$ is the initial surface accommodation coefficient, $1/\Gamma_s$ the resistance for uptake via surface reaction and $1/\Gamma_b$ the resistance for uptake via bulk reaction. k_d is the desorption rate constant. Its inverse corresponds to the desorption lifetime τ_d given in Table 4.1. k_{sb} is the solvation rate constant, describing the transformation from surface to bulk molecule for the volatile species.

Langmuir-Hinshelwood-dominated regime. Given the recommended bulk accommodation coefficient for O_3 on water ($> 10^{-3}$) (Ammann et al., 2013) and the fact that surface accommodation is necessarily larger than bulk accommodation, it is unlikely that surface accommodation is the rate limiting step. Equation 4.6 then simplifies to

$$\frac{1}{\gamma_X} = \frac{1}{\frac{1}{\frac{1}{\Gamma_b} + \frac{k_d}{\alpha_{s,0} k_{sb}}} + \Gamma_s} \tag{4.7}$$

in which case γ_X is the sum of a bulk process (solvation and bulk reaction) and a surface reaction. The surface reaction can therefore be easily separated. We assume that the decrease after the initial plateau indicates the end of the surface reaction, and therefore chose the γ_X averaged at 11-15 min to represent the initial

bulk process Γ_b. Γ_s can then be extracted by subtracting Γ_b from the total γ_X measured on the initial plateau. The results from plotting Γ_s as a function of gas-phase $[O_3]$ are shown in Figure 4.4. The values determined for Γ_s at 24 % RH are only between a factor of 1.2 and 2.3 lower than for 92 % RH, compared to the more than one order of magnitude for γ_X measured on the second, bulk dominated plateau. This suggests that the surface reaction is not strongly influenced by changes in humidity. Γ_s is strongly dependent on gas-phase $[O_3]$, which, as already mentioned, points to a Langmuir-Hinshelwood process. The uptake coefficient of a Langmuir-Hinshelwood surface reaction of O_3 with a second species Y residing on the surface can be described by the following equations (Ammann et al., 2003)

$$\frac{1}{\Gamma_s} = \frac{\omega_{O_3}\sigma_{O_3}\left(1 + K_{LH}[O_3]_{gs}\right)}{4k^{I}_{SLR}K_{LH}} \tag{4.8}$$

with

$$K_{LH} = \frac{\sigma_{O_3}k_a}{k_d} \tag{4.9}$$

and

$$k^{I}_{SLR} = k^{II}_{SLR}[Y]_s \tag{4.10}$$

where k^{I}_{SLR} is the first order surface layer reaction rate constant in s^{-1}, σ_{O_3} the occupied surface area per adsorbed molecule of O_3 in $cm^2\,molecule^{-1}$, K_{LH} the Langmuir constant in $cm^3\,molecule^{-1}$, k_a the adsorption rate constant in $cm\,s^{-1}$, k^{II}_{SLR} the second order surface reaction rate constant in $cm^2\,molecule^{-1}\,s^{-1}$ and $[Y]_s$ the surface concentration of Y. Equation 4.8 reveals that the decrease in Γ_s with increasing $[O_3]_{gs}$ at high concentrations is caused by the limited availability of adsorption sites. Equation 4.8 was fitted to the experimental data. In the form written above, we have three unknown variables in the equation: K_{LH}, k^{I}_{SLR}, and σ_{O_3}. $1/\sigma_{O_3}$ equals N_{max}, the number of adsorbed molecules of O_3 on a fully-covered surface per cm^2. In the high concentration limit, the slope of a logarithmic plot of γ against $[O_3]$ shown in Figure 4.4 is -1. The absolute values of the linear part of the function are given by the product of k^{I}_{SLR} and N_{max}, i.e. changing these variable causes a vertical parallel shift. The concentration where the function curves (transition to the low concentration regime) depends on K_{LH}. It is therefore possible to determine 3×10^{-13} $cm^3\,molecule^{-1}$ as a lower limit for K_{LH} (dashed curve in Figure 4.4). At K_{LH}-values lower than that, the absolute values of the plateau could still be adjusted via k^{I}_{SLR} and N_{max}, but transition to the linear regime would come too late. The available data do not allow determining an

upper limit for K_{LH}. While the data points do indicate a slight curvature that could be interpreted as the beginning of the low concentration plateau, the error is too large to really draw this conclusion. Measurements at lower $[O_3]$ would be needed to determine at which concentration the slope decreases.
The lower limit of $K_{LH} = 3 \times 10^{-13}$ cm^3 molecule^{-1} compares well with K_{LH}-values for ozonolysis of polycyclic aromatic hydrocarbons (PAHs) such as benzo[a]pyrene, where K_{LH} is between 2.8×10^{-13} cm^3 molecule^{-1} (Pöschl et al., 2001) and 1.2×10^{-15} cm^3 molecule^{-1} (Kwamena et al., 2004) and anthracene, where K_{LH} ranges from 1.0×10^{-13} cm^3 molecule^{-1} to 2.2×10^{-15} cm^3 molecule^{-1} (Kwamena et al., 2007). While it is not possible to separate k^{I}_{SLR} and N_{max} from the data, 3×10^{14} cm^{-2} can be seen as the upper limit for N_{max}. This gives a value around 1.5×10^{-4} s^{-1} as the lower limit for k^{I}_{SLR}. We also estimated the O_3 loss due to the surface reaction by subtracting the integral of the ozone loss due to bulk processes from the total integral. The average ozone loss at 11-15 min was used to calculate the bulk integral. The integrated surface O_3 loss varies between 6×10^{14} and 3×10^{15} molecules. This is only slightly more than a monolayer, which supports the idea that the plateaus are caused by surface reactions. Overestimation of the total loss as well as differences between the calculated losses are most likely due to how the bulk loss was extrapolated. The fact that plateaus at the same humidity do not differ in length supports the assumption that they are caused by a Langmuir-Hinshelwood reaction in the surface-saturated regime.

Reacto-diffusion-limited regime. After the decline of the first plateau during the first minutes of the exposure, the system settles for a slowly declining long term pseudo steady-state uptake, which, as described above, may be bulk dominated. In this case, Eq. 4.7 simplifies to

$$\frac{1}{\gamma_X} = \frac{k_d}{\alpha_{s,0} k_{sb}} + \frac{1}{\Gamma_b} = \frac{1}{\alpha_{b,0}} + \frac{1}{\Gamma_b} \tag{4.11}$$

Considering the IUPAC-recommended value of $\alpha_{b,0} > 1 \times 10^{-3}$ for O_3 on water (Ammann et al., 2013), the contribution of $\alpha_{b,0}$ to the limitation is negligible and the equation simplifies to

$$\gamma_X = \Gamma_b \tag{4.12}$$

Knowing that the condensed phase is liquid at 92 % RH and the reaction must be relatively slow, O_3 should be well-mixed within a large part of the bulk. We

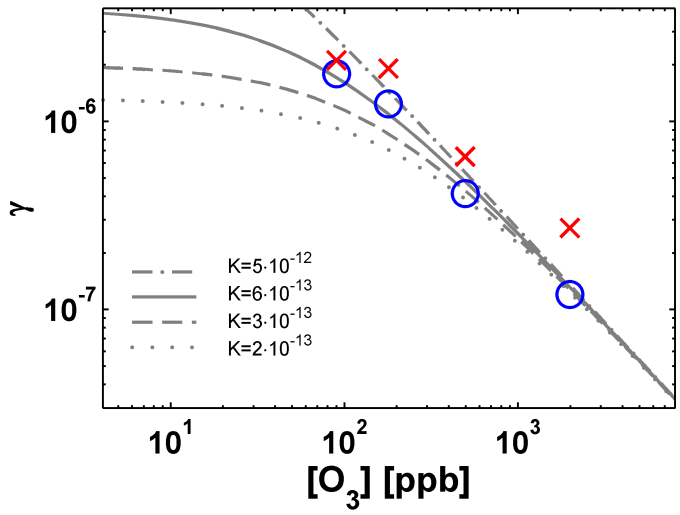

Figure 4.4: Dependence of Γ_s on O_3 concentration. Blue circles show experimental data at 24 % RH, red crosses at 92 % RH. The gray lines show fits of Eq. 4.8 to the experimental data at 24 % RH, using the following values: $k^{I}_{SLR} = 2 \times 10^{-4}\ s^{-1}$, $N_{max} = 3 \times 10^{14}\ cm^{-2}$ and $K_{LH} = 5 \times 10^{-12}\ cm^3\,molecule^{-1}$ (dash-dotted line), $6 \times 10^{-13}\ cm^3\,molecule^{-1}$ (solid line), $3 \times 10^{-13}\ cm^3\,molecule^{-1}$ (dashed line), and $2 \times 10^{-13}\ cm^3\,molecule^{-1}$ (dotted line).

can then assume a bulk reaction limited case to determine the second-order rate constant of the reaction from the following equation (Ammann et al., 2013):

$$k^{II}_{BR} = \frac{\gamma_X \omega_{O_3} \frac{S}{V_b}}{4HRT[Y]_b} \tag{4.13}$$

where k^{II}_{BR} is the second order rate constant of the bulk reaction, S/V_b the ratio of film surface to film volume, H the Henry constant, R the gas constant, T the temperature and $[Y]_b$ the concentration of shikimic acid in the film. We are using a Henry constant of $H = 1.3 \times 10^{-2}\ mol\,L^{-1}\,atm^{-1}$ for O_3 in water (Utter et al., 1992) and a shikimic acid concentration of 3.38 $mol\,L^{-1}$. All shikimic acid bulk concentrations used in this study were deduced from hygroscopycity measurements of levitated particles in an EDB (Chapter 2/Steimer et al., 2015). The calculated second order rate constant is $(1.5 \pm 0.5) \times 10^3\ L\,mol^{-1}\,s^{-1}$, which is only a factor of 2 slower than the second order rate constant determined from STXM-NEXAFS measurements, in which it was derived from the degradation rate of shikimic acid (Chapter 3/Steimer et al., 2014). The rate is therefore showing a good agreement between the two techniques. The slight difference in results could be explained by

both errors associated with the measurements and the fact that the measurement used for extraction of the rate constant with STXM was conducted at a lower humidity (82 % RH). The determined rate constant of shikimic acid with O_3 is comparable to similarly functionalized compounds in aqueous solution, such as maleic acid (1×10^3 L mol^{-1} s^{-1}) and fumaric acid (6×10^3 L mol^{-1} s^{-1}) (Hoigné and Bader, 1983). It is about three orders of magnitude lower than the second-order rate constant of O_3 and oleic acid (1×10^6 L mol^{-1} s^{-1}, Razumovskii and Zaikov, 1980), a compound frequently used as a proxy for assessment of condensed phase oxidation kinetics of OM (Zahardis and Petrucci, 2007).
With decreasing humidity, the uptake decreases, despite the increase in shikimic acid concentration. Since the condensed phase becomes more and more viscous, diffusion of O_3 into the bulk becomes slower. Reacto-diffusive limitation of the uptake could in principle explain the decrease in γ_X with decreasing humidity. Subsequently we investigate this hypothesis. Reacto-diffusive uptake is described by the following equation (Ammann et al., 2013):

$$\Gamma_b = \frac{4HRT}{\omega_{O_3}} \sqrt{D_{b,O_3} k_{BR}^{II} [Y]_b} \tag{4.14}$$

where D_{b,O_3} is the diffusion coefficient of O_3 in the bulk. As apparent from Eq. 4.13 and Eq. 4.14, Γ_b is independent of the gas phase ozone concentration (in contrast to Γ_s discussed above). This is obviously the case for the measurements at high relative humidity, but less so for the measurement at 24 % RH. In a first approach we nevertheless assume that Eq. 4.14 describes the quasi-steady state uptake coefficient of the bulk reaction limited plateau. Figure 4.5b shows the values of the averaged uptake coefficient at time 11-15 min as a function of relative humidity. The general trend of decreasing steady state ozone uptake to shikimic acid with decreasing RH is consistent with the decelerating shikimic acid degradation with decreasing humidity in our previous STXM study. Since the solubility of ozone in general rather slightly increases with decreasing polarity of organic solvents (Biń, 2006), we assume that a change in solubility of ozone is not the cause for this decrease. If we also assume that the reaction rate constant is independent of the shikimic acid concentration, the obvious parameter varying with water content is the diffusion coefficient. The squares in Figure 4.5a show the values of D_{b,O_3} necessary to obtain the measured uptake coefficients according to Eq. 4.14, with the other parameters except the shikimic acid concentration kept fixed. The diffusion coefficients for this flow tube study are compared with D_{b,O_3} data inferred

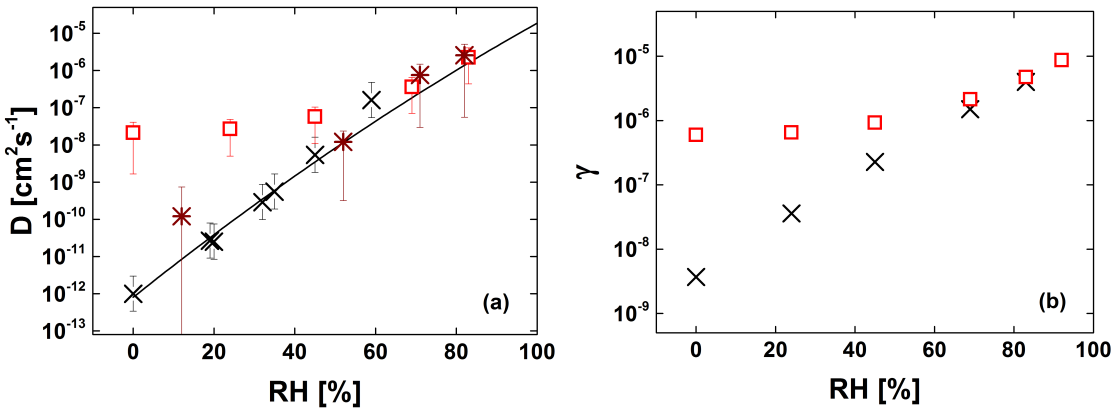

Figure 4.5: (a) O_3 diffusion coefficients from flow tube (295.7 K, red squares) and STXM (298 K, dark red asterisks) measurements as well as water diffusion coefficients from EDB measurements (293.5 K, measured data: black crosses, parameterization: black line). (b) Humidity dependent O_3 uptake measured in this study (red squares) and calculated from D_{b,H_2O} (parameterized from EDB data and assuming reacto-diffusive limitation, black crosses).

from the STXM-NEXAFS experiments (Chapter 3/Steimer et al., 2014) as well as D_{b,H_2O} determined from EDB measurements (Chapter 2/Steimer et al., 2015). The values for all three techniques agree well at higher humidities. While the diffusion coefficients determined for water via EDB and those for O_3 inferred from the STXM-NEXAFS measurements are also in agreement at low RH, values derived from Γ_b, obtained here, are consistently larger below 40 % RH. At 0 % RH, the value for D_{b,O_3} determined from the flow tube measurements is four orders of magnitude larger than the one derived from the EDB measurements. In turn, uptake coefficients calculated from Eq. 4.14 through insertion of the D_{b,H_2O} measured with the EDB are much smaller than the γ actually measured in the flow tube (Figure 4.5b). While the diffusion coefficient measured with EDB was for water and not O_3, the molecules are sufficiently similar that this cannot explain the large difference observed between measured diffusion coefficients and those inferred from Γ_b. Additionally, the D_{b,O_3} values inferred from the STXM-NEXAFS measurement support the EDB data. It is therefore clear that Eq. 4.14 does not adequately describe the system. In the reacto-diffusion limited regime, the reacto-diffusive length l_{O_3} describes the characteristic length a gas-phase molecule can

diffuse into the bulk before it reacts. At the distance l_{O_3}, the O_3 concentration in the bulk has dropped to $1/e$. l_{O_3} can be calculated by the following equation:

$$l_{O_3} = \sqrt{\frac{D_{b,O_3}}{k_{BR}^{II}[Y]_b}} \tag{4.15}$$

At 92 % RH, the reacto-diffusive length is 440 nm under the assumption $D_{b,O_3} = 1 \times 10^{-5}$ cm^2 s^{-1}. This is only slightly lower than the film thickness of 470 nm, which justifies the treatment of the reaction kinetics at 92 % RH as bulk reaction limited. However, as the true $[O_3]_b$ is lower than the value assumed by using Eq. 4.13, $(1.5 \pm 0.5) \times 10^3$ L mol^{-1} s^{-1} is a lower limit for k_{BR}^{II}. From estimation of the error in $[O_3]_b$, we suggest $+1.5 \times 10^3$ L mol^{-1} s^{-1} as the maximum positive error in k_{BR}^{II}. At 69 % RH, l_{O_3} is 60 nm. Given the film thickness of 250 nm, this clearly indicates reacto-diffusive limitation. As the discrepancy between $D_{b,O_3}$and D_{b,H_2O} indicates that the shikimic acid-O_3-water system does not follow pure reacto-diffusive limitation any more even at 45 % RH, we refrain from determining l_{O_3} at humidities ≤ 45 %. Deviations from the reacto-diffusive regime were expected at very low RH due to the decreasing diffusivity of shikimic acid. The characteristic chemical lifetime of shikimic acid is

$$\tau_Y = \frac{1}{k_{BR}^{II}[O_3]_b} \tag{4.16}$$

At 500 ppb, τ_Y is about 1×10^5 s. The upper limit of $D_{b,Y}$ for mass transport limitation of the reaction due to diffusion of shikimic acid would be given when diffusion becomes too slow to transport shikimic acid from the bottom of the film to the surface within τ_Y. The upper limit for $D_{b,Y}$ can therefore be calculated with

$$D_{b,Y} = \frac{{r_p}^2}{2\tau_Y}, \tag{4.17}$$

where r_p is the film thickness. Using the film thickness at 0 % RH (190 nm), $D_{b,Y} \approx 2 \times 10^{-15}$ cm^2 s^{-1} is the upper limit for diffusion limitation with regards to shikimic acid. Such diffusivities can occur for self-diffusion of organic molecules when the material is solid or a highly viscous semi-solid (Koop et al., 2011). However, in that case the uptake should be lower than expected, not higher as in this study.

4.4.2 Deviations from steady-state

As explained in the previous section, the resistor model can be used to interpret the initial plateau as well as the RH dependence of the long-term uptake at higher RH ($> 60\,\%$). However, its application to data at lower humidities leads to results which are not consistent with measurements with other techniques. Also, it is not clear why the surface reaction should decrease after the first couple of minutes. While one can in principle explain this drop in reaction rate by consumption of the shikimic acid initially present on the surface, the concentration should be constantly replenished in absence of transport limitation. There is no reason to assume transport limitation of shikimic acid at high humidity, and while transport limitation at low humidity might not be unrealistic, it is internally inconsistent with using Eq. 4.14, as it assumes a bulk well-mixed with respect to shikimic acid. There are three additional features of the dataset which cannot be explained with the traditional resistor model approach. The first is the slow decrease of the long-term uptake, which is particularly prominent for the dry experiment. The second is the dependence of the long-term uptake on gas-phase $[O_3]$. If the underlying reaction is reacto-diffusion limited, as implied by the RH dependence, the uptake should not depend on $[O_3]$. The third is the decrease of both the initial plateau and the long-term uptake. Steady-state assumptions are not valid when the uptake changes over time. There is however an analytical expression for the solubility limited uptake and its change with time, which can be used in the resistor-model. In this case, γ is proportional to $t^{-0.5}$, where t is the time (Ammann et al., 2013). A log-log plot of γ vs. t should then have a slope of -0.5. which is clearly not the case for our experimental data. We therefore assume that the region between the initial and the second plateau and the slow decline of the second plateau mark transition regimes, which can not be interpreted with the resistor model. We use a multilayer flux model (KM-SUB) to avoid the limitations of the resistor model and get a more complete understanding of the reaction kinetics.

4.4.3 Model-derived kinetics

The Monte-Carlo genetic algorithm (MCGA) was used to obtain optimized global input parameter sets for KM-SUB which can fit all experimental measurements simultaneously. So far, a global parameter set which would convincingly explain all features in a unique way has not been found. Out of our four MCGA runs so

far, we here show the two optimized parameter sets with the lowest error E: set A with $E = 4.55 \times 10^{-2}$ and set B with $E = 4.38 \times 10^{-2}$. E describes the average square deviation of model γ_{mod} from experimental γ_{exp} and therefore corresponds to R without different weighting of the fits. These two KM-SUB input parameter sets are listed in Table 4.2. Apart from k_{bs,O_3} and $k_{ssb,Y}$, which, as described in Section 4.3.3, are parameterized based on the diffusion constants, two more input parameters from Table 4.1 were not included in the optimization process. As the uptake is not accommodation limited on the timescales we can access experimentally, it is not sensitive to $\alpha_{s,0}$ and τ_d. We therefore choose an $\alpha_{s,0}$ of 0.5 to limit the number of parameters which are optimized and only vary τ_d to obtain a value for $\alpha_{s,0} \cdot \tau_d$ which fits with our experimental data. For D_{g,O_3} we used the value of 0.14 [$cm^2\,s^{-1}$] according to Massman (1998).

Parameter	Unit	MCGA output A	MCGA output B
k^{II}_{BR}	$cm^3\,s^{-1}$	5.94×10^{-19}	6.59×10^{-19}
k^{II}_{SLR}	$cm^2\,s^{-1}$	2.26×10^{-16}	3.39×10^{-16}
f_{kbs,O_3}	$cm\,s^{-1}$	4.86×10^{0}	6.99×10^{-1}
$f_{kssb,Y}$	s^{-1}	1.54×10^{-2}	1.07×10^{-4}
H	$mol\,cm^{-3}\,atm^{-1}$	2.27×10^{-4}	1.47×10^{-4}
K_{bs}	cm	2.98×10^{-9}	3.39×10^{-9}
τ_d	s	1.71×10^{-3}	3.29×10^{-3}
σ_{O_3}	cm^2	1.76×10^{-14}	5.09×10^{-14}
D_{b,O_3} 0 %	$cm^2\,s^{-1}$	9.42×10^{-11}	2.85×10^{-10}
D_{b,O_3} 24 %	$cm^2\,s^{-1}$	1.75×10^{-10}	4.28×10^{-10}
D_{b,O_3} 45 %	$cm^2\,s^{-1}$	3.88×10^{-10}	1.35×10^{-9}
D_{b,O_3} 69 %	$cm^2\,s^{-1}$	3.11×10^{-9}	9.16×10^{-9}
D_{b,O_3} 83 %	$cm^2\,s^{-1}$	1.25×10^{-8}	4.87×10^{-8}
D_{b,O_3} 92 %	$cm^2\,s^{-1}$	7.44×10^{-8}	1.91×10^{-7}
$D_{b,Y}$ 0 %	$cm^2\,s^{-1}$	5.69×10^{-19}	3.49×10^{-22}
$D_{b,Y}$ 24 %	$cm^2\,s^{-1}$	6.47×10^{-19}	2.12×10^{-20}
$D_{b,Y}$ 45 %	$cm^2\,s^{-1}$	2.54×10^{-18}	1.04×10^{-18}
$D_{b,Y}$ 69 %	$cm^2\,s^{-1}$	2.08×10^{-17}	4.69×10^{-18}
$D_{b,Y}$ 83 %	$cm^2\,s^{-1}$	2.72×10^{-14}	3.17×10^{-17}
$D_{b,Y}$ 92 %	$cm^2\,s^{-1}$	9.47×10^{-8}	5.01×10^{-15}

Table 4.2: Globally optimized KM-SUB input parameters

Figure 4.6 shows the KM-SUB results with parameter set A (a) and parameter set B (b) as well as the resistor model from Section 4.4.1 (c) for γ at different RH

and a fixed O_3 concentration of 177-179 ppb in comparison with the experimental data from Figure 4.2. Clearly, the flux model results describe the experimental data better than the resistor model. For both parameter sets, the absolute value of γ_{mod} agrees well with γ_{exp}; the maximum deviation is around a factor of 2. However, the different features of the change of γ_{exp} with time are not captured equally well. Set B seems to better describe γ at higher humidities (92 % and RH 83 %). This is both true for the long-term uptake and the initial plateau. It also captures the initial plateaus at 69 % and 45 %. At lower RH however, the performance is not as good. For 24 % RH and 0 % RH, the initial plateaus end too late and the long-term uptake is too low and its decreasing slope with time is not captured. At these humidities, the experimental data are better described by parameter set A, even though it also has problems with capturing the steep decrease in long-term uptake at 0 %. Set A severely underestimates the initial plateaus at all humidities above 24 %.

In Figure 4.7, the KM-SUB model results with the two different input parameter sets for the dependence of uptake on $[O_3]$ at two RH are compared with experimental data from Figure 4.3. The O_3 dependence of the initial plateau in γ at 92 % RH is better captured by set B, since, as mentioned above, set A does not result in a plateau at high humidities. Set A also overestimates the long term uptake at low concentrations and high RH. It does, however, perform better in capturing the depletion of the film at high concentrations. At low RH, set A gives the better performance. Set B does not capture the O_3 dependence at $> 10^3$ s as all curves converge and a second plateau develops instead of the more constant slopes seen in the experiment.

For the analysis of the different kinetic processes determining the uptake for parameter sets A and B, we have determined parameter sensitivities, shown in Figure 4.8, and the regime classification parameters according to (Berkemeier et al., 2013), shown in Figure 4.9. For both parameter sets, we see in Figure 4.9 that the surface saturation ratio (SSR) is consistently close to one on the timescales where experimental data are available. As SSR describes the ratio of surface O_3 to the concentration at equilibrium in absence of reaction, this means that uptake is not limited by mass transport to the surface (i.e. gas phase diffusion and surface accommodation). Similarly, the bulk saturation ratio (BSR), which is the ratio of the actual O_3 concentration in the first bulk layer to its value at equilibrium in absence of reaction (described by Henry's law), also stays close to one. This indicates that bulk accommodation is not a limiting process. From the time-

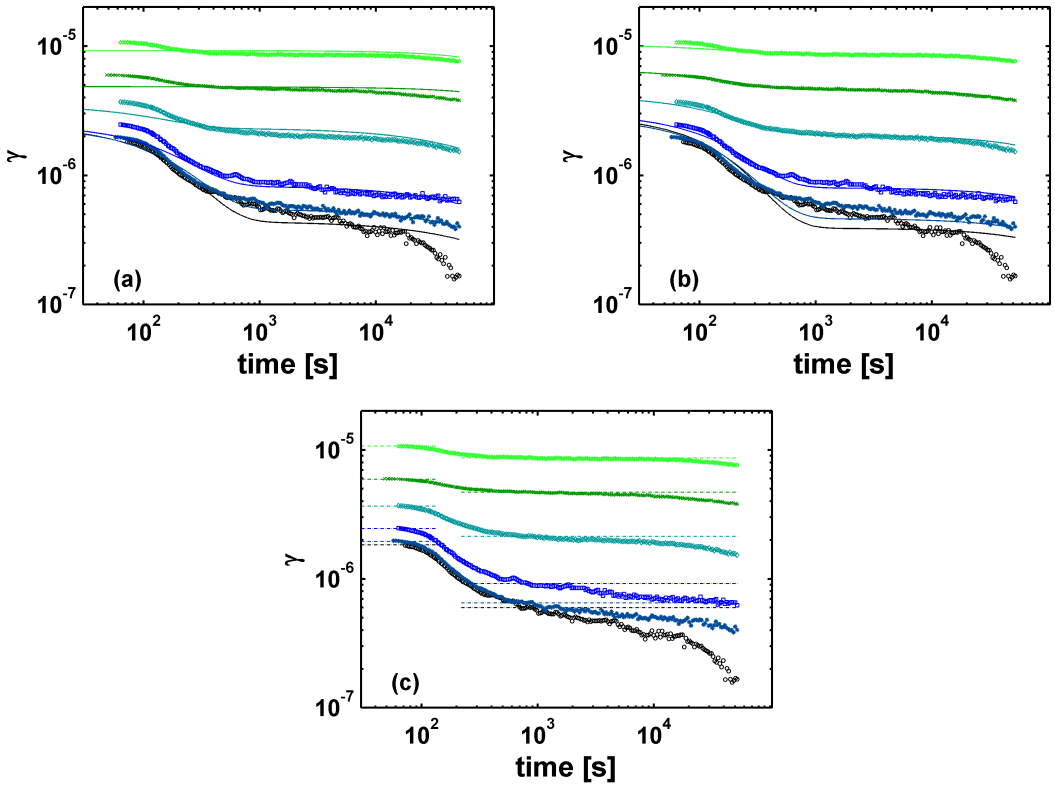

Figure 4.6: KM-SUB fits to the experiments at different RH and a fixed O_3 concentration of 177-179 ppb, using the global KM-SUB input parameter sets A (a) and B (b) and the resistor model from Section 4.4.1 for comparison (c). See Table 4.2 for a list of the parameters and assigned values. From the bottom up, the humidities are: 0 % RH (black), 24 % RH (dark blue), 45 % RH (blue), 69 % RH (dark cyan), 83 % RH (green) and 92 % RH (bright green).

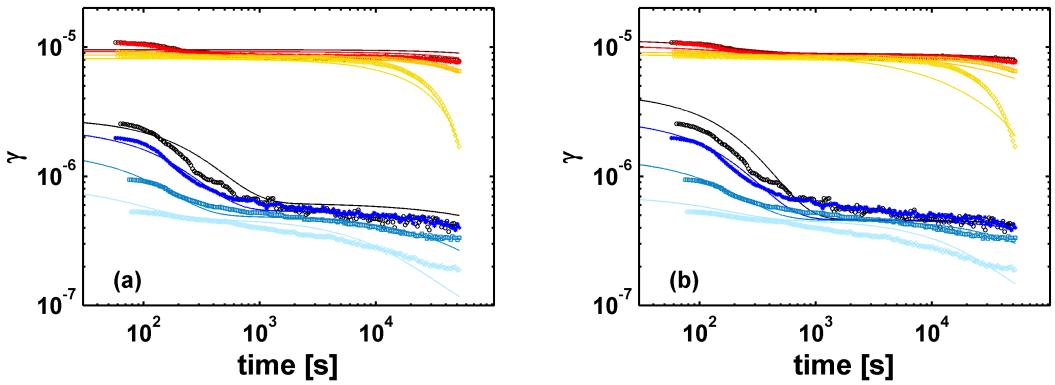

Figure 4.7: KM-SUB fits to measurements at different gas-phase O_3 for two different RH, using the global KM-SUB input parameter sets A (a) and B (b). See Table 4.2 for a list of the parameters and assigned values. The lower four sets where measured at 24 % RH (89-90 ppb (black), 177-179 ppb (blue) 495-496 ppb (dark cyan), 1984-1985 ppb (light blue)), the upper four at 92 % RH (89-90 ppb (dark red), 177-179 ppb (red) 495-496 ppb (orange), 1984-1985 ppb (yellow)).

dependence of the surface to total loss rate ratio (STLR), we can conclude that the formation of an initial plateau occurs if the O_3-loss due to surface reaction decreases abruptly. This is again consistent with the results from the steady-state evaluation. Such decrease can be seen for all cases except the two highest RH modeled with set A, which fits with the fact that no plateau appeared in the corresponding model calculation. The sharp decrease in STLR coincides with a decrease in the surface mixing parameter of Y, SMP_Y. SMP_Y describes the ratio of the actual surface concentration of Y to the maximal possible surface concentration given by $[Y]_{bn} \cdot \delta_Y$, where $[Y]_{bn}$ is the current concentration of Y in the lowest bulk layer and δ_Y a geometric factor to relate the molecular volume concentration to a molecular area concentration. The decrease in SMP_Y therefore indicates limitation of mass transport of Y from the bulk to the surface, as seen at 0-69 % RH for set A and at all humidities for set B. This coincides with a rise in sensitivity of $f_{kssb,Y}$ and $D_{b,Y}$ for parameter set A at 0-69 % RH. The fact that the decrease in SMP_Y correlates with the presence of an initial plateau in turn indicates that the model can only explain the plateau if it introduces a transport limitation for shikimic acid from the bulk to the surface. At higher humidities, the bulk becomes more well-mixed in Y for set A, which can be inferred from SMP_Y staying constantly around one and the concentration profiles shown in Figure 4.10.

We also see an increase in BMP_X and BMP_{XY} at high RH. BMP_X is the bulk mixing parameter for O_3. It is defined as $l_{O_3} / \left(l_{O_3} + r_p / e \right)$, where l_{O_3} is the reacto-

diffusive length (Eq. 4.15) and r_p the film thickness. The increasing value of BMP_X therefore indicates that the bulk becomes more well-mixed with regards to O_3. BMP_Y (not shown in Figure 4.9) accordingly is the bulk mixing parameter for shikimic acid, defined as $l_Y/\left(l_Y + r_p/e\right)$. BMP_{XY} is the average of the bulk mixing parameters for O_3 and shikimic acid. If BMP_{XY} approaches unity, O_3 and shikimic acid are well-mixed throughout the particle and the system falls within the reaction-limited bulk reaction case described by Eq. 4.13. If BMP_{XY} approaches zero, strong gradients in both O_3 and shikimic acid limit the loss rate and the system falls within the bulk diffusion-limited bulk reaction case defined according to Berkemeier et al. (2013). For intermediate BMP_{XY} with low BMP_X, the system is well-mixed in shikimic acid and therefore a traditional reacto-diffusion limited case which can be described with Eq. 4.14. At 92 % RH, set A predicts such a classic, reacto-diffusive case in terms of the bulk reaction. It should be noted that while the surface reaction sharply decreases for 0 % RH to 69 % RH and is generally low for 83 % RH and 92 % RH, the STLR never drops to 0. This is likely the cause of the O_3 dependence in γ_{mod}, which can be seen over all timescales for set A. Set B shows a sharp drop in STLR combined with a decrease of SMP_Y even at high RH.

As seen in Table 4.2, $D_{b,Y}$ and $f_{kssb,Y}$ are lower than for set A. Given that $D_{b,Y}$ is 5.01×10^{-15} $cm^2\,s^{-1}$ even at 92 % RH, it seems unlikely that set B is a realistic choice to describe the experiments as Stokes-Einstein should be valid in this range. This is corroborated by the fact that Figure 4.10 shows formation of a gradient in Y at 83 % RH, which was not observed in the STXM measurements. However, while set A shows a more realistic value for $D_{b,Y}$ at 92 % RH, the sharp drop to 2.72×10^{-14} $cm^2\,s^{-1}$ at 83 % RH also seems too strong. Obviously, reasonably good fits to the experimental data are only obtained if diffusion of Y is becoming a sufficiently limiting parameter. As mentioned in the context of the steady state analysis, this is the case at around 2×10^{-15} $cm^2\,s^{-1}$ for a film thickness of 190 nm (0 % RH) and 1×10^{-14} $cm^2\,s^{-1}$ for a film thickness of 470 nm (92 % RH). This agrees well with the $D_{b,Y}$ values found by the two KM-SUB fits, but is not realistic at such high humidities. Set A and B have similar values of D_{b,O_3}. Comparison with values determined from steady-state evaluation of the CWFT data, STXM measurements and EDB measurements is shown in Figure 4.11. While the overall order of magnitude agrees fairly well, D_{b,O_3} is too large at low RH compared to D_{H_2O} determined with the EDB, and too small at high RH. The latter could be due to the low values for k_{BR}^{II} obtained via the MCGA.

The fact that no global parameter set which would convincingly explain all features could be found so far and the fact that the current solutions include unrealistic parameters show that the model is still not properly constrained. There are several additional constraints one could apply. Setting H to the fixed value of O_3 in water might change the problem of the low values for k_{BR}^{II} and D_{b,O_3}. D_{b,O_3} could be further constrained by coupling it with a constant to the values of D_{b,H_2O} measured with the EDB and fitting this constant instead of varying D_{b,O_3} freely. Trying to constrain $D_{b,Y}$ in a similar way would be more problematic, as shikimic acid is not a small guest molecule but the main component of the matrix and therefore bound to change differently with increasing viscosity, so that the factor could not be constant. One could however set a minimum for $D_{b,Y}$ at high RH based on D_{b,H_2O}, as deviation from Stokes-Einstein should be low, or further limit the range in which $D_{b,Y}$ is varied at the different humidities. The unrealistically low values for $D_{b,Y}$ needed to achieve the initial plateaus might be compensated by relaxing the constraint that $f_{kssb,Y}$ is not RH dependent. If surface to bulk transport can be influenced by factors such as surface tension and viscosity, $f_{kssb,Y}$ would indeed be RH dependent and should be varied for each RH.

In addition to the question of constraints on parameters and parameter ranges, two basic features of the KM-SUB model and the MCGA fitting procedure might contribute to the problem in finding a good fit. Regarding KM-SUB, there remains a problem with how to handle the transport of molecules in the limit of molecular scale transport processes. When the reacto-diffusive length is smaller than the layer thickness, depletion happens layer-wise due to the compartmentalization of the model. This can be counteracted by decreasing the layer thickness. However, using the continuum process diffusion to describe the transport might not be valid any more when the layer thickness approaches molecular scale. Regarding the MCGA, there remains the open question of whether the current least-square method really gives the best estimate of fit quality, as the change of γ in time (i.e. the progression of the slopes) might be considered just as or even more important than the absolute values. It of course also remains a possibility that the current version of the KM-SUB model simply does not represent all processes necessary to describe the system. The current model only allows for a surface reaction and a bulk reaction of O_3 and shikimic acid. Other reactions, such as e.g. a self-reaction of O_3 on the surface, are not considered. The change in properties over time is currently also not considered. While experimental variables such as [Y] are tracked over time, the model input parameters in Table 4.1 are considered constant, even

though it is known that e.g. viscosity can change with formation of reaction products. However, due to the current lack of knowledge about these processes, an implementation of such features into KM-SUB would at this time be premature and lead to arbitrary results.

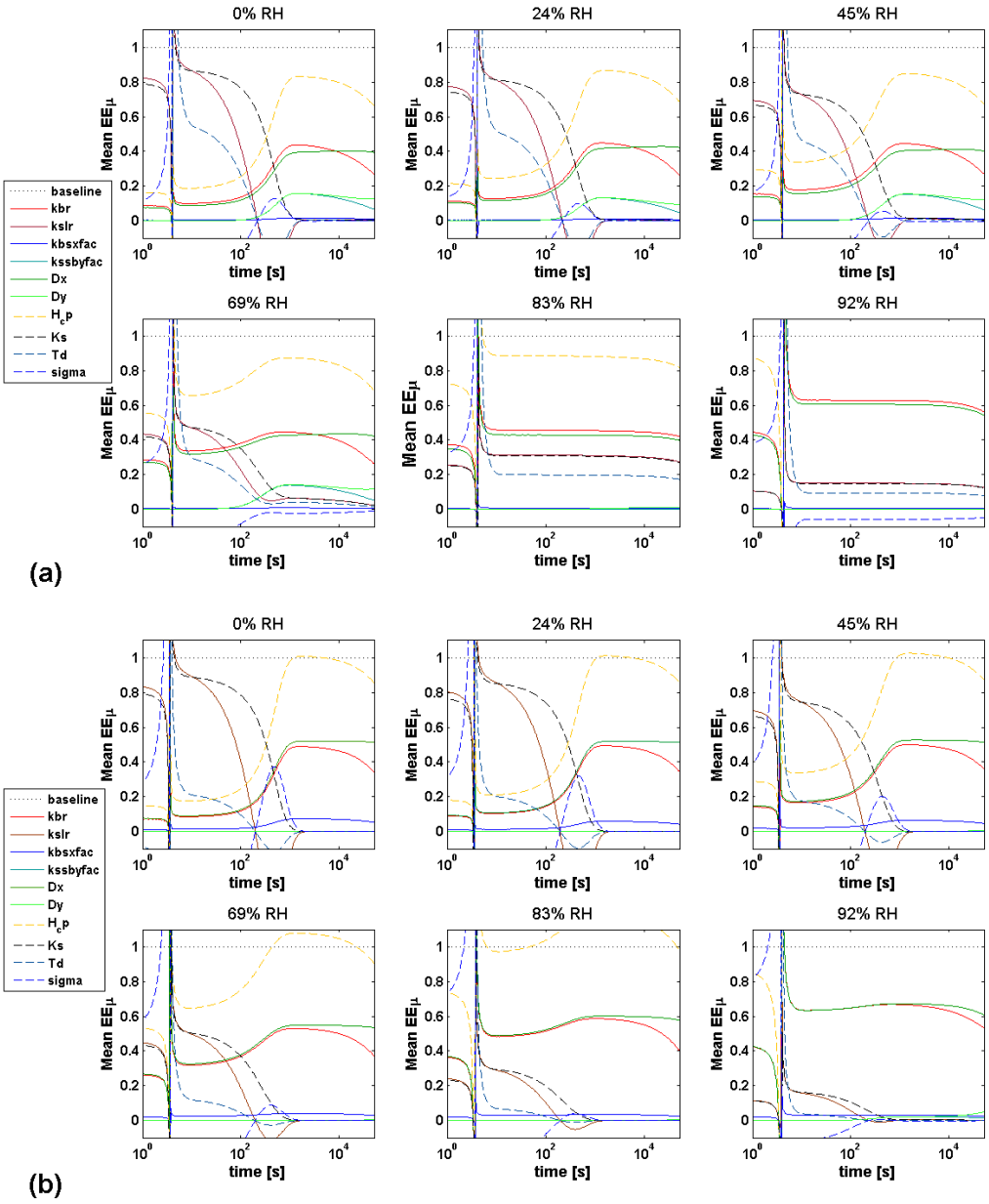

Figure 4.8: Sensitivity analysis of the KM-SUB input parameters for parameter set A (a) and B (b). A list of the parameters and their descriptions can be found in Table 4.1.

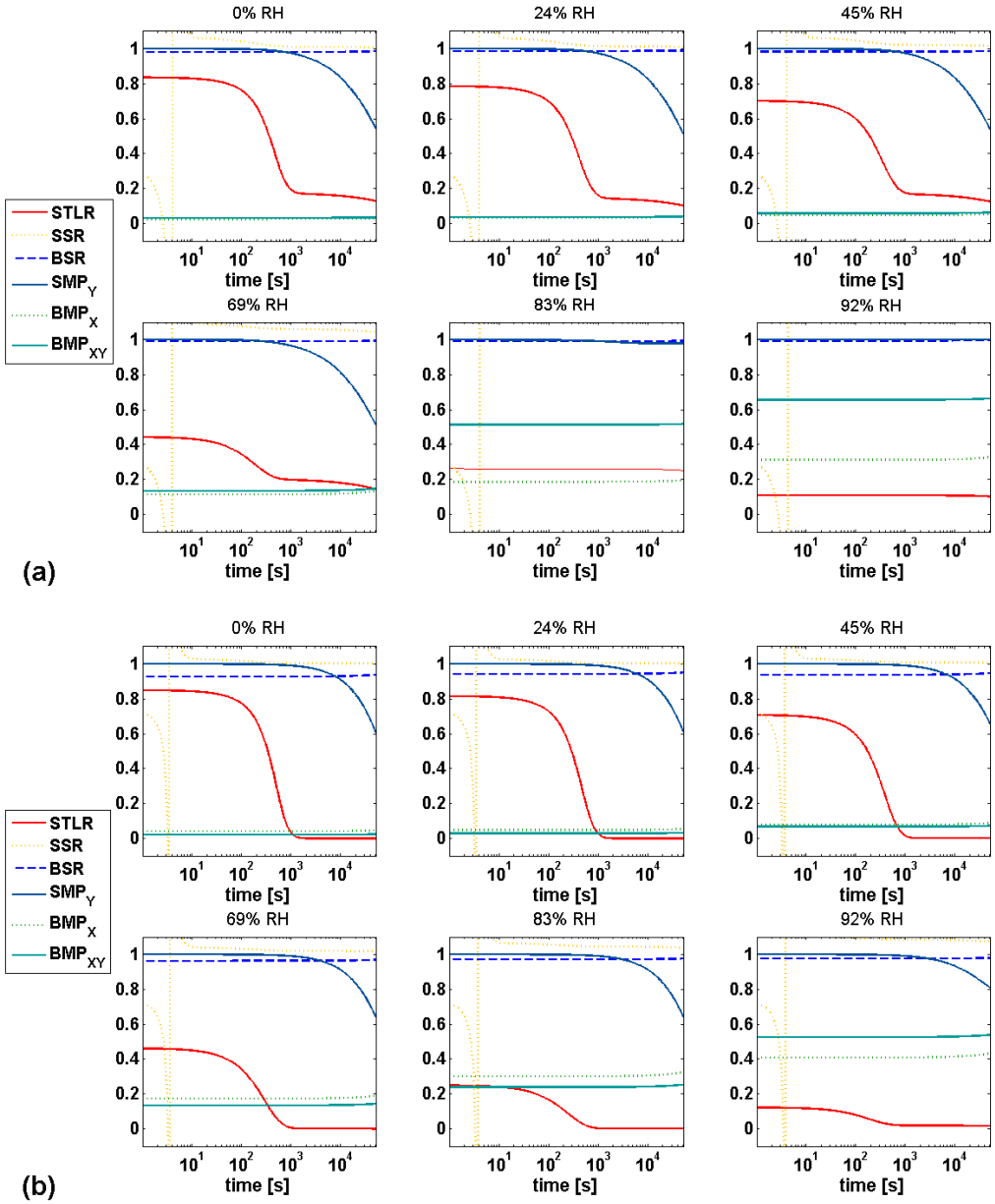

Figure 4.9: Classification parameters for global KM-SUB input parameter set A (a) and B (b) according to Berkemeier et al. (2013). STLRL=surface to total loss rate ratio, SSR=normalized surface saturation ratio, BSR=normalized bulk saturation ratio, SMP_Y=normalized surface mixing parameter, BMP_X=normalized bulk mixing parameter in X, BMP_{XY}=normalized bulk mixing parameter in X and Y.

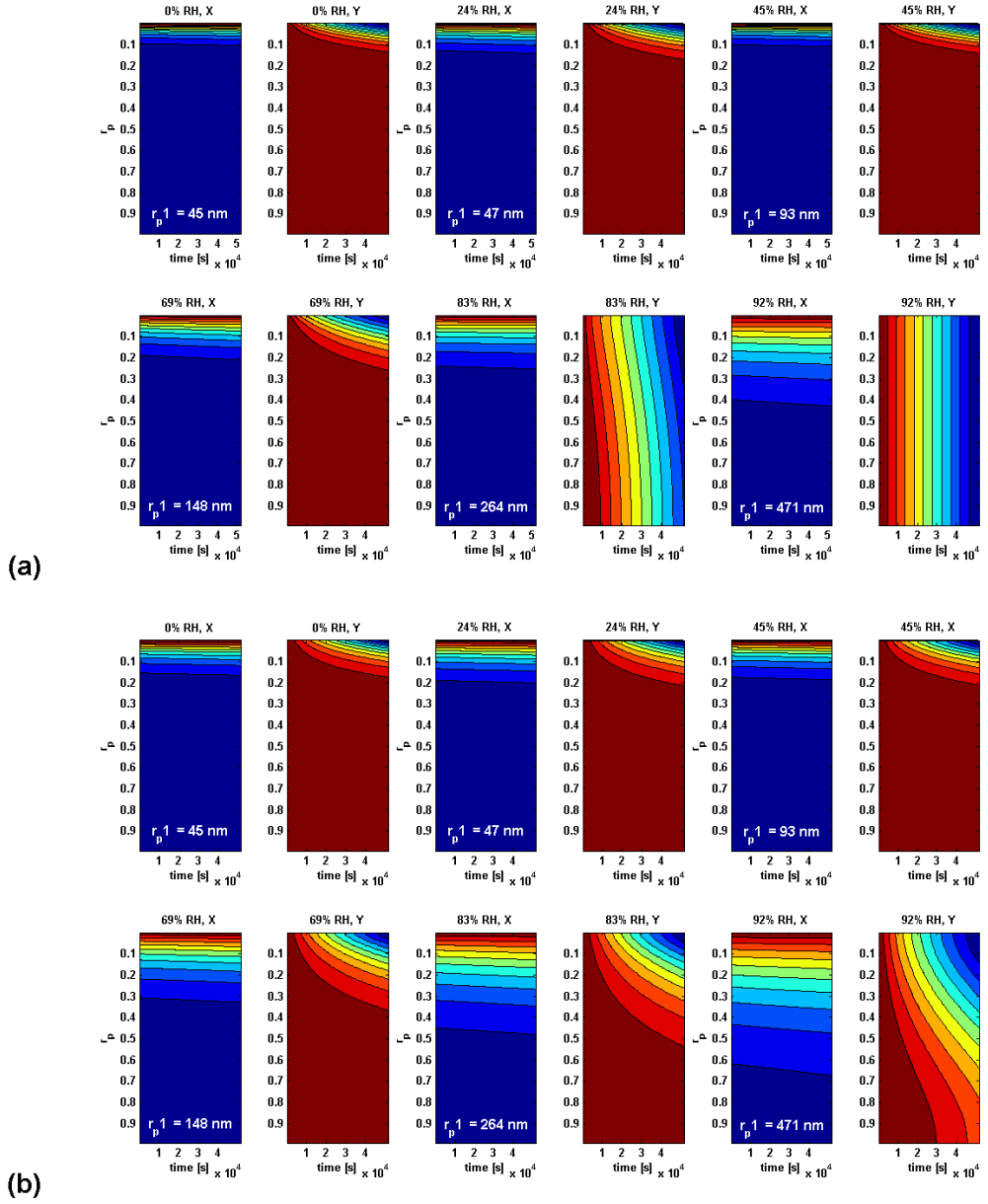

Figure 4.10: Concentration gradients. r_p is the relative penetration depth where $r_p = 0$ marks the particle surface.

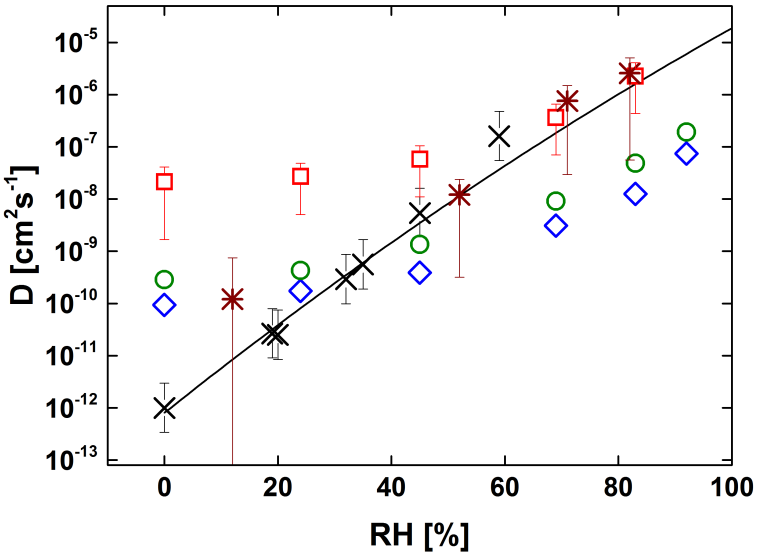

Figure 4.11: Comparison of diffusion coefficients. O_3 diffusion coefficients from flow tube measurements (295.7 K), evaluated with a resistor model approach (red squares) and two different KM-SUB parameter sets (A, blue diamonds, B, green circles), as well as from STXM measurements (298 K, dark red asterisks). H_2O diffusion coefficients from EDB measurements (293.5 K, measured data: black crosses, parameterization: black line).

4.5 Conclusions

The ozonolysis of shikimic acid was measured for several O_3 concentrations (89 ppb-1985 ppb) and humidities (0 %-92 %) for over 14 h. The data was analyzed by both steady-state analysis and the kinetic flux model KM-SUB. Analysis with the resistor model suggests a Langmuir-Hinshelwood-type surface reaction running parallel to a bulk reaction for the first few minutes of the experiment, after which the bulk reaction dominates. Uptake due to surface reaction remains similar when passing from the aqueous solution at 92 % RH to the semi-solid or solid material at 24 % RH. The lower limit for $k^{\mathrm{I}}_{\mathrm{SLR}}$ is 1.5×10^{-4} s^{-1}. The lower limit for K_{LH} is 3×10^{-13} cm^3 molecule^{-1}, which compares well with K_{LH}-values for ozonolysis of PAHs. The uptake is best described by reaction limitation at 92 % RH and reacto-diffusive limitation below 92 % RH. The second order rate constant was determined from the measurements at 92 % RH. Its value of $(1.5 \pm ^{1.5}_{0.5}) \times 10^3$ L mol^{-1} s^{-1} is consistent with the one determined from STXM experiments (Chapter 3/Steimer et al., 2014). The uptake increased by more than one order of magnitude upon humidification from 0 % to 92 % RH. This trend of increasing uptake with increasing

humidity is again consistent with the results from the STXM measurements. The steady state analysis reveals deficiencies in explaining the humidity dependent γ after long exposure times when attributed to reacto-diffusive regime. Additionally, the diffusion constants for O_3 are too high at low humidity, providing further evidence that the analytical expression for reacto-diffusive limitation does not adequately describe the system. Optimization of KM-SUB yielded two global input parameter sets which fit the experimental data with similar quality. In both cases, the model indicates that a surface reaction is present, confirming the results of the steady-state evaluation. Furthermore, with both parameter sets the model reproduces the general trend of decreasing reactivity with decreasing humidity. Finally, both KM-SUB parameter sets consistently infer that $D_{b,Y}$ is largely responsible for the general dependence of reactivity on humidity and low $D_{b,Y}$ is needed to generate the initial plateau from the surface reaction. This is due to convolution of diffusion and reaction of O_3 and shikimic acid in the same region. However, both $D_{b,Y}$ and D_{b,O_3} are too low at high RH to be realistic. While the availability of the current measurements, which explore a broad range of conditions, imposes heavy constraints on the numerical model, still, several global parameter sets provide similarly good fits to the experimental data. Yet, so far none of these simulations could globally reproduce all significant features of the experimental data. A better set might still be found by changing the constraints or prolonging the running time of the MCGA for increased optimization.

Acknowledgements

We acknowledge support by the Swiss National Science Foundation (grant no. 130175) and the EU FP7 project PEGASOS. We thank M. Birrer for technical support and C. Marcolli and U. Krieger for helpful discussions. F. Vivian ran preliminary experiments on the temperature dependence of the O_3 uptake. A. J. Huisman suggested shikimic acid as a possible proxy for glass-forming organic matter.

Bibliography

Abramson, E., Imre, D., Beranek, J., Wilson, J., and Zelenyuk, A.: Experimental determination of chemical diffusion within secondary organic aerosol particles, *Phys. Chem. Chem. Phys.*, **15**, 2983–2991, 2013.

Ammann, M., Pöschl, U., and Rudich, Y.: Effects of reversible adsorption and Langmuir-Hinshelwood surface reactions on gas uptake by atmospheric particles, *Phys. Chem. Chem. Phys.*, **5**, 351–356, 2003.

Ammann, M., Cox, R. A., Crowley, J. N., Jenkin, M. E., Mellouki, A., Rossi, M. J., Troe, J., Wallington, T. J.: Evaluated kinetic and photochemical data for atmospheric chemistry: Volume VI - heterogeneous reactions with liquid substrates, *Atmos. Chem. Phys.*, **13**, 8045–8228, 2013.

Berkemeier, T., Huisman, A. J., Ammann, M., Shiraiwa, M., Koop, T., and Pöschl, U.: Kinetic regimes and limiting cases of gas uptake and heterogeneous reactions in atmospheric aerosols and clouds: a general classification scheme, *Atmos. Chem. Phys.*, **13**, 6663–6686, 2013.

Biń, A. K.: Ozone solubility in liquids, *Ozone-Sci. Eng.*, **28**, 67–75, 2006.

Bones, D. L., Henricksen, D. K., Mang, S. A., Gonsior, M., Bateman, A. P., Nguyen, T. B., Cooper, W. J., and Nizkorodov, S. A.: Appearance of strong absorbers and fluorophores in limonene-O_3 secondary organic aerosol due to NH_4^+-mediated chemical aging over long time scales, *J. Geophys. Res. Atmos.*, **115**, D05203, 2010.

Cappa, C. D., and Wilson, K. R.: Evolution of organic aerosol mass spectra upon heating: implications for OA phase and partitioning behavior, *Atmos. Chem. Phys.*, **11**, 1895–1911,

2011.

Cooney, D. O., Kim, S.-S., and Davis, E. J.: Analyses of mass transfer in hemodialyzers for laminar blood flow and homogeneous dialysate, *Chem. Eng. Sci.*, **29**, 1731–1738, 1974.

Criegee, R.: Mechanism of ozonolysis, *Angew. Chem. Int. Edit.*, **14**, 745–752, 1975.

Crowley, J. N., Ammann, M., Cox, R. A., Hynes, R. G., Jenkin, M. E., Mellouki, A., Rossi, M. J., Troe, J., and Wallington, T. J.: Evaluated kinetic and photochemical data for atmospheric chemistry: Volume V - heterogeneous reactions on solid substrates, *Atmos. Chem. Phys.*, **10**, 9059–9223, 2010.

Hoigné, J. and Bader, H.: Rate constants of reactions of ozone with organic and inorganic compounds in water-II: Dissociating organic compounds, *Water Res.*, **17**, 185–194, 1983.

Kanakidou, M., Seinfeld, J. H., Pandis, S. N., Barnes, I., Dentener, F. J., Facchini, M. C., Van Dingenen, R., Ervens, B., Nenes, A., Nielsen, C. J., Swietlicki, E., Putaud, J. P., Balkanski, Y., Fuzzi, S., Horth, J., Moortgat, G. K., Winterhalter, R., Myhre, C. E. L., Tsigaridis, K., Vignati, E., Stephanou, E. G., and Wilson, J.: Organic aerosol and global climate modelling: a review, *Atmos. Chem. Phys.*, **5**, 1053–1123, 2005.

Koop, T., Bookhold, J., Shiraiwa, M., and Pöschl, U.: Glass transition and phase state of organic compounds: dependency on molecular properties and implications for secondary organic aerosols in the atmosphere, *Phys. Chem. Chem. Phys.*, **13**, 19238–19255, 2011.

Kuwata, M. and Martin, S. T.: Phase of atmospheric secondary organic material affects its reactivity, *P. Natl. Acad. Sci. USA*, **109**, 17354–17359, 2012.

Kwamena, N.-O., A., Thornton, J. A., and Abbatt, J. P. D.: Kinetics of Surface-Bound Benzo[a]pyrene and Ozone on Solid Organic and Salt Aerosols, *J. Phys. Chem. A*, **108**, 11626–11634, 2004.

Kwamena, N. O. A., Staikova, M. G., Donaldson, D. J., George, I. J., and Abbatt, J. P. D.: Role of the aerosol substrate in the heterogeneous ozonation reactions of surface-bound PAHs, , *J. Phys. Chem. A*, **111**, 11050–11058, 2007.

Loza, C. L., Coggon, M. M., Nguyen, T. B., Zuend, A., Flagan, R. C., and Seinfeld, J. H.: On the Mixing and Evaporation of Secondary Organic Aerosol Components, *Environ. Sci. Technol.*, **47**, 6173–6180, 2013.

Massman, W. J.: A review of the molecular diffusivities of H_2O, CO_2, CH_4, CO, O_3, SO_2, NH_3, N_2O, NO, AND NO_2 in air, O_2 and N_2 near STP, *Atmos. Environ.*, **32**, 1111–1127, 1998.

Medeiros, P. M. and Simoneit, B. R. T.: Source Profiles of Organic Compounds Emitted upon Combustion of Green Vegetation from Temperate Climate Forests, *Environ. Sci. Technol.*, **42**, 8310–-8316, 2008.

Murphy, D. M., and Fahey, D. W.: Mathematical Treatment of the Wall Loss of a Trace Species in Denuder and Catalytic-Converter Tubes, *Anal. Chem.*, **59**, 2753–2759, 1987.

Odum, J. R., Hoffmann, T., Bowman, F., Collins, D., Flagan, R. C., and Seinfeld, J. H.: Gas/particle partitioning and secondary organic aerosol yields, *Environ. Sci. Technol.*, **30**, 2580–2585, 1996.

Pankow, J. F.: An Absorption-Model of the Gas Aerosol Partitioning Involved in the Formation of Secondary Organic Aerosol, *Atmos. Environ.*, **28**, 189–193, 1994.

Perraud, V., Bruns, E. A., Ezell, M. J., Johnson, S. N., Yu, Y., Alexander, M. L., Zelenyuk, A., Imre, D., Chang, W. L., Dabdub, D., Pankow, J. F., and Finlayson-Pitts, B. J.: Nonequilibrium atmospheric secondary organic aerosol formation and growth, *P. Natl. Acad. Sci. USA*, **109**, 2836–2841, 2012.

Pöschl, U., Letzel, T. Schauer, C., and Niessner, R.: Interaction of ozone and water vapor with spark discharge soot aerosol particles coated with benzo[a]pyrene: O_3 and H_2O adsorption, benzo[a]pyrene degradation, and atmospheric implications, *J. Phys. Chem. A*, **105**, 4029–4041, 2001.

Pöschl, U., Rudich, Y., and Ammann, M.: Kinetic model framework for aerosol and cloud surface chemistry and gas-particle interactions - Part 1: General equations, parameters, and terminology, *Atmos. Chem. Phys.*, **7**, 5989–6023, 2007.

Razumovskii, S. D. and Zaikov, G. E.: Kinetics and mechanism of ozone reactions with dual reactivity points, *Usp. Khim.*+, **49**, 2344–2376, 1980.

Renbaum-Wolff, L., Grayson, J. W., Bateman, A. P., Kuwata, M., Sellier, M. Murray, B. J., Shilling, J. E., Martin, S. T., and Bertram, A. K.: Viscosity of α-pinene secondary organic material and implications for particle growth and reactivity, *P. Natl. Acad. Sci. USA*, **110**, 8014–8019, 2013.

Segal-Rosenheimer, M., and Dubowski, Y.: Heterogeneous Ozonolysis of Cypermethrin Using Real-Time Monitoring FTIR Techniques, *J. Phys. Chem. C*, **111**, 11682–11691, 2007.

Shiraiwa, M., Pfrang, C., and Pöschl, U.: Kinetic multi-layer model of aerosol surface and bulk chemistry (KM-SUB): the influence of interfacial transport and bulk diffusion on the oxidation of oleic acid by ozone, *Atmos. Chem. Phys.*, **10**, 3673–3691, 2010.

Shiraiwa, M., Ammann, M., Koop, T., and Pöschl, U.: Gas uptake and chemical aging of semisolid organic aerosol particles, *P. Natl. Acad. Sci. USA*, **108**, 11003–11008, 2011.

Steimer, S. S., Lampimäki, M., Coz, E., Grzinic, G., and Ammann, M.: The influence of physical state on shikimic acid ozonolysis: a case for in situ microspectroscopy, *Atmos. Chem. Phys.*, **14**, 10761–10772, 2014.

Steimer, S. S., Krieger, U. K., Te, Y.-F., Lienhard, D. M., Huisman, A. J., Ammann, M., and Peter, T.: Electrodynamic balance measurements of thermodynamic, kinetic, and optical aerosol properties inaccessible to bulk methods, *Atmos. Meas. Tech. Discuss.*, **8**, 689-719, 2015.

Utter, R. G., Burkholder, J. B., Howard, C. J., and Ravishankara, A. R.: Measurement of the mass accommodation coefficient of ozone on aqueous surfaces, *J. Phys. Chem.-US*, **96**, 4973–4979, 1992.

Vaden, T. D., Imre, D., Beranek, J., Shrivastava, M., and Zelenyuk, A.: Evaporation kinetics and phase of laboratory and ambient secondary organic aerosol, *P. Natl. Acad. Sci. USA*, **108**, 2190–2195, 2011.

Vesna, O., Sjogren, S., Weingartner, E., Samburova, V., Kalberer, M., Gäggeler, H. W., and Ammann, M.: Changes of fatty acid aerosol hygroscopicity induced by ozonolysis under humid conditions, *Atmos. Chem. Phys.*, **8**, 4683–4690. 2008.

Virtanen, A., Joutsensaari, J., Koop, T., Kannosto, J., Yli-Pirilä, P., Leskinen, J., Mäkelä, J. M., Holopainen, J. K., Pöschl, U., Kulmala, M., Worsnop, D. R., and Laaksonen, A.: An amorphous solid state of biogenic secondary organic aerosol particles, *Nature*, **467**, 824–827, 2010.

Zahardis, J. and Petrucci, G. A.: The oleic acid-ozone heterogeneous reaction system: products, kinetics, secondary chemistry, and atmospheric implications of a model system – a review, *Atmos. Chem. Phys.*, **7**, 1237–1274, 2007.

Zhang, Q., Jimenez, J. L., Canagaratna, M. R., Allan, J. D., Coe, H., Ulbrich, I., Alfarra, M. R., Takami, A., Middlebrook, A. M., Sun, Y. L., Dzepina, K., Dunlea, E., Docherty, K., DeCarlo, P. F., Salcedo, D., Onasch, T., Jayne, J. T., Miyoshi, T., Shimono, A., Hatakeyama, S., Takegawa, N., Kondo, Y., Schneider, J., Drewnick, F., Borrmann, S., Weimer, S., Demerjian, K., Williams, P., Bower, K., Bahreini, R., Cottrell, L., Griffin, R. J., Rautiainen, J., Sun, J. Y., Zhang, Y. M., and Worsnop, D. R.: Ubiquity and dominance of oxygenated species in organic aerosols in anthropogenically-influenced Northern Hemisphere midlatitudes, *Geophys. Res. Lett.*, **34**, L13801, 2007.

Zhou, S., Shiraiwa, M., McWhinney, R. D., Pöschl, U., and Abbatt, J. P. D.: Kinetic limitations in gas-particle reactions arising from slow diffusion in secondary organic aerosol, *Faraday Discuss.*, **165**, 391–406, 2013.

CHAPTER 5

Summary & Outlook

This work provides an in depth analysis of the reaction kinetics of the shikimic acid/O_3/water system. The key question of this thesis is: *How are the reaction kinetics influenced by changes in viscosity?* To answer this question, we took a multi-technique approach to investigate the system from various angles.
Atmospheric particles containing only inorganic compounds are usually aqueous solutions or, more rarely, crystalline upon efflorescence. For particles without any organic content, viscosity therefore changes abruptly over several orders of magnitude from very high to very low. In the first case, bulk reactions can usually be neglected, in the latter they can be treated as well-mixed. This is different for organic matter, where viscosities can continuously change over several orders of magnitude as the material turns from liquid to semi-solid and finally glassy. In the atmosphere, temperature and humidity are the main driving variables for these changes. Diffusivity decreases as viscosity increases. This is bound to lead to concentration gradients within the condensed phase, which in turn affect the reaction rates. Our goal was to understand the fundamental processes underlying this phenomenon to provide a generalized description of the kinetics.
Our model compound for the bulk reactant is shikimic acid, a carboxylic acid with a single carbon-carbon double bond. The majority of studies on alkene ozonolysis

in atmospheric particles use oleic acid as a proxy. However, oleic acid is insoluble in water, making it an poor proxy for the large fraction of organic carbon which is water soluble. We therefore suggest shikimic acid as an alternative in cases where the scientific question relates to water soluble organic carbon.

As we used water as a plasticizer, it was important to first characterize the influence of water on the physical properties of shikimic acid. We therefore conducted measurements on single, levitated shikimic acid particles in an electrodynamic balance. These measurements provide thermodynamic and kinetic physical data to describe the microphysics of the shikimc acid-water system. We obtained parametrizations for density and mass fraction of solute as a function of humidity. With this data, one can calculate e.g. film thickness and shikimic acid concentration in solution at a specific humidity. Additionally, we confirmed that shikimic acid does not crystallize upon drying, but forms an amorphous solid. This is accompanied by a decrease in the diffusion coefficients of water over several orders of magnitude from 1.9×10^{-9} $\mathrm{m^2\,s^{-1}}$ to about 1×10^{-16} $\mathrm{m^2\,s^{-1}}$. This knowledge about the microphysics then provided the foundation for investigating the reaction kinetics with scanning transmission X-ray microscopy combined with near-edge X-ray absorption fine structure spectroscopy and coated wall flow tube experiments.

Scanning transmission X-ray microscopy combined with near-edge X-ray absorption fine structure spectroscopy provides the means to obtain spatially resolved chemical information with a resolution < 20 nm. It can therefore in principle be used to directly observe gradients of the bulk phase reactant, which were previously implied from fitting a flux model to experimental data of O_3 uptake on a protein (Shiraiwa et al., 2011). We successfully showed that the technique can be applied to measure the reaction of a proxy for environmentally relevant condensed matter *in situ*. We were able to directly follow the degradation of single shikimic acid particles. We did not detect any gradients even at low humidity, a fact ascribed to any potential gradients at low RH being below the resolution of the microscope. In the flow tube experiments, we followed the reaction via the loss of gas phase ozone. In both cases, we found a clear trend of decreasing reaction rate as humidity decreased and the material became more solid. We extracted second order reaction rate constants for the bulk reaction from the measurements at the highest humidity, 83 % or 92 % respectively. The rates of $(3 \pm 1.8) \times 10^3$ $\mathrm{L\,mol^{-1}\,s^{-1}}$ (X-ray microscopy) and $(1.5 \pm {}^{1.5}_{0.5}) \times 10^3$ $\mathrm{L\,mol^{-1}\,s^{-1}}$ (flow tube) are in good agreement. We found that the X-ray microscopy measurements are well described by the traditional reacto-diffusive regime, which captures the humidity dependence

of γ and results in diffusion coefficients for O_3 which are similar to those of water measured with the electrodynamic balance. However, analysis of the data obtained by coated wall flow tube measurements revealed that traditional reacto-diffusive limitation alone can not describe all features of the O_3 uptake. The dependence of the initial uptake on O_3 could be ascribed to a surface reaction in a way still consistent with the presence of reacto-diffusive limitation by using the resistor-model approach. However, other features could not be explained and the obtained diffusion constants are inconsistent with the ones obtained from the microspectroscopy and electrodynamic balance measurements.

We therefore used a uniformly-sampled Monte-Carlo search combined with a genetic algorithm to optimize fits derived from the kinetic flux model KM-SUB to our measured uptake coefficients. With this approach, we search for a global set of input parameters, which can fit all data simultaneously without changes in parameters which should be constant between measurements. The general trend of reactivity with relative humidity was captured well, but just as with the resistor-model approach, none of the fits managed to correctly reproduce all features of the measured uptake and some results contradict findings from the microspectroscopy experiments. While this is, of course, not a satisfying end result, it demonstrates that large datasets over long timescales and the constraints on model parameters obtained from measurements with additional experimental techniques can significantly reduce the arbitrariness of the fits as the model is no longer underdetermined. The observations from additional measurements may also not only help to constrain the input parameters, but also help in determining how realistic a resulting fit is. One example for this is the wide shikimic acid concentration gradient which was predicted by one of the model runs at intermediate humidity, but not observed with microspectroscopy.

The discrepancy between fit and experimental results could be due to either flaws in the representation of physical and chemical processes in the model or reasons such as problems with the fit optimization procedure, poor choice of constraints, or uncertainties of the experiments. As fit quality is judged based on the features of the O_3 uptake measured in our flow tube experiments, it is extremely important that the measurements are both accurate and precise. We have optimized our flow tube measurements in terms of film production and experimental setup, and achieved high reproducibility of the measured uptake. One source of uncertainty is the long-term stability of the environmental conditions, such as temperature, dew point, and O_3 concentration. The main issue here is the stability of the O_3 source,

which influences the long term uptake. Apart from variation of the environmental conditions, inhomogeneities in the film might introduce some error. This is particularly likely at low humidities, where cracks might form in a solid film, as they would increase the available surface area compared to the calculated one and lead to uncertainties in the characterization of the surface reaction in particular.

We have already used three different techniques with different observables (O_3 loss, shikimic acid degradation and particle growth) to constrain the KM-SUB model. There are however several additional experiments which could provide constraints on the input variables or provide additional information to judge the scenarios provided by the model output. Measurements in diluted shikimic acid solution could be used to determine the second order rate constant with higher accuracy and use it as input for the model. As there is a lot of uncertainty regarding the surface reaction, it would also be useful to investigate the system with a surface-sensitive technique, such as high-pressure X-ray photoemission spectroscopy or near-edge X-ray absorption fine structure spectroscopy with electron-yield detection. We have measured the diffusion of water in shikimic acid to compare the obtained values with the model output and potentially use them as a constraint on the input parameters regarding the O_3 diffusion. Just as in the study of Shiraiwa et al. (2011), we found the model output also suggests very low diffusion of the bulk material to explain the measured uptake. While values of $D_{b,Y} \leq 10^{-17} cm^2 s^{-1}$ at 50 % RH might be realistic for the self-diffusion of a bulky protein, the obtained values for shikimic acid seem unrealistically low.

While the diffusion of the bulk molecules seems to play a major role in the uptake process according to the flux model fit to the flow tube data, the general trend in the dependence of uptake on humidity can be easily explained even if the bulk is well-mixed with respect to shikimic acid. An independent verification of the actual self-diffusion constant would therefore be of great use in determining the correct description of the uptake process. Diffusion constants can be calculated from viscosity via the Stokes-Einstein equation. There has been a recent, successful push to extend the range of viscosities which can be measured in small sample volumes (Hosny et al., 2013; Power et al., 2013). This is however only of limited use in answering questions regarding effects of transport limitation in the bulk, as viscosity and diffusion decouple at the low viscosities where transport limitation actually becomes relevant. A technique which could measure slow self-diffusion of molecules in the range of transport limitation would be of tremendous use in understanding the interplay of the different diffusion processes with reaction.

The discrepancy between model and experimental results could also point towards

fundamental problems with the model itself. One question here is whether the diffusion at the molecular level is treated correctly, another one whether the model might be too simple, i.e. relevant processes are not taken into account. One possible suggestion for such a process is a self reaction of O_3, as already suggested by Ammann and Pöschl (2007). Such a reaction would become more important relative to the bulk reaction with decreasing relative humidity. This in turn would lead to an overestimation of D_{b,O_3} at low RH if all of the uptake is attributed to the bulk reaction, as in our steady-state analysis of the data. Also in this case, investigation of the surface processes with a surface-sensitive technique could provide some idea regarding the likelihood of such a process. Other possible processes are e.g. changes of diffusivity or bulk to surface transport rate with time due to the changing composition of the film.
While there are still many uncertainties regarding the exact processes of the uptake, in particular at low humidity, we would like to point out that the kinetics can be adequately described by the resistor model down to about $\geq 50\,\%$ RH, where the solution is already significantly supersaturated.

One purpose of this study was the assessment of the likelihood of formation of chemical gradients due to transport limitation at low viscosity. As mentioned above, we did not see evidence for a chemical gradient in the microspectroscopy experiments. While the flux model results show development of gradients in shikimic acid for both optimized solutions at nearly all humidities, it should be noted that these gradients are generally very shallow and therefore smaller than can be resolved by our technique. Under closer examination, the same is true for the gradient shown in the supporting information of Shiraiwa et al. (2011). While larger gradients are in principle possible according to the flux model (see e.g Figure 4.10 for set B at 83 % RH and 92 % RH), it seems that a very specific combination of reaction constant, concentrations and diffusion coefficients of both reactants would need to be met to result in gradients observable with current instrumentation. While the KM-SUB model can be used to predict at which combination of reaction constants and diffusion coefficients such gradients appear, better measurements of these parameters would be needed for this, as it is currently not possible to predict those from fits with the model with the needed accuracy. It seems that in the majority of cases, the bulk is either completely well-mixed (at high humidity), or only a very short gradient is formed (at low humidity). Such gradients, often only nanometers wide, could be seen more as a surface crust instead of a wide reaching inhomogeneity. There are, however, some recent smog

chamber experiments on scooter exhaust which suggest formation of wider gradients (Figure 5.1, Coz et al., personal communications).

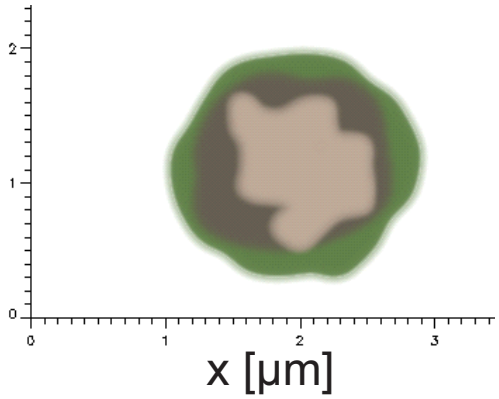

Figure 5.1: Chemical map of a particle collected from a smog chamber in which scooter exhaust was processed for 18 h under UV light (Coz et al.), measured with STXM/NEXAFS; Light brown indicates unsaturated carbon, dark brown carbon with ketone functionality, and green carboxyl-groups.

Changes in uptake of reactive gases due to moisture induced changes in diffusivity have now been shown for a variety of different gas-phase reactants and matrices, such as O_3 and shikimic acid (this study), O_3 and bovine serum albumin (Shiraiwa et al., 2011), O_3 and maleic acid (Gallimore et al., 2011), ammonia and α-pinene SOM (Kuwata and Martin, 2012), OH-radicals and levoglucosan (Slade and Knopf, 2014), H_2O_2 and sucrose (Lakey et al., personal communications) and N_2O_5 and citric acid (Grzinic et al., personal communications, see Figure 5.2).

While the overall relevance of the influence of changing diffusivity in the larger atmospheric context is still under debate, the results of this study as well as previous studies on this topic make clear that it can significantly affect the reaction of organic matter. Differences in relative humidity during uptake measurements and lacking equilibration of the sample are therefore a likely source of discrepancies between different measurements of the same reaction system. In Figure 5.3, we show that e.g O_3 uptake on tannic acid, which is frequently used as a proxy for humic substances, is also influenced by humidity. The need for proper humidity control and measurement should therefore be firmly kept in mind when designing experiments which measure uptake on material that can undergo moisture-induced changes in diffusivity.
The uptake of O_3 on shikimic acid is too low to significantly affect O_3 concentra-

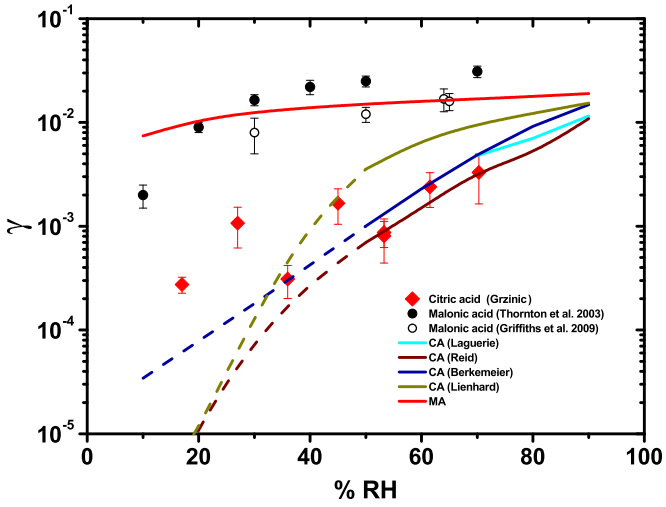

Figure 5.2: Comparison of the humidity dependent uptake of N_2O_5 on citric acid, measured by Grzinic et al., with data for malonic acid and parametrizations based on the resistor model formulation for reacto-diffusive uptake on particles. The different lines for citric acid denote different estimates of the N_2O_5 diffusion coefficient

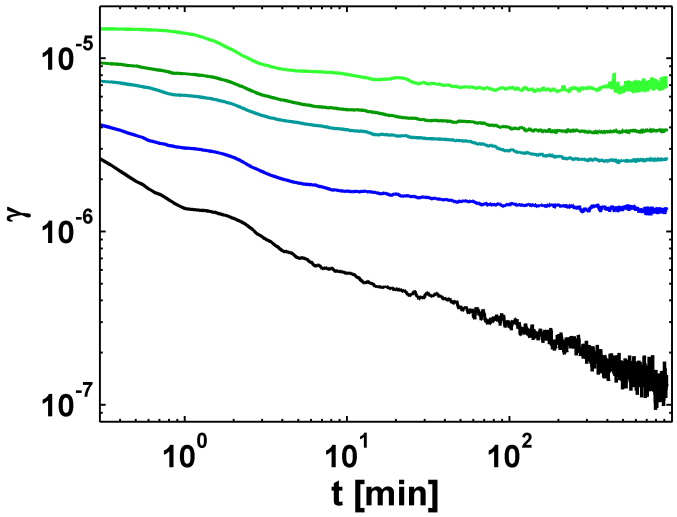

Figure 5.3: Ozone uptake on tannic acid at various humidities (95 % RH, light green line to 0 % RH, black line)

tion in the atmosphere at any of the measured humidities. Humidity does however significantly affect the chemical lifetime of shikimic acid itself in the atmosphere; it should increase from years at low humidity to only several days at high humidity (Chapter 3). Better knowledge of the composition of organic matter in atmospheric aerosol and the extent of the dependence of reactivity on diffusivity for the different compounds in mixture are needed to give a full assessment of the impact of glass formation on atmospheric chemistry.

Bibliography

Ammann, M. and Pöschl, U.: Kinetic model framework for aerosol and cloud surface chemistry and gas-particle interactions - Part 2: Exemplary practical applications and numerical simulations, *Atmos. Chem. Phys.*, **7**, 6025–6045, 2007.

Gallimore, P. J., Achakulwisut, P., Pope, F. D., Davies, J. F., Spring, D. R., and Kalberer, M.: Importance of relative humidity in the oxidative ageing of organic aerosols: case study of the ozonolysis of maleic acid aerosol, *Atmos. Chem. Phys.*, **11**, 12181–12195, 2011.

Hosny, N. A., Fitzgerald, C., Tong, C., Kalberer, M., Kuimova, M. K., and Pope, F. D.: Fluorescent lifetime imaging of atmospheric aerosols: a direct probe of aerosol viscosity, *Faraday Discuss.*, **165**, 343–356, 2013.

Kuwata, M. and Martin, S. T.: Phase of atmospheric secondary organic material affects its reactivity, *P. Natl. Acad. Sci. USA*, **109**, 17354–17359, 2012.

Power, R. M., Simpson, S. H., Reid, J. P., and Hudson, A. J.: The transition from liquid to solid-like behaviour in ultrahigh viscosity aerosol particles, *Chem. Sci.*, **4**, 2597–2604, 2013.

Shiraiwa, M., Ammann, M., Koop, T., and Pöschl, U.: Gas uptake and chemical aging of semisolid organic aerosol particles, *P. Natl. Acad. Sci. USA*, **108**, 11003–11008, 2011.

Slade, J. H., and Knopf, D. A.: Multiphase OH oxidation kinetics of organic aerosol: The role of particle phase state and relative humidity, *Geophys. Res. Lett.*, **41**, 5297–5306, 2014.

Acknowledgements

Many people have contributed to this work, either directly, through scientific input, or indirectly, by keeping me sane during those nearly four years. I would therefore like to thank:

- Tom Peter for taking me on as a PhD student and for the valuable input on this project...such as calling attention to how underdetermined a complex system might be!
- Markus Ammann, for supervising my work and being a great boss, for always being around for useful discussions about the experiments and data analysis as well as all things kinetics, for the valuable feedback on my manuscripts and for believing in my data even when I didn't. I am also very thankful for the many opportunities you gave me to present my work at different conferences and engage with the larger scientific community.
- Uli Krieger for his assistance with the EDB measurements, data analysis and manuscript, for sharing his vast knowledge about diffusion, for giving helpful advice on my other experiments, and for answering all my questions about physics.
- Daniel Knopf for agreeing to review this work
- Mario Birrer for fixing the things which (I) break and building cool new ones. This work would not have been possible without your amazing technical support.

- The various members of the IACETH who have contributed to this work with their scientific input, including Claudia Marcolli, Daniel Lienhard, Beiping Luo, and Andy Huisman.
- Thomas Berkemeier, for his work on modelling the flow tube data, his dedication to improve the KM-SUB code and answering my questions about the model.
- The beamline scientists at PolLux, Ben Watts & Jörg Raabe, for their support of our work at the beamline. In particular, I would like to thank Ben for not strangling me after any of my panicked "nothing is working" late-night phone calls.
- Manabu Shiraiwa, for providing the CKD and KM-SUB code
- All my former and current colleagues from the surface chemistry group. I would especially like to thank Markus Lampimäki, for teaching me how to use the STXM setup; Sepp Schreiber, for helping me over my initial Matlab-woes and cheering me up when things didn't work quite as expected; Thomas Ulrich, for keeping me company in the lab; and Thorsten Bartels-Rausch, for not only not kicking me out of the office despite the constant stream of questions, but even answering most of them.
- Angela Blattmann and Petra Forney for taking care of all things bureaucratic.
- All members of the Laboratory of Radiochemistry and Environmental Chemistry for the pleasant working atmosphere.
- My friends from Germany, especially Annika for listening to my multi-hour skype rants.
- My friends from Sweden, keep being awesome & tack så mycket!
- My friends from Zürich, especially Ting for organizing many cool trips through Switzerland; Elke, for the LaTeX support and being crazy in a good way; and the AVETH crowd, for providing ample distraction from work.
- Erik, for ALL the things

Thanks for the good times!